Forschungszentrum Karlsruhe
Technik und Umwelt

Wissenschaftliche Berichte
FZKA 6577

Experiments on the Axisymmetric Spreading of a Metallic Melt in Presence of Basal Solidification

F. Richter, P. Ehrhard
Institut für Kern- und Energietechnik

Juni 2001

Forschungszentrum Karlsruhe
Technik und Umwelt

Wissenschaftliche Berichte

FZKA 6577

Experiments on the axisymmetric spreading of a metallic melt in presence of basal solidification

F. Richter, P. Ehrhard

Institut für Kern- und Energietechnik

Forschungszentrum Karlsruhe GmbH, Karlsruhe
2001

Forschungszentrum Karlsruhe GmbH
Postfach 3640, 76021 Karlsruhe

Mitglied der Hermann von Helmholtz-Gemeinschaft
Deutscher Forschungszentren (HGF)

ISSN 0947-8620

Experiments on the axisymmetric spreading of a metallic melt in presence of basal solidification

When a jet of liquid metal impinges on a horizontal surface, we can observe a radial spreading of the melt. One can distinguish two separate regions of flow, firstly an area with supercritical flow and a thin fluid layer in the region around the point of impact, secondly an area with subcritical flow. The transition between these two types of flow is sudden, marked by a hydraulic jump. The position of the jump is dependent on time, it will decrease to zero during an experiment. The initial position is defined by the volumetric flow rate at the beginning of an experiment. This parameter is also responsible for the initial size of the jump radius and its behaviour (purely circular and undisturbed or irregular and unsteady). A further parameter of influence is the temperature of the base plate. The base plate temperature influences the jump in its position and its decreasing velocity. If this temperature is remarkably below the solidification temperature (non-isothermal case) the hydraulic jump radius is remarkably smaller in size and it moves faster inwards. The spreading itself also shows a strong dependence on these two parameters. In isothermal cases one can see a completely radial and axisymmetric spreading of the melt. If the plate temperature is below the solidification temperature, we have solidification during the spreading process. The consequence is the forming of a basal crust, which in the worst case, prevents the melt from flowing. There are fingers formed, which lead to a quite irregular shape of the melt, the axisymmetry, present in the case of isothermal spreading, is lost. The influence of the base plate temperature decreases with growing jet diameter. A remarkable effect is, that lower base plate temperatures lead to greater melt bodies in the case of the 10 mm aperture. The size of the spreading area in the case of the 5 mm aperture is independent of the base plate temperature as long as it is below solidification temperature. Experiments under non-isothermal conditions and with the 2 mm aperture have not been conducted because of the strong solidification. The size of the spreading area is in all cases proportional to a function of the type $A = c_1 Q^{c_2} t^{c_3}$, where A is the size of the spreading area, Q is the volumetric flow rate and t the time since first impact. For a detailed description of the dependencies and phenomenon, experimental data are required. In the following, a set of experiments with different outlet conditions is described. The varied parameters are the diameter of the outlet aperture (=diameter of the jet), the height of fall of the melt and the temperature of the base plate.

Experimente zur achsensymmetrischen Ausbreitung metallischer Schmelzen bei gleichzeitiger Erstarrung

Trifft ein Strahl metallischer Schmelze auf eine horizontale Oberfläche, so kann man eine radiale Ausbreitung der Schmelze beobachten. Es sind zwei Bereiche unterschiedlicher Strömungen zu beobachten, zum Einen ein Gebiet überkritischer Strömung und sehr dünner Schichtdicke rund um den Auftreffpunkt des Strahles, zum Anderen ein Gebiet unterkritischer Strömung mit großer Schichtdicke. Der Übergang zwischen beiden Gebieten ist abrupt, gekennzeichnet durch einen hydraulischen Sprung. Die Position dieses Sprunges ist zeitabhängig und seine Anfangsposition ist festgelegt durch den Volumenstrom zu Beginn des Experimentes. Dieser Parameter bestimmt auch das Verhalten des hydraulischen Sprunges (vollkommen kreisförmig und ungestört oder unregelmäßig und unruhig). Eine weitere Einflußgröße ist die Temperatur der Grundplatte. Liegt sie unterhalb der Erstarrungstemperatur (nicht-isothermer Fall), so ist der hydraulische Sprung merklich kleiner in seiner Ausdehnung (Radius), außerdem wandert er schneller nach innen. Die Ausbreitung selbst zeigt ebenfalls eine starke Abhängigkeit von diesen beiden Parametern. Im isothermen Fall kann man eine vollkommen radiale und achsensymmetrische Ausbreitung beobachten. Im nicht-isothermen Fall tritt während der Ausbreitung eine Erstarrung der Schmelze auf. Dadurch bildet sich eine Bodenkruste, die im Extremfall eine weitere Ausbreitung der Schmelze verhindert. Es bilden sich sodann zahlreiche Finger, die zu einer stark zerklüfteten Form der Schmelze führen. Die Achsensymmetrie wie im Falle der isothermen Ausbreitung geht gänzlich verloren. Der Einfluß der Temperatur der Grundplatte sinkt mit steigendem Strahldurchmesser. Auffallend ist, daß niedrige Grundplattentemperaturen zu größeren Schmelzekuchen führen, wenn der Strahldurchmesser 10 mm beträgt. Im Falle der 5 mm Strahlöffnung zeigt sich im nicht-isothermen Fall keine Abhängigkeit von der Grundplattentemperatur. Experimente mit der 2 mm Strahlöffnung und Grundplattentemperaturen unterhalb der Erstarrungstemperatur wurden wegen der erheblichen Krustenbildung nicht durchgeführt. In allen Fällen ist die Größe der Ausbreitungsfläche proportional zu einer Funktion des Typs $A = c_1 Q^{c_2} t^{c_3}$, wobei A die Größe der Ausbreitungsfläche, Q der Volumenstrom und t die Zeit seit dem ersten Auftreffen der Schmelze auf die Grundplatte bedeuten. Um die auftretenden Phänomene und Abhängigkeiten detailliert beschreiben zu können, sind experimentelle Daten notwendig. Im folgenden wird ein Satz Experimente beschrieben, bei denen die wesentlichen Einflußgrößen, wie die Größe der Austrittsöffnung (Strahldurchmesser), die Temperatur der Grundplatte und die Fallhöhe der Schmelze, variiert wurden.

Contents

The results of the experiments

Characteristic quantities of the flow

Appendix A: Description of the experiments

Index of Symbols

Solidification temperature:	T	$^\circ C$
Density:	ρ	kg/m^3
Specific heat:	c_p	J/kgK
Heat conductivity (liquid):	λ	W/mK
Dynamic viscosity:	η	Pas
Kinematic viscosity:	ν	m^2/s
Mass of melt:	m	kg
Gravity acceleration:	g	m/s^2
Time:	t	s
Volumetric flow rate:	$\dot{V}$	m^3/s
Jet velocity:	u_{jet}	m/s
Aperture diameter:	d	m
Spreading area:	A	m^2
Height of the melt:	h_{melt}	m
Height of fluid layer:	h	m
Height of the streaming flow:	h_{str}	mm
Height of the shooting flow:	h_{sh}	mm
Radius:	r	m
Prandtl number:	Pr	–
Reynolds number:	Re	–
Froude number:	Fr	–

Table 1: Index of symbols

Material properties of MCP58:

Solidification temperature:	T	58	$^\circ C$
Density:	ρ	9230	kg/m^3
Specific heat:	c_p	201	Ws/kgK
Heat conductivity (liquid):	λ	10	W/mK
Prandtl number:	Pr	0.85	
Reynolds number:	Re	$f(t,r)$	
Dynamic viscosity:	η	$f(T)$	
Kinematic viscosity:	ν	$f(T)$	

Table 2: Properties of MCP58.

T	58	60	62	64	66	68
η	0,0468	0,0446	0,0428	0,0414	0,0403	0,0393
ν	5,0754E-06	4,8348E-06	4,6417E-06	4,4867E-06	4,3624E-06	4,2626E-06

T	70	72	74	76	78	80
η	0,0386	0,0380	0,0375	0,0372	0,0368	0,0366
ν	4,1825E-06	4,1182E-06	4,0666E-06	4,0252E-06	3,9920E-06	3,9653E-06

Table 3: Dynamic and kinematic viscosity.

For the calculation of the kinematic viscosity, a constant melt density is assumed at temperatures in the range from 58 $^\circ C$ to 80 $^\circ C$. It is

$$\nu = \frac{\eta}{\rho} \quad .$$

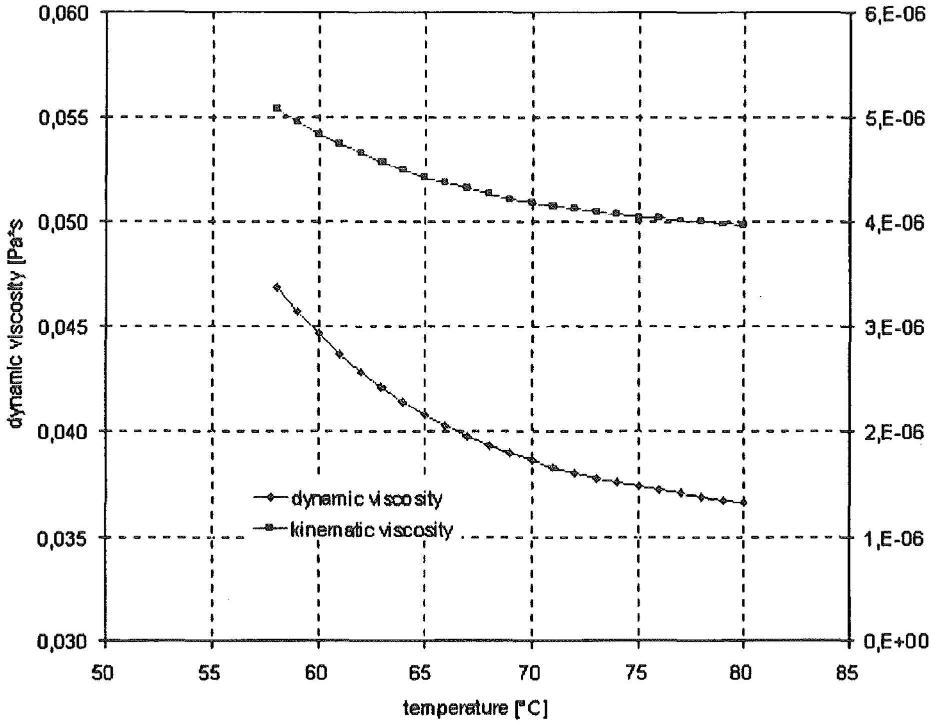

Figure 1: Dynamic and kinematic viscosity.

Reynolds number

The initial Reynolds number at the beginning of an experiment for the liquid jet is around $Re = 1500$ for the 5 mm aperture and $Re = 3300$ for the 10 mm aperture. These values refer to the outlet aperture (before the acceleration through gravity). They increase to $Re = 4000$ respectively $Re = 8000$ at the impact point (before redirection from vertical to horizontal flow). The Reynolds numbers on the base plate depends on volumetric flow rate and radius, for a detailed calculation see page 49.

The experimental rig

A schematic drawing of the experimental rig is shown in figure 2. The main parts of the experimental rig are:

- Melt container
- Base plate
- Image recording system and lighting
- Measuring device
- Heat- and cooling units

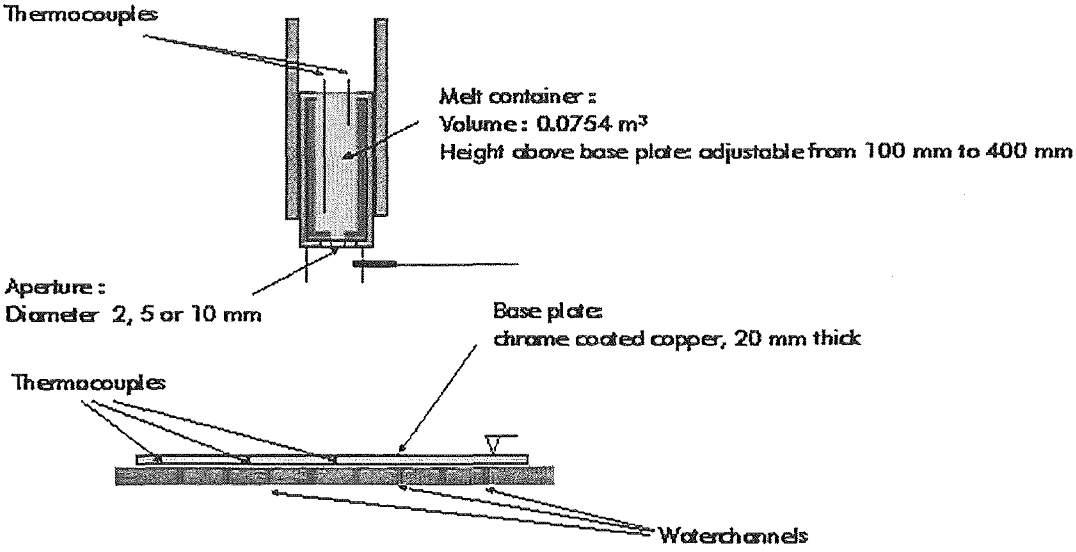

Figure 2: The experimental rig.

a) Melt container

The melt container is connected with a heater to hold the melt at a specific temperature, normally 5 degrees above the solidification temperature. At the bottom of the melt container, there is an aperture, which has a diameter of either 2, 5 or 10 mm. At the beginning of an experiment, the aperture is opened suddenly by a spring loaded piston. The flow signal of melt is detected from the signal of a light barrier. The melt temperature is measured at the bottom and at the top of the melt container. The volume of the melt container is 0.000754 m^3, this is equal to a maximum load of approximately 6,9 kg with MCP58.

b) Base plate

The base plate is a mirrorfinished chromecoated copperplate with a thickness of 20 mm and a diameter of 640 mm. The base plate can be kept at any temperature between 4 °C and 60 °C. Therefore, a system of water channels is integrated below the copper plate. The maximum temperature is limited by the used materials of the rack. Three themocouples are integrated into the base plate, one in the center (impact area of the liquid jet), one at half radius and one at the outside radius.

c) Image recording system and lighting

The image recording system consists of a CCD- camera, an appropriate computer system with an image processing software and an artificial lighting. The artificial lighting is neccessairy because the environmental light causes many reflections on the surface of the base plate.The position of the CCD - camera can be varied in all directions to obtain the best viewing angle (the best viewing angle changes with the height of the melt container). The focus of the camera is adjusted to the impact area.

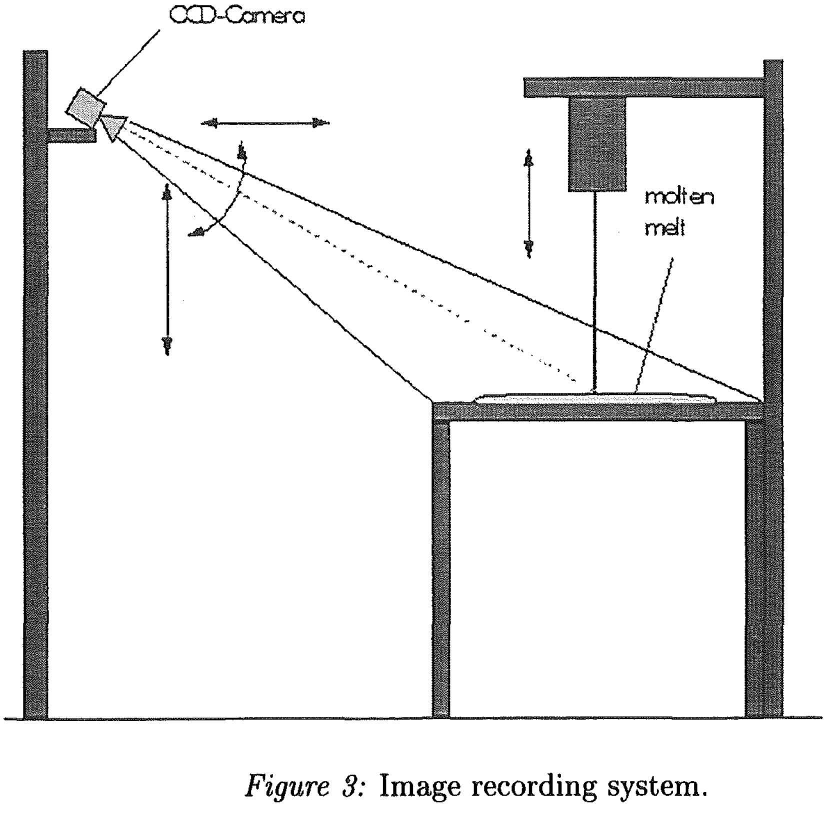

Figure 3: Image recording system.

d) Measuring device

All thermocouples are connected to thermocouples in a reference thermostat at $0°C$ to reach maximum accuracy of the measurements. The measured data are recorded with a data scanner combined with a computer data gathering system. Additionally some of the measuring channels are sent to a pen recorder. The data are stored on harddisk for further evaluation like the transformation into temperatures (during the experiments, only voltages are measured). All thermocouples are of type k (Ni-CrNi).

e) Heating and cooling units

Two heaters are used, one for the base plate and one for the melt container. The temperature of the melt container is hold constantly at $63°C$, the temperature of the base plate can be adjusted from $4°C$ to $60°C$.

Enhancements of the experimental rig

Before the experiments can begin some enhancements have to be applied. The first thing is the replacement of the base plate. The old one had a thickness of 5 mm and it was not strong enough to withstand the pressure caused by the circulating water, resultin in a non-planar surface. The new base plate is described in the passage before. The second enhancement concerns the lighting. After the installation of the new base plate a new problem appeared. Now it is difficult to distinguish between base plate and liquid melt, because they have the same reflection properties and color. Therefore, it is necessary to install some lights around the base plate to obtain reflections along the melt front line. The lighting consists of seven bar lights connected to a ring. A schematic drawing is shown in fig 4.

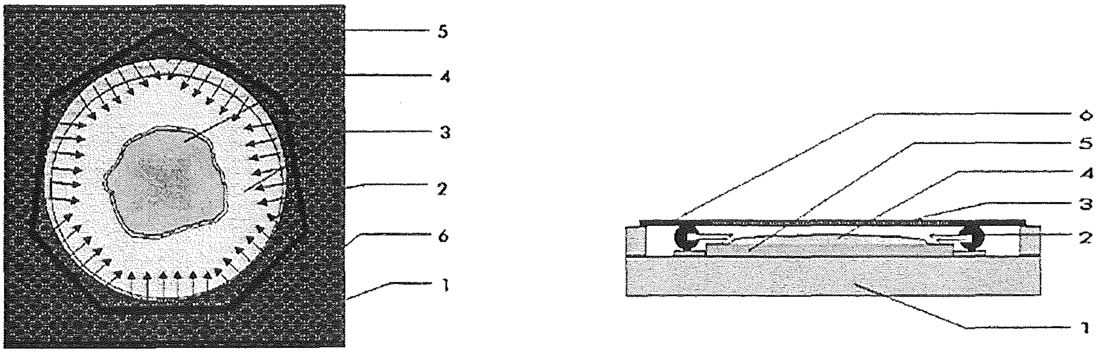

Figure 4: The installation of the lights in top view (left) and side view (right). 1=Experimental rack, 2=bar light, 3=visible area (light grey colored area),4=liquid melt, 5=base plate, 6= coverage as protection from glare.

The geometric distortion of the recorded images

The geometric distortion of the recorded images results from the inclined camera position. If we look at the video screen, distortions in all axis directions are to notice. What we have is a distortion with vanishing point, the effects are shown in the figure 5.

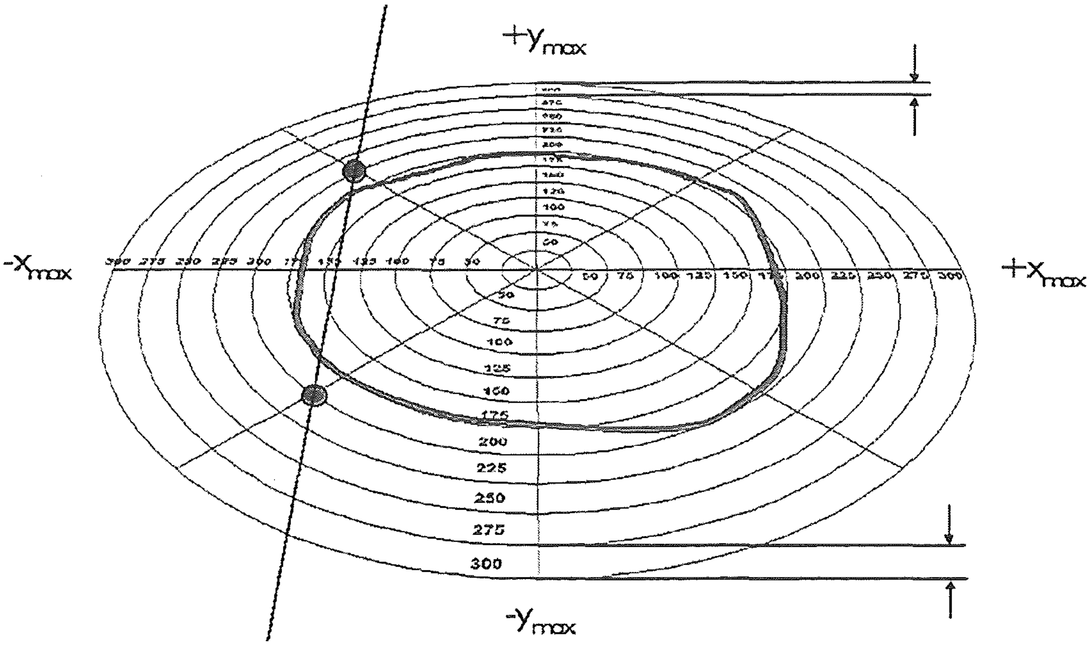

Figure 5: Illustration of the geometric distortions. The two marked points have the same distance from the center, the numbers represent the radius of the adjacent circles in *mm*. The origin of the coordinate system is in the intersection of the two axis.

Distortion in y-direction

The y-axis is jolted in the direction from the bottom to the top margin of the picture. The spaces between two neighbouring points decrease in size. The decrease is not linear, so a quadratic function in y is needed to correct this distortion.

Distortion in x-direction

The x-axis is jolted also, it becomes shorter from the bottom to the top of the image. The result is, that in truth lines parallel to the y-axis appear under an angle. This angle increases in direction from the selected origin of the coordinate system to the outer regions. In contrast to the y-axis, the x-axis is not jolted itself, that means the spaces between two neighbouring points remain constant at equal y-values.
For the evaluation of the recorded images, the distortion has to be corrected in such a way, that a pixel value received from the evaluation process can be transformed into

a metric value. This correction has to be included into the image processing software. The evaluation of area, circumference and radius requires additional programs.

Correction of the perspective distortion

The correction process is divided into several steps. These steps have to be executed before evaluating the images from the experiments. For the correction, a special calibration image is used. The single steps are:

1. Defining the origin of the coordinate system;
2. Scanning the points of intersection of the circles on the calibration sheet with the y- and x-axis. This step returns pixel values for x and y in the range of 0 to 511 in both directions;
3. Finding an approximative function for y-values;
4. Calculation of a general scaling factor for the x-axis (scaling factor for y-axis is included in the function mentioned above);
5. Transformation of the x-values with the scaling factor and the corrected y-values.

The correction has to be made in both directions, one time from pixel values to metric values and the other time from metric values to pixel values. The first correction is needed to evaluate the images, the second one serves as a mean to verify the quality and accuracy of the transformation. Therefore, circles are drawn on the video screen (depending on the actual cursor position) which are compared with the circles on the calibration sheet. If the circles coincide, the correction is good in quality and the evaluation result corresponds to real values.

The transformation functions and scaling factors

The general form of the function for correcting the y-values in case 1 is:

$$\begin{aligned} y_{metric} &= a_1(y_{pixel} - y_m)^2 + b_1(y_{pixel} - y_m) \quad &\text{for} \quad y_{pixel} > y_m \\ y_{metric} &= a_2(y_{pixel} - y_m)^2 + b_2(y_{pixel} - y_m) \quad &\text{for} \quad y_{pixel} < y_m \end{aligned}$$

In case 2, the argument is the calculated distance to the x-axis in y-direction of the circles to be drawn on the video screen. The factors a1, a2, b1 and b2 are different for case 1 and 2. There are 4 functions required for all corrections of the y-values.

Scaling factors

Two scaling factors are needed for the correction in the x-direction, a length-scaling factor and an angle-growth factor. The length scaling factor serves for the transformation of distance from the origin in pixel units to metric units. For $y = 0$, this factor is sufficient to correct the x-values. In cases $y \neq 0$, an additional step to correct the angular distortion is required. This problem is solved by the following function respectively equation:

$$\begin{array}{rcl} x_{pixel} = x_m + a_3(x - x_m) & + & \tan(c_1 a_3(x - x_m))(y_{corrected} - y_m) \\ x_{pixel} > x_m & , & x_m < x < x_{max} \\ x_{pixel} = x_m + a_3(x_m - x) & + & \tan(c_1 a_3(x_m - x))(y_{corrected} - y_m) \\ x_{pixel} < x_m & , & 0 < x < x_m \end{array}$$

The factor a_3 represents the length scaling factor, c_1 the angular growth factor. The x-values are corrected with the same function for both cases, however, in case one the equation has to be solved, in case two the x-value can be calculated directly. The figures 6 and 7 show the two correction processes. Process 1 is needed for evaluating the melt front line, process 2 is needed for evaluating the hydraulic jump radius and for a reliability test of the approximation.

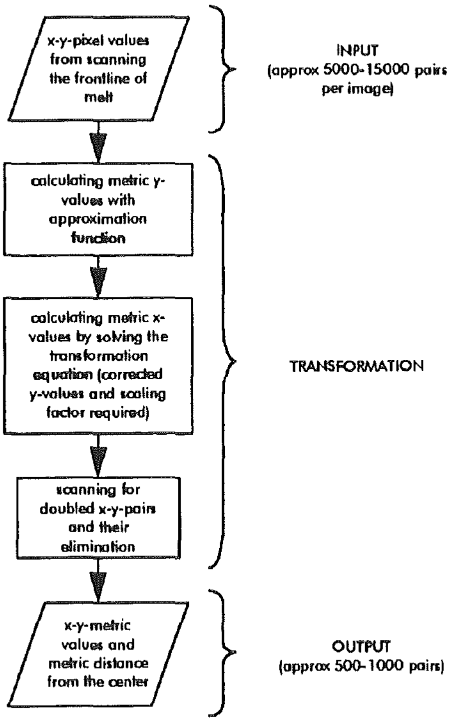

Figure 6: Correction process 1.

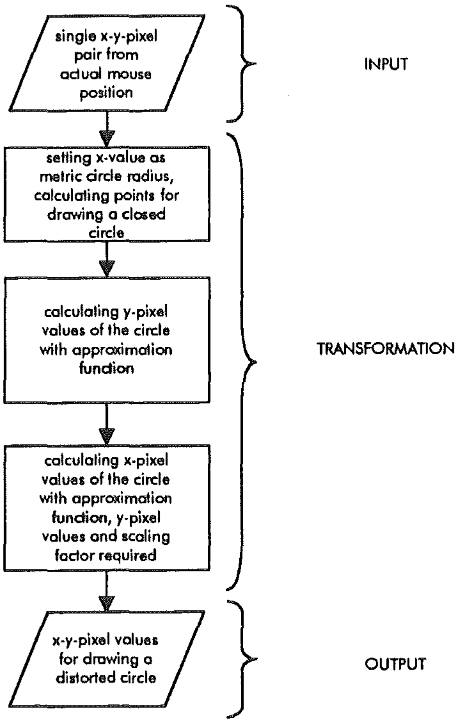

Figure 7: Correction process 2.

The evaluation of the experiments

The image evaluation process

For evaluating an experiment, several steps have to be executed and several programs are needed to extract the needed information and to display the results. The first part of the evaluation can be done with the interface program which also records the image series. The second part is done with the help of a spreadsheet program, which allows to apply several sorting and calculation processes to the data sets. At the beginning of an evaluation, the required steps for correcting the described distortions have to be executed. After that, the intrinsic evaluation process can start, it is divided into the following steps:

1. Defining the origin of the coordinate system (normally once for a whole image series, but also possible for each picture);
2. Scanning the melt front line by digitizing it with the cursor (approximated spline curve is added ´online´);
3. Scanning the hydraulic jump radius;
4. Transferring data sets to the spreadsheet program and extract the informations needed.

The structure of the progams and the required steps in the spreadsheet program are described in the following chapters.

The image processing and evaluation program

The image evaluation program is designed for an effective working and to get the needed experimental data. A block diagram of the program is shown in figure 12. Some features of the program are:

1. Ability to record image series with changing parameters (image size, time step between two recordings, number of images);
2. Show image series (all images of a serie in a row automatically or manually controlled picture by picture);
3. It includes modules for evaluating melt front line and hydraulic jump radius;
4. No console commands required, the whole evaluation process is executed on the video screen (not the normal computer monitor).

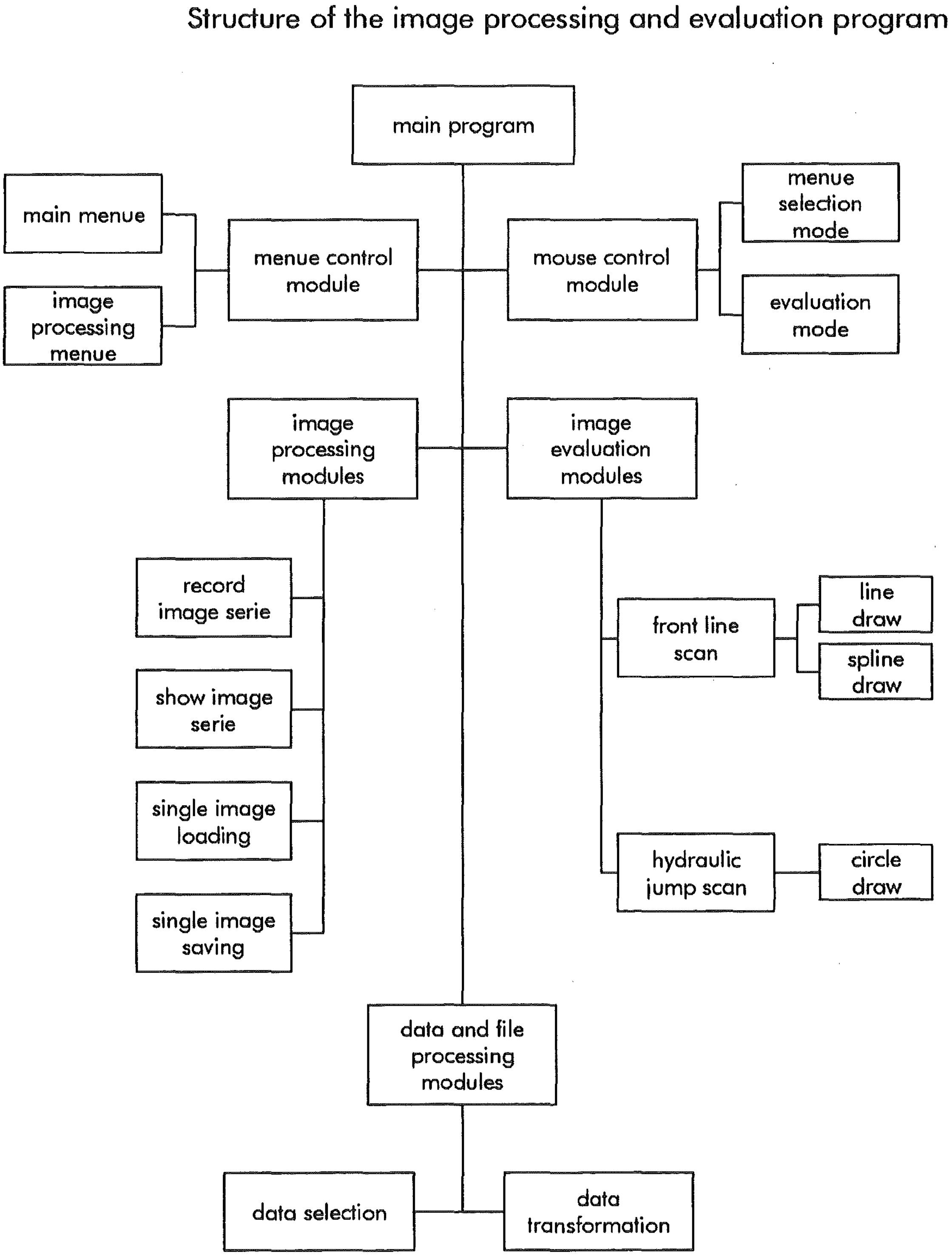

Figure 8: The components of the image processing and evaluation program.

Main program

The main program controls the file handling during the image evaluation or the recording / play process and calls the subroutines depending on the menue button selection. It also includes a part of the module for scanning the melt front and all commands for the post evaluation processes (mainly the creation of the output files).

Menue creating module

This part creates the graphic user interface, consisting of two menubars, one for the evaluation process and one for the image processing process. On the two pictures of figure 13, one can see screenshots from the video monitor which show the two menues during a typical image evaluation.

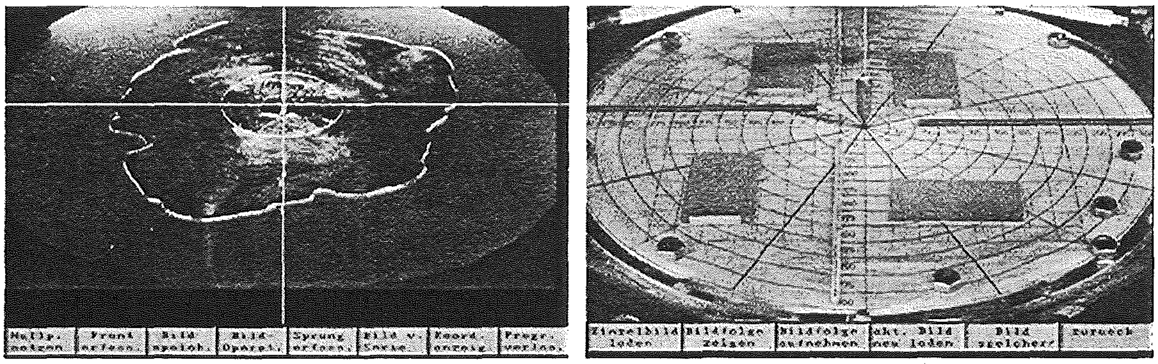

Figure 9: The graphic user interface of the evaluation program, left the evaluation menue while scanning a hydraulic jump radius (white distorted circle), right the image processing menue with the calibration image loaded.

Mouse control module

The mouse control module creates a mouse-cross or a mouse arrow, depending on the actual mouse position. There are two different modes, a menue selection mode and an evaluation mode. In evaluation mode, the mouse-cross can be replaced by an distorted circle (for scanning the hydraulic jump radius), two crossed lines (for defining the origin of the coordinate system) or by the actual end of the spline curve (spline curve is redrawn after each mouse movement).

Image processing modules

These parts are the interface programs for the CCD-camera. The recording module needs as input parameters the image size, the number of images and the time step between two pictures. The module for showing an image serie uses the same algorithms as the recording module. In both cases, the time is inferred from the internal computer clock.

Image evaluation modules

There are three modules required to evaluate an experiment. Two of these modules are integrated in the mouse module, the subroutines for The third module serves

- defining the origin of the coordinate system;
- scanning the radius of the hydraulic jump.

for evaluating the melt front postion. The melt front is approximated by modified interpolated cubic Bèzier-Splines. The theory of these special spline type is described separately.

The post evaluation process module

These modules perform all steps to reduce the amount of data to a minimum. After scanning a melt front, the first data file contains between 9000 an 15000 coordinate pairs. The final data file contains usually not more than 1000 pairs (depending on the melt front size). After this selection process, the data are transformed to metric coordinate pairs. Simultaneously, the distance to the origin is calculated.

The approximation of the melt front

The melt front is approximated by a piecewise composed spline curve. The spline type is a modified version of cubic Bèzier-Splines. The Bèzier-Splines have several advantages, which support the scanning and the approximation of a melt front line:

- The interpolation points can be used directly in this modified form of Bèzier-Splines (normally, one has to select so- called weighting points, which are not part of the spline curve);
- The interpolation points do not need to be equidistant;
- The interpolation points do not have to decrease or to increase monotonously;
- Closed curves can be approximated;
- The trend of the spline curve is identical with the trend of the melt front line.

The common form of a Bèzier-Spline is as follows [1]:

$$\begin{aligned} P(v) &= (1-v)^3 b_k + 3(1-v)^2 v k_{k+1} + 3(1-v)v^2 b_{k+2} + v^3 b_{k+3} \quad , \\ k &\in [0,1,2...m-1] \quad , \quad m \geq 2 \quad , \quad v \in [0,1] \end{aligned}$$

$P(0)$ is the starting point and $P(1)$ is the end point of the spline curve or the Bèzier segment. The Bèzier points b_1, b_2, $\cdots$, b_{3m-2}, b_{3m-1} are calculated with help of the weighting points $d_0,\cdots,d_m$ according to the following scheme:

$$\begin{aligned} b_{3k-2} &= \frac{1}{3}(2d_{k-1} + d_k) & ,k = 1(1)m \quad , \\ b_{3k-1} &= \frac{1}{3}(d_{k-1} + 2d_k) & ,k = 1(1)m \quad , \\ b_{3k} &= \frac{1}{6}(d_{k-1} + 4d_k + d_{k+1}) & ,k = 1(1)m-1 \quad . \end{aligned}$$

The Bèzier points for calculating the x-and y-values are different, in fact, two functions are required. In this special case, the Bèzier points are first set equal to the interpolation points. Then there are some additional (virtual) points calculated (by taking the mean of two consecutive points). These virtual points are used as weighting points. In an iteration process they are changed until they are close to the interpolation points. The two figures on the following page explain this method. For the numerical calculation of the Bèzier-curves, a Fortran subroutine from [1] is used. To reduce the amount of data, it is neccesairy to split the melt front line into several packages, each one is limited to a maximum of eight single segments. This principle is also clarified in the figure 11 on the next page.

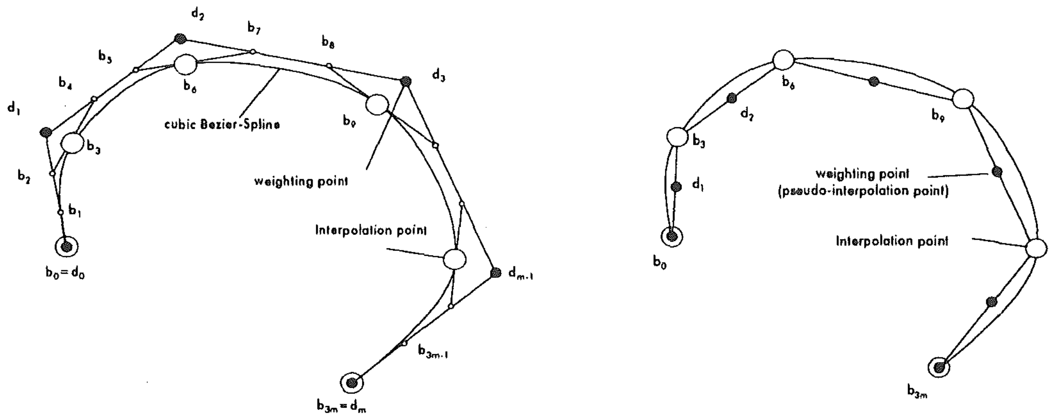

Figure 10: Schematic drawing of the Bèzier-Spline approximation, left the normal method, right the modified (interpolating) method.

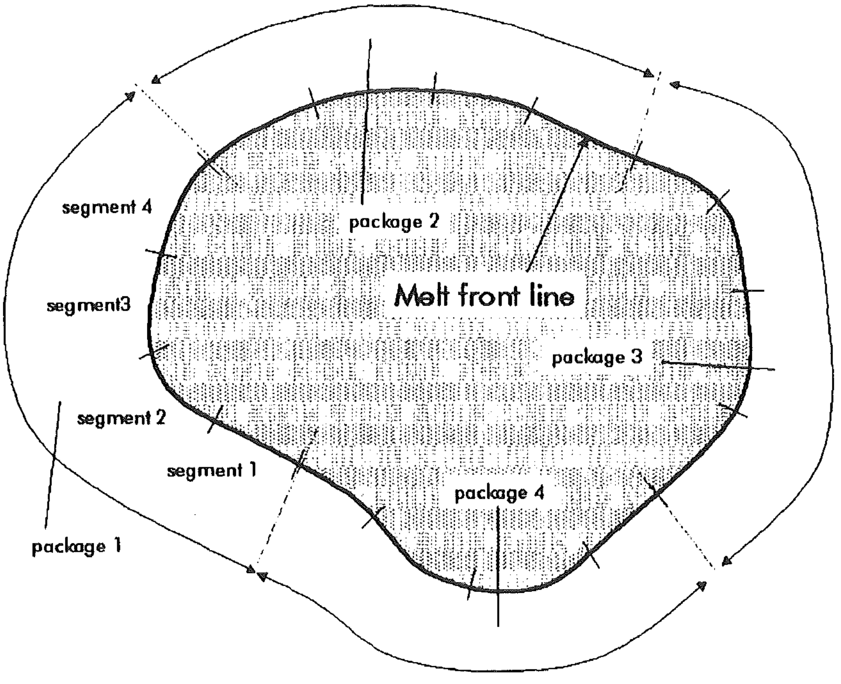

Figure 11: The splitted melt front.

Each segment of the curve is represented by 201 data points. Because of the limited computer memory, only 8 segments can be calculated at the same time. After reaching a number of 8 segments, the first four segments of this package are stored in the data file (one should remark that these curve segments don't change much when moving the end point of the eighth segment). The rest of the segments are renumbered starting with one within the segments.

Determination of area and circumference

The final step of the evaluation is the determination of the area and the circumference from the scanned melt front. For this, each scanned melt front line is divided into horizontal lines, like shown in figure 12. A specific width can be assigned to each line, it results from the distance to the neigbouring line. Normally, this width is about one milimeter. The partial area that each line results from the length of the line (= value of the x-coordinate) and its width. All partial areas together give the area enclosed by the melt front line. At first, the data have to be sorted by the y-coordinates. This is strongly required, because double lines have to be removed (set to zero) and missing lines (=missing y-values) have to be filled by counting the neighbouring line twice. The sorting allows also to include the fingers in the calculation. Normally, each y-value appears twice - the length of each line is counted from the y-axis. The extract of an evaluation sheet (table 4) explain the procedure.

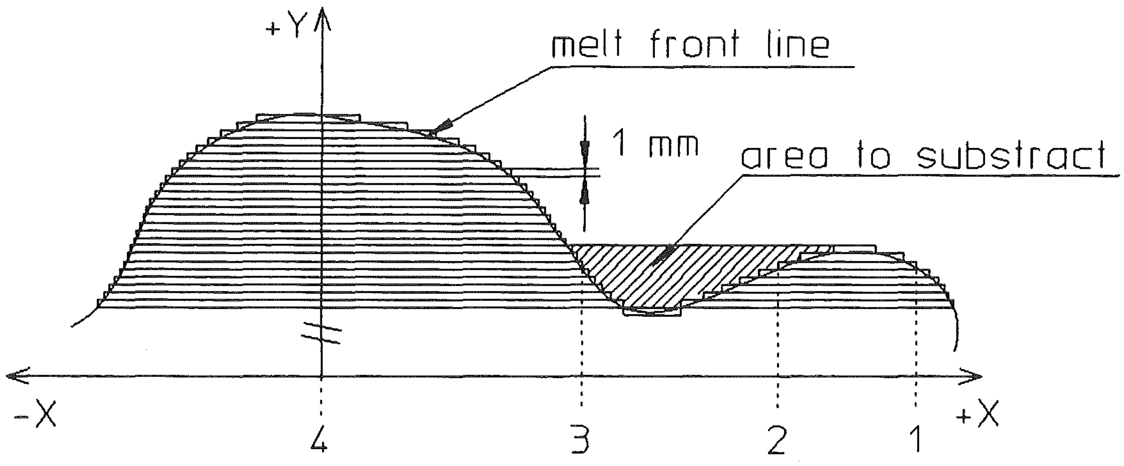

Figure 12: The principle of the evaluation of the spreading area.

At $y = -152$ or $y = -153$ we have normal conditions, one line in each direction (+ and - x-direction). Both values are counted positive for the area sum. At $y = -156$, we have several lines in the -y-direction. Such a case is shown in the figure 12, marked by the vertical dashed lines (points 1 to 4). The data sets are sorted twice, first by increasing y-values and secondly by increasing x-values, so the outside border is counted positive (length between point 4 and 1) and the inside border is counted negative (length between point 4 and 2). The length between point 4 and 3 is counted positive again (see the most right column in the table). The sum of this column is the size of the area. All values in the table have $[mm]$ as unit.

X-coord.	Y-coord.	Radius	circumference-portion X	circumference-portion Y	Height Y	circumference-portion	area portion +X	area portion -X	area portion total
49	-156	163,51	1	1	1	1,41421	49	0	49
-22	-156	157,54	6	1	1	6,08276	0	22	22
-34	-156	159,66	2	1	1	2,23607	0	-34	-34
-89	-156	179,60	0	1	1	1,00000	0	89	89
48	-155	162,26	1	1	1	1,41421	48	0	48
-28	-155	157,51	6	1	1	6,08276	0	-28	-28
-89	-155	178,73	0	1	1	1,00000	0	89	89
47	-154	161,01	1	1	1	1,41421	47	0	47
-89	-154	177,87	1	1	1	1,41421	0	89	89
47	-153	160,06	0	1	1	1,00000	47	0	47
-88	-153	176,50	1	1	1	1,41421	0	88	88
46	-152	158,81	1	1	1	1,41421	46	0	46
-89	-152	176,14	1	1	1	1,41421	0	89	89

Table 4: Extract of an evaluation sheet.

The circumference is the sum of the column "circumference portion", while each portion is calculated geometrically as follows:

$$circumference\_portion = \sqrt{\Delta x^2 + \Delta y^2} \quad .$$

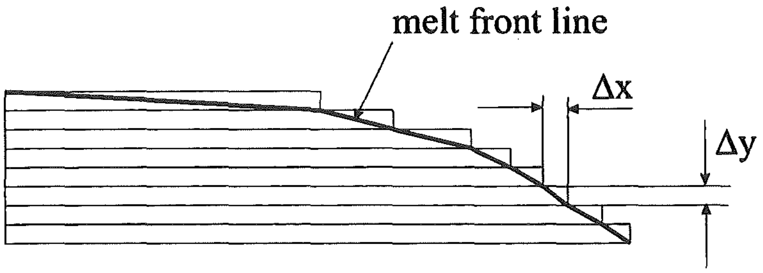

Figure 13: Determination of the circumference of the melt front line.

Error estimation of the evaluation process

The selected way of evaluating the images from the experiments is not error free. The reason is the angle of image recording, it does not capture areas in the rear of the base plate. The source of error is, that the melt front line (= contact line of melt with base plate) is determined from the visible borderline on the images. This effect is shown in figure 14. This is, of course, not completely accurate as demonstrated in the figure 14. One can see that the virtual contact line of melt (3) is ahead the real contact line (2) with the base plate (1). This problem appears only in areas opposite to the camera. The magnitude of the error depends on thickness and inclination of the boundary of liquid melt (4). Another factor of influence is the angle between camera and liquid melt. The error growth with the angle between camera and the vertical. The error of the evaluation is estimated experimentally. The idea is to evaluate circles with a defined size and to compare the results with the real values for each circle with regard to area, circumference and average radius. The circles are taken from the calibration image, which has circles with diameters from 50 *mm* to 550 *mm* in steps of 50 *mm*. The circles represent melt front lines, they are scanned and evaluatet in the same way as in a normal experiment. The results are shown in figure 15, the relative error of

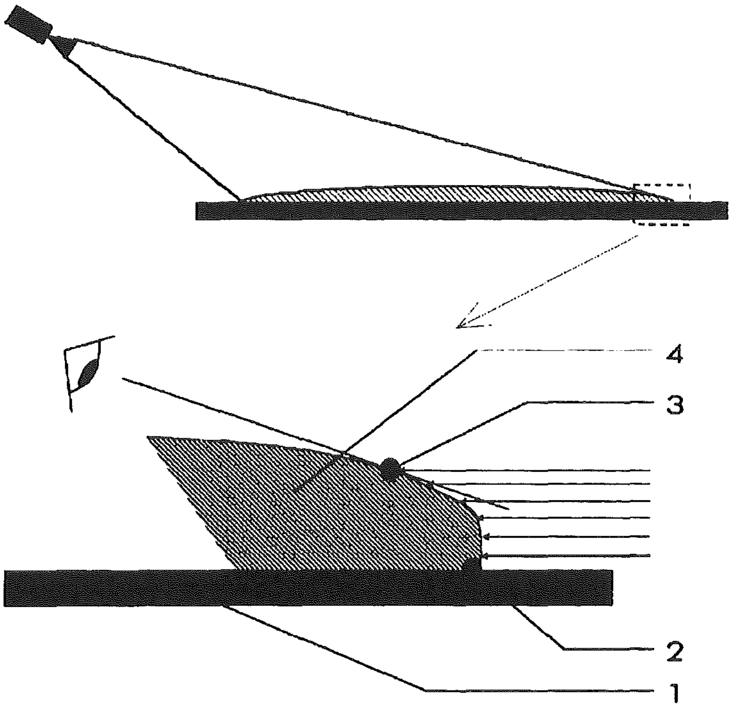

Figure 14: Virtual and real contact line.

the experimental values with regard to the real values are calculated as follows:

$$percentage\ error = \frac{|calculated\ value| - |real\,value|}{|real\,value|}\,100\%.$$

Diameter	Area $[mm^2]$		Circumference $[mm]$		Average radius $[mm]$	
	experiment	real	experiment	real	experiment	real
50	1958	1963	159,79	157,08	24,92	25,00
100	7894	7854	321,25	314,16	50,24	50,00
150	17745	17671	479,78	471,23	75,45	75,00
200	31627	31416	640,99	628,31	100,52	100,00
250	49311	49087	808,21	785,39	125,49	125,00
300	70839	70685	989,54	942,47	150,49	150,00
350	96273	96211	1143,73	1099,55	175,53	175,00
400	124727	125664	1319,54	1256,63	200,15	200,00
500	195458	196350	1605,34	1570,80	249,96	250,00

Table 5: Comparison between experimental and real values.

One can see that area and average radius correspond well with the real values. Only circumferences show larger differencies. The reason for that lies in the way the contour is scanned. The accuracy depends not conclusively on the human factor. The more exact the cursor is directed over the screen during scanning, the more exact is the result. Especially on strongly fingered contours, this premise cannot be kept always. Further, while calculating with gathered data, several transformations from float to integer variables are executed. This cannot be prevented without loosing information needed for the determination of area, circumference and average radius.

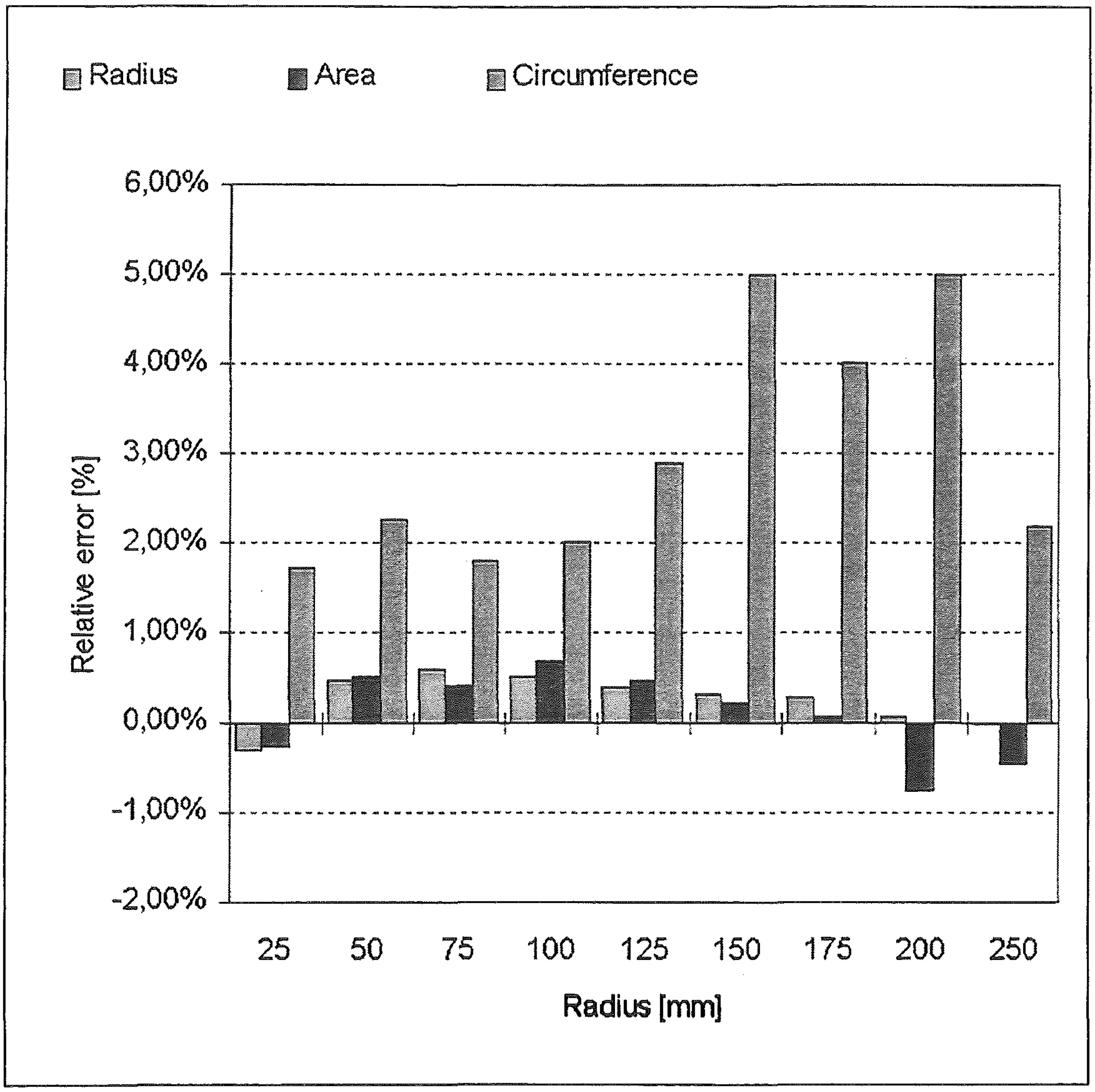

Figure 15: Relative error between experimental and real values.

The volumetric flow rate

The volumetric flow rate is determined experimentally. The experimental setup is similar to the setup in of the spreading experiments. A schematic drawing of the experimental setup is shown in figure 16. An electronic scale is positioned below the melt container. A basin catches the melt and is weighted simultaneously. In defined time steps, an image of both, the display of the scale and the display of the electronic clock is taken. The time stepping for the images is controlled by the host computer of the camera. With these two informations, time and actual weight, functions can be found which describe the mass of melt $m(t)$ and the volume of melt $V(t)$ in time t. To obtain the volumetric flow rate in time, the function $m(t)$ has to be differentated with respect to time. The equation is:

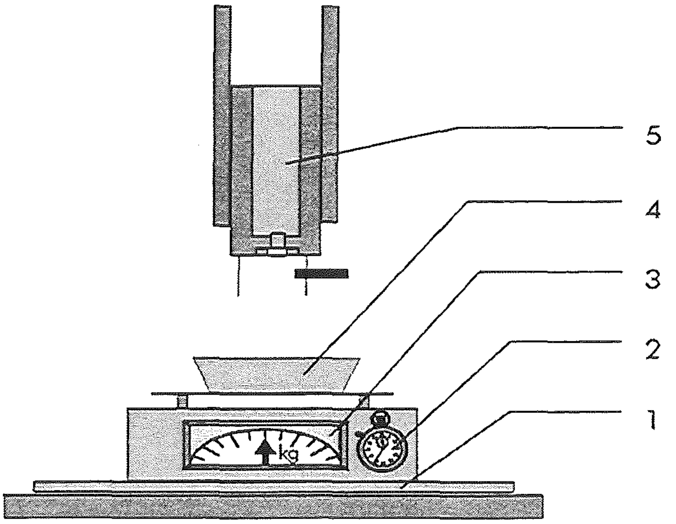

1 = Base plate
2 = Electronic time clock
3 = Electronic scale
4 = Basin
5 = Melt container

Figure 16: Experimental setup for the determination of the volumetric flow rate.

$$\dot{V}(t) = \frac{\dot{m}(t)}{\rho}$$

Two series of experiments are conducted to verify the influence of the amount of melt in the melt container. The first experiments are done with an average mass of 4.8 to 5 kg, the second set of experiments is done with a mass of approximately 6.3 to 6.5 kg. The results for the 5 mm and 10 mm aperture are shown in figures 17-19. Variations of the height of melt over the basin are not done because this parameter does not influent the volumetric flow rate. The height over the basin is approximately 150 mm. It is kept identical for all experiments.

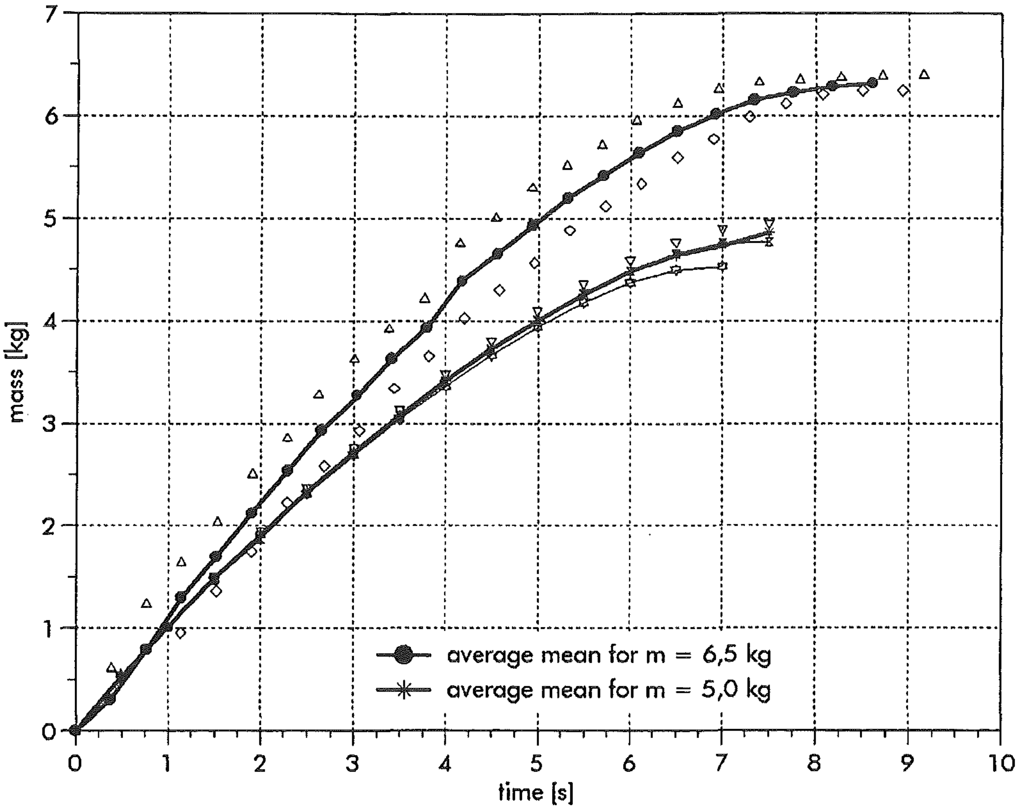

Figure 17: Results for the 10 *mm* aperture.

The least square fits for the 10 mm aperture are:

$$m_0 = 6.5 kg:$$

$$m = 2.073420 \cdot 10^{-5} t^4 - 5.420434 \cdot 10^{-3} t^3 - 4.03057 \cdot 10^{-3} t^2 + 1.149328 t$$

$$\dot{V} = \frac{1}{\rho}(8.29368 \cdot 10^{-5} t^3 - 1.626130 \cdot 10^{-2} t^2 - 8.06114 \cdot 10^{-2} t + 1.149328)$$

$$m_0 = 5.0 kg:$$

$$m = -4.908039 \cdot 10^{-4} t^4 + 5.314962 \cdot 10^{-3} t^3 - 7.076567 \cdot 10^{-2} t^2 + 1.083815 t$$

$$\dot{V} = \frac{1}{\rho}(-1.9632156 \cdot 10^{-3} t^3 + 1.5944886 \cdot 10^{-2} t^2 - 0.14153134 t + 1.083815)$$

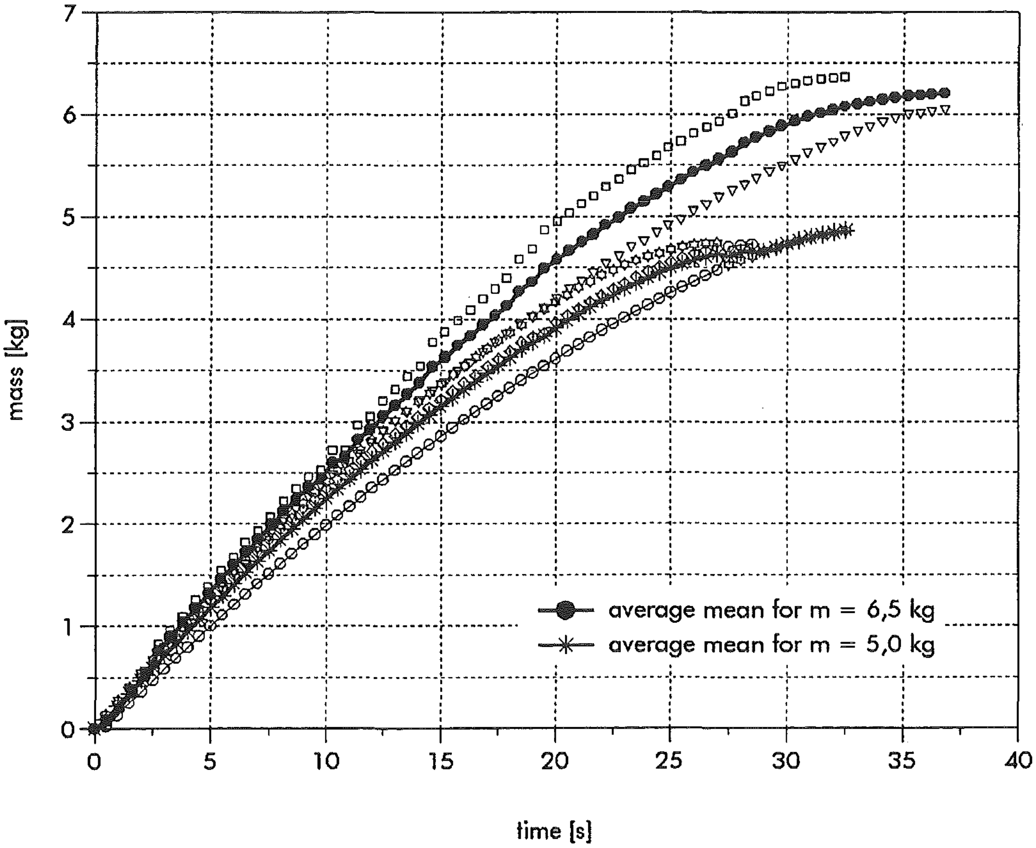

Figure 18: Results for the 5 *mm* aperture.

The least square fits for the 5 *mm* aperture are:

$$
\begin{aligned}
m_0 &= 6.5kg: \\
m &= -1.483083 \cdot 10^{-6} t^4 + 6.437110 \cdot 10^{-5} t^3 - 3.450752 \cdot 10^{-3} t^2 + 0.282045 t \\
\dot{V} &= \frac{1}{\rho}(-5.932233 \cdot 10^{-6} t^3 + 1.931133 \cdot 10^{-4} t^2 - 6.901504 \cdot 10^{-3} t + 0.282045)
\end{aligned}
$$

$$
\begin{aligned}
m_0 &= 5.0kg: \\
m &= -3.807564 \cdot 10^{-7} t^4 + 1.975041 \cdot 10^{-5} t^3 - 1.978483 \cdot 10^{-3} t^2 + 0.2462892 t \\
\dot{V} &= \frac{1}{\rho}(-1.523025 \cdot 10^{-6} t^3 - 5.925123 \cdot 10^{-5} t^2 - 3.956966 \cdot 10^{-3} t + 0.2462892)
\end{aligned}
$$

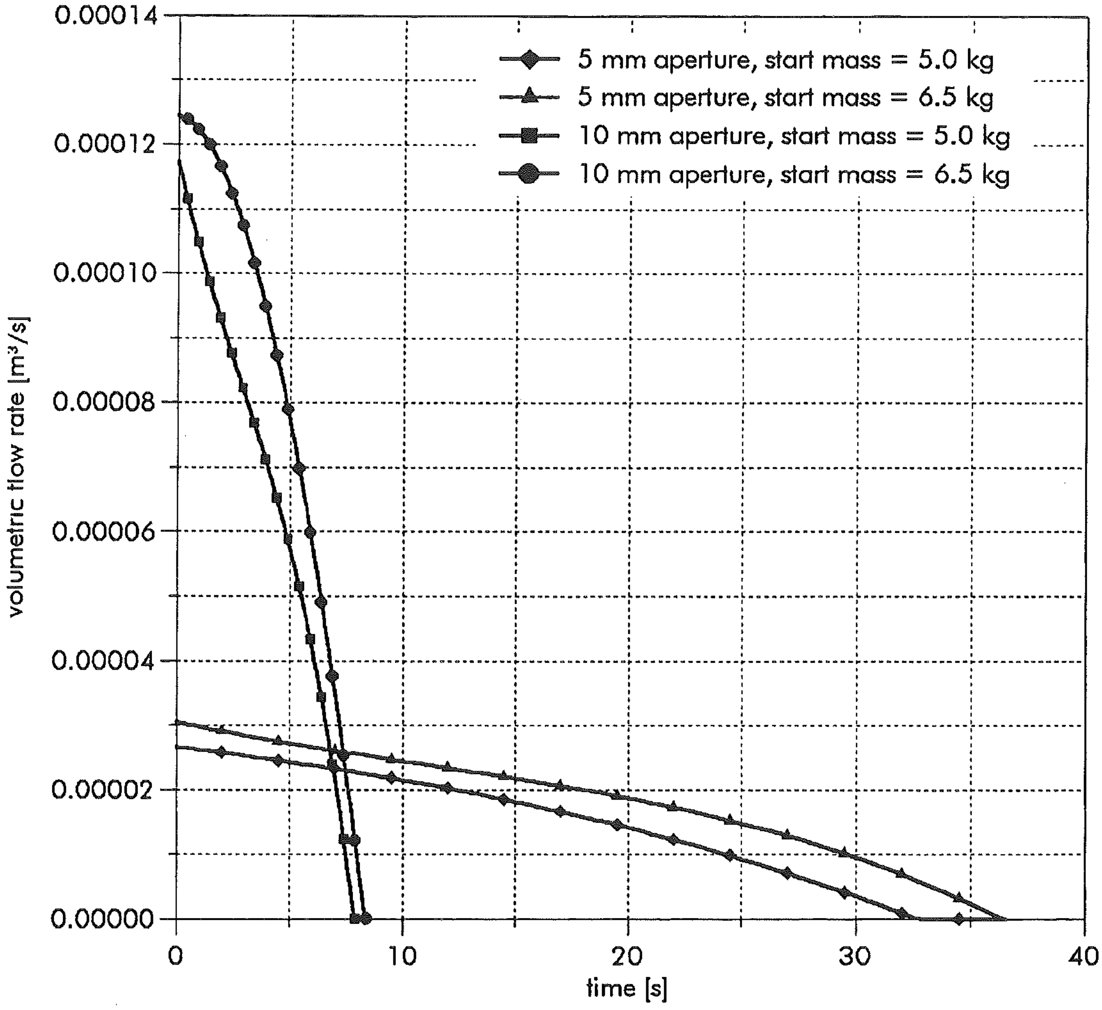

Figure 19: Volumetric flow rate for the 5 mm and the 10 mm aperture in time.

The results for the volumetric flow rate shows that the amount of melt has a remarkable influence only in case of the 10 *mm* aperture. The volumetric flow rate decreases rapidly in the first seconds in case of a starting mass of $m_0 = 5kg$. This circumstance leads to a difference around 20 to 40 % in a direct comparison at the same times. In case of the 5 *mm* aperture, the difference occurs numerically seen quite low, but it ranges around 10 and 20 percent, too. For the 2 *mm* aperture, no experiments are done. A direct calculation of the volumetric flow rate with the equations for the outflow from an open container with a non-constant liquid height gives poor results because the friction cannot be neglected in our case. The derivations with respect to our measurements are around 30 %.

The experimental program

The experimental program includes most of the possible parameter combinations. The varied parameters are the height of melt, the base plate temperature and the aperture diameter. The values for the aperture diameter are either 2 *mm*, 5 *mm* or 10 *mm*. The height of the melt outlet can be adjusted from 100 *mm* to 400 *mm* ahead the base plate . The base plate temperature can be varied from 4°C to 60°C (limited by the rack material). The different combinations of paremeters are listed in the three tables below.

Height of the melt	Base plate temperature			
	4°C	20°C	40°C	60°C
200 *mm*				
300 *mm*				mcp02
400 *mm*		mcp09		mcp05

Table 6: Experiments with the 2 mm aperture.

Height of the melt	Base plate temperature			
	4°C	20°C	40°C	60°C
200 *mm*			mcp19/20*	
300 *mm*	mcp10/17*		mcp01/18*	
400 *mm*		mcp08		mcp04

Table 7: Experiments with the 5 mm aperture.

Height of the melt	Base plate temperature			
	4°C	20°C	40°C	60°C
200 *mm*			mcp19/20*	
300 *mm*	mcp10/17*		mcp01/18*	
400 *mm*		mcp08		mcp04

Table 8: Experiments with the 10 mm aperture.

The expressions in the fields of the tables are the labels of the experiments. Details for each experiment can be found in appendix A. As one can see, experiments with an aperture diameter of 10 *mm* combined with a height of the melt of 400 *mm* are not performed. The reason for that is the high impact energy of the melt, which leads to spreading areas greater than the base plate. Furthermore, experiments with a height of the melt of 100 *mm* can also not be performed because in this case the only suitable camera position leads to a rather great evaluation error. The results of the experiments are discussed on the following pages. A detailed description of each experiment can be found on appendix A.

The experiments

When the spring loaded piston is released, the melt flows out of the melt container and impinges onto the base plate. Around the point of impingment, an area of shooting flow with high flow velocities is formed. The shooting flow is characterized by a thin fluid layer as we can see in figure 20. At a specific radius, the thin layer of shooting flow transits into a subcritical flow. The transition is sudden and the point of the transition (=position of the hydraulic jump) is time dependent. Outside the hydraulic jump, we have low flow velocities and a thick fluid layer. The melt outside the hydraulic jump is bounded by a contact line which moves outward in time.

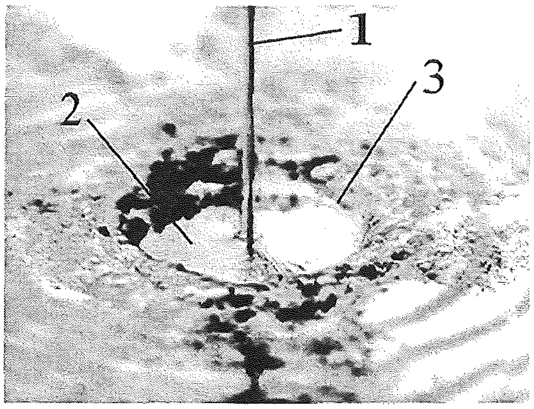

Figure 20: The flow around the point of impingement. One can see the jet of liquid melt (1), the area of the shooting flow (2) and the sudden transition from shooting (supercritical) to streaming (subcritical) flow (3).

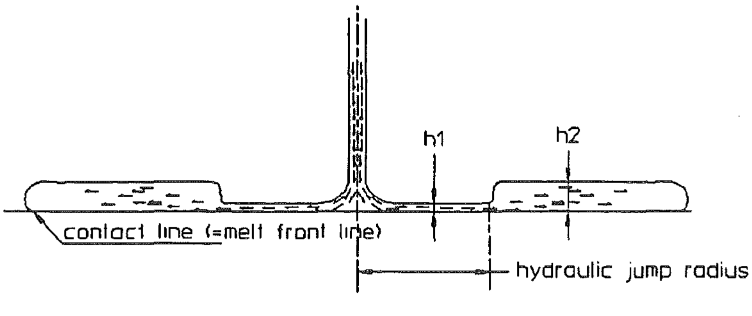

Figure 21: Profile of the flow

A profile of the flow is shown in figure 21. The thicknesses h1 and h2 give the height of the fluid layers before and after the hydraulic jump. The diameter of the liquid jet is slightly smaller than the aperture diameter. The spreading of the melt is approximately axisymmetric in case of isothermal spreading. The thickness of the fluid layer is almost constant both inside and outside the hydraulic jump. If the conditions are non-isothermal (cooled base plate), a basal crust is formed and the spreading becomes non-axisymmetric. A strong fingering is present for such conditions. This effect is best seen from a sequence which shows the spreading (figures 22-25).

Comparison isothermal non-isothermal spreading

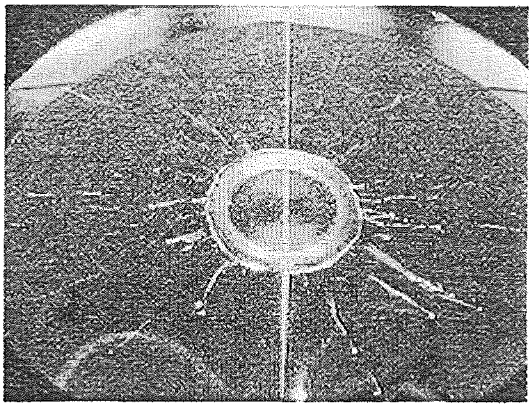

Figure 22: Isothermal spreading

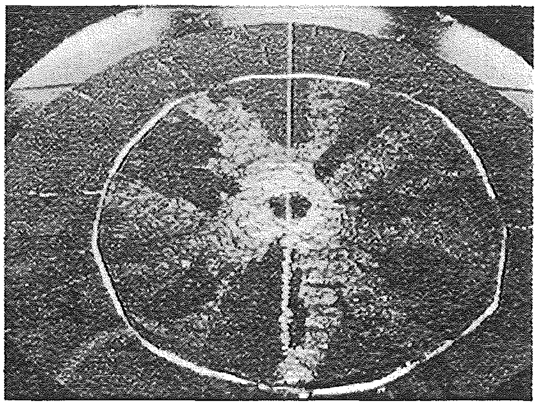

Figure 23: Isothermal spreading

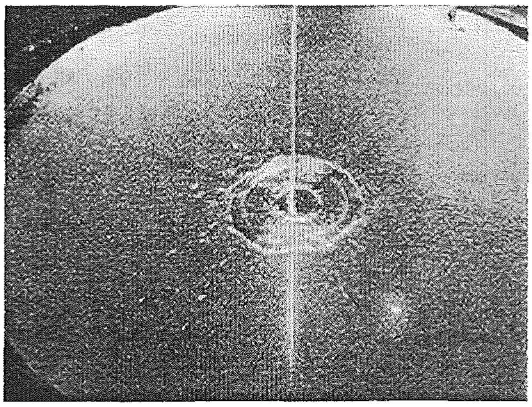

Figure 24: Non-isothermal spreading

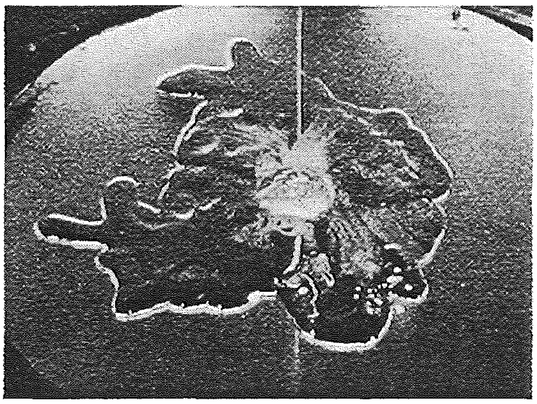

Figure 25: Non-isothermal spreading

In figure 22-25 we can see pictures taken from the experiments. figure 22 and figure 23 show the isothermal case, figure 24 and figure 25 show the non-isothermal case. figure 22 and figure 24 are taken approximately 1.5 seconds after the jet has impinged on the base plate, figure 23 and figure 25 show the situiation after another 22.5 s. In the isothermal case, we can see the circular contact line (cf. figure 23). For the non-isothermal case (cf. figure 25) we can see a lot of fingers along the contact line. Some of these fingers are closed by following flow of melt, others survive until the complete solidification of the melt.

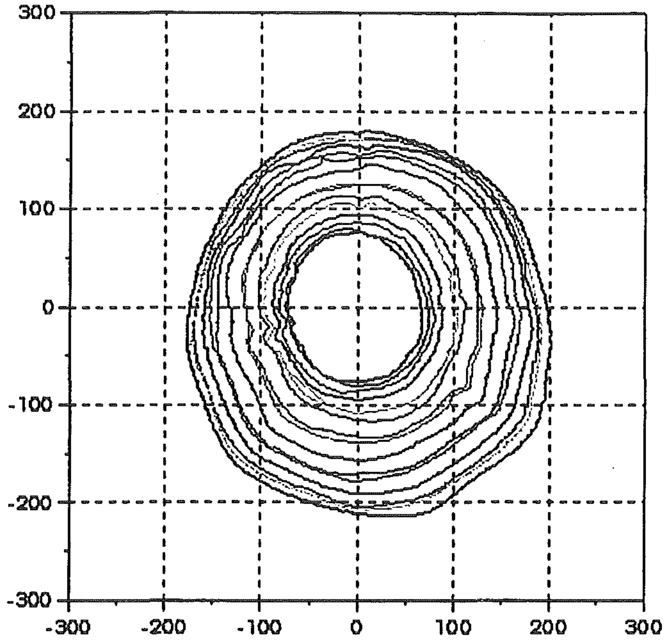

Figure 26: Sequence of the melt fronts for isothermal conditions (aperture diameter $5mm$, base plate temperature $60°C$). The lines give the melt front for different times (from 0.8 to 24 seconds after release of the melt. The axis are given in unit of $[mm]$.

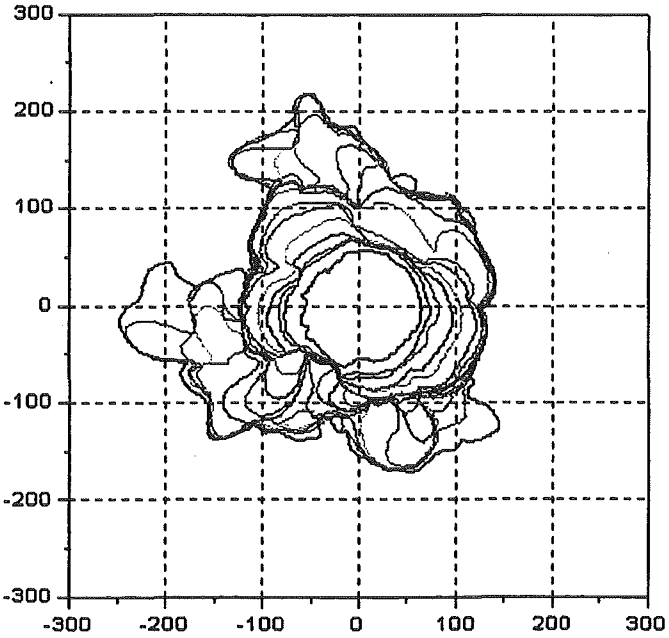

Figure 27: Sequence of the single phases of spreading for nonisothermal conditions (aperture diameter $5mm$, base plate temperature $4°C$). The axis are given in unit of $[mm]$.

The time increment between two melt front lines increases from $\Delta t = 0.7s$ at the beginning (most inner line) to $\Delta t = 2.5s$ at the end of an experiment.

The results of the experiments

The results of the experiments can be divided into two main groups:

1. Results concerning the size of the spreading area (figures 28, 29), average radius (figures 30, 31) and the circumference (figures 32, 33) of the melt body;
2. Results concerning the size of the hydraulic jump radius.

Spreading area, average radius and circumference

On the following pages, one can see the results for the size of the spreading area, the average radius and the circumference, each value in time. In case of the average radius and the circumference, the values for an ideal circle are shown too (spreading area is set equal to the circle area).

Spreading area - 5 mm aperture

If we have a look at the curves of the spreading area versus time, we can see a remarkable difference between isothermal and non-isothermal spreading. In case of the 5 *mm* aperture and non-isothermal spreading (temperatures between 4°*C* and 40°*C*), the base plate temperature has no significant influence on the size of the spreading area. The slope of the curves is identical for all experiments in a first phase, a separation of the curves develops after approximately 10 seconds. The spreading area occurs generally smaller in non-isothermal spreading, from starting. The size of the spreading area of the solidified melt after the experiment is nearly twice as large in isothermal spreading compared to non-isothermal spreading. The initial mass of the melt has only little influence on the spreading area. More melt mass does not always cause a greater spreading area. A first explanation of this weak influence can be given from the comparison of volumetric flow rate for different melt mass (cf. page 26). Here, a larger initial mass leads to a slight increase of the volumetric flow rate. In the non-isothermal case, the higher amount of melt is transformed mostly into a thicker layer of melt. The height of the melt above the base plate h_{melt} has also little influence on the size of the spreading area.

Spreading area - 10 mm aperture

In case of the 10 *mm* aperture we see other dependencies of the behaviour of the spreading melt. Here, too, we have the largest spreading areas for isothermal spreading. In contrast to the 5 *mm* aperture, the size of the spreading area now depends on the base plate temperature for non-isothermal spreading. It is furthermore remarkable that at a base plate temperature of 4°*C* leads to larger melt bodies than at medium temperatures like for example 40°*C*. The reason may be found in a thin layer of condensed water which formed on the surface of the base plate for a temperature of 4°C. It appears because of the great temperature decrease from base plate to the ambient air (approx. 35°C). The slope of the spreading curves is identical for all experiments with the 10 mm aperture, one cannot see a difference between isothermal and non-isothermal spreading. The initial mass of melt has more influence on the size of the spreading area in this case compared to the 5 mm aperture. The reason is the strong increase of the volumetric flow rate when the mass of melt is increased. The height of the melt above the base plate has almost no influence on the spreading area. This is similar to the experiments with the 5 mm aperture.

Radius and circumference - 5 mm and 10 mm aperture

The curves for radius and circumference versus time are displayed together with the curves for an ideal circle (dashed lines). To determine the size of an ideal circle, the spreading area is assumed equal to the circle area. If one compares both values, the real and the ideal ones, one can see that the values for the average radius are close to the ideal (circular) radius. This indicates that all melt bodies are nearly circular. In cases where there is a significant difference (max. 10 percent), we have a deformed melt body, mostly a jolted and elongated form (for example experiment no. 19). In case of the values for the circumference, the comparison between solid and dashed lines gives a hint for the amount of fingering at the melt front. If there is a big difference between ideal and real values, we can conclude that the melt body features a lot of fingers (one compare the curves for experiment no. 11). This effect appears specially for non-isothermal experiments. One can also see, that it takes some time before the appearance of first fingers, marked by a fast initial increase of the circumference (experiments no. 11, 17 and 19). In 'normal' cases (isothermal spreading with few or no fingers formed), the slope of radius and circumference curves behaves similar to the curves of the spreading area. In fact, the differences in slope are often in the range of the approximation error (circumference).

The figures 28-33 show the results for all experiments depending on time.

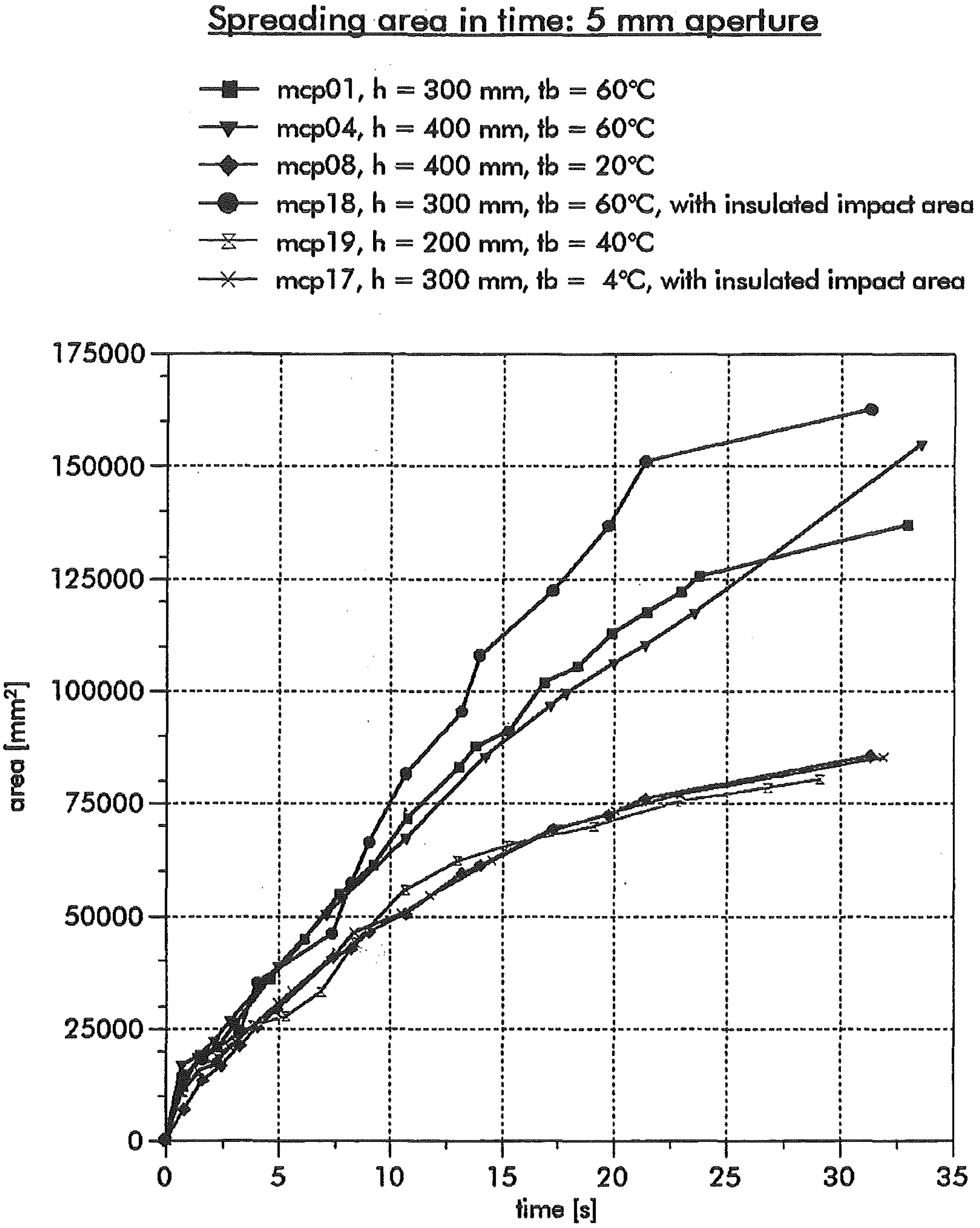

Figure 28: Results for the spreading area - 5 *mm* aperture.

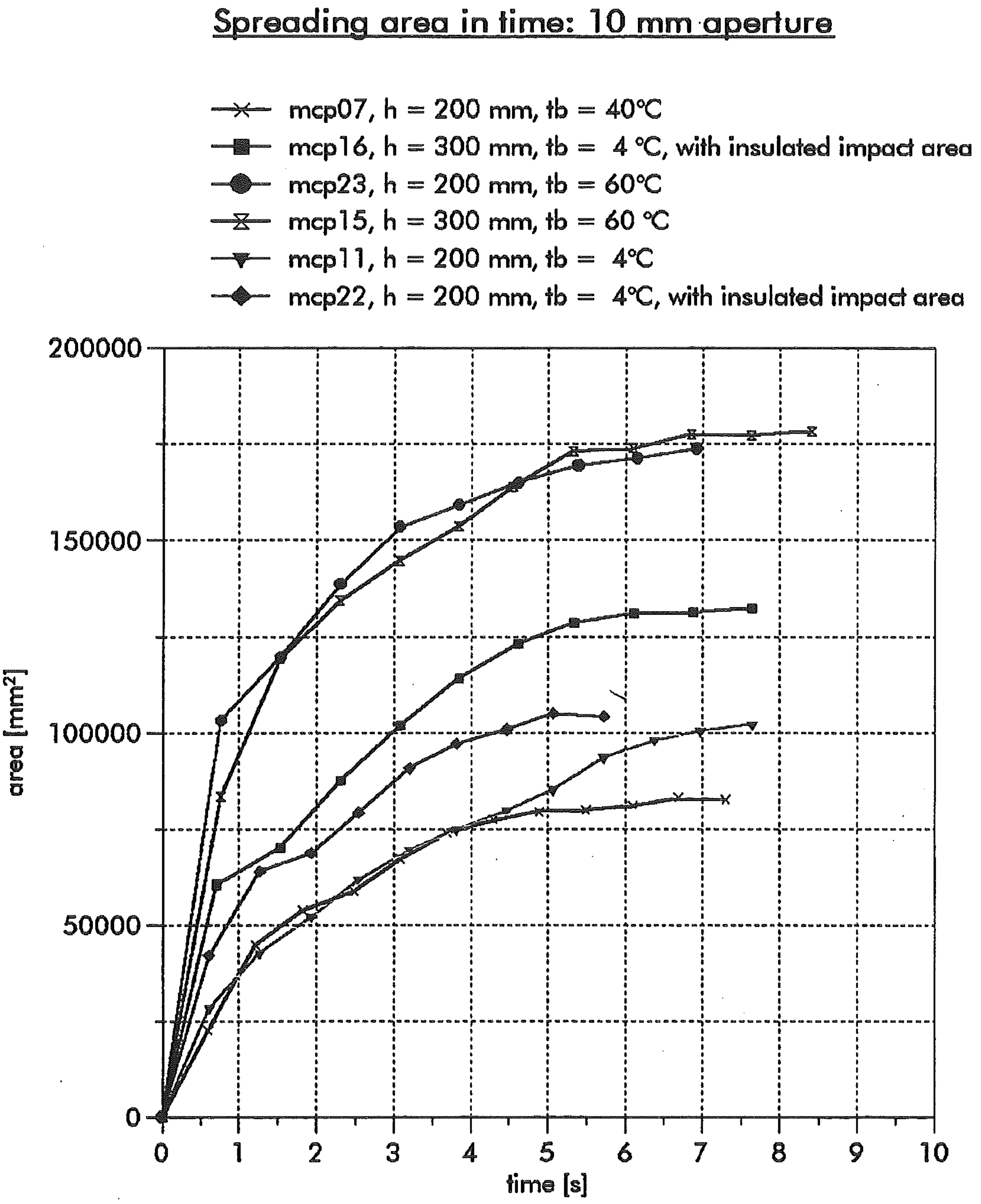

Figure 29: Results for the spreading area - 10 *mm* aperture.

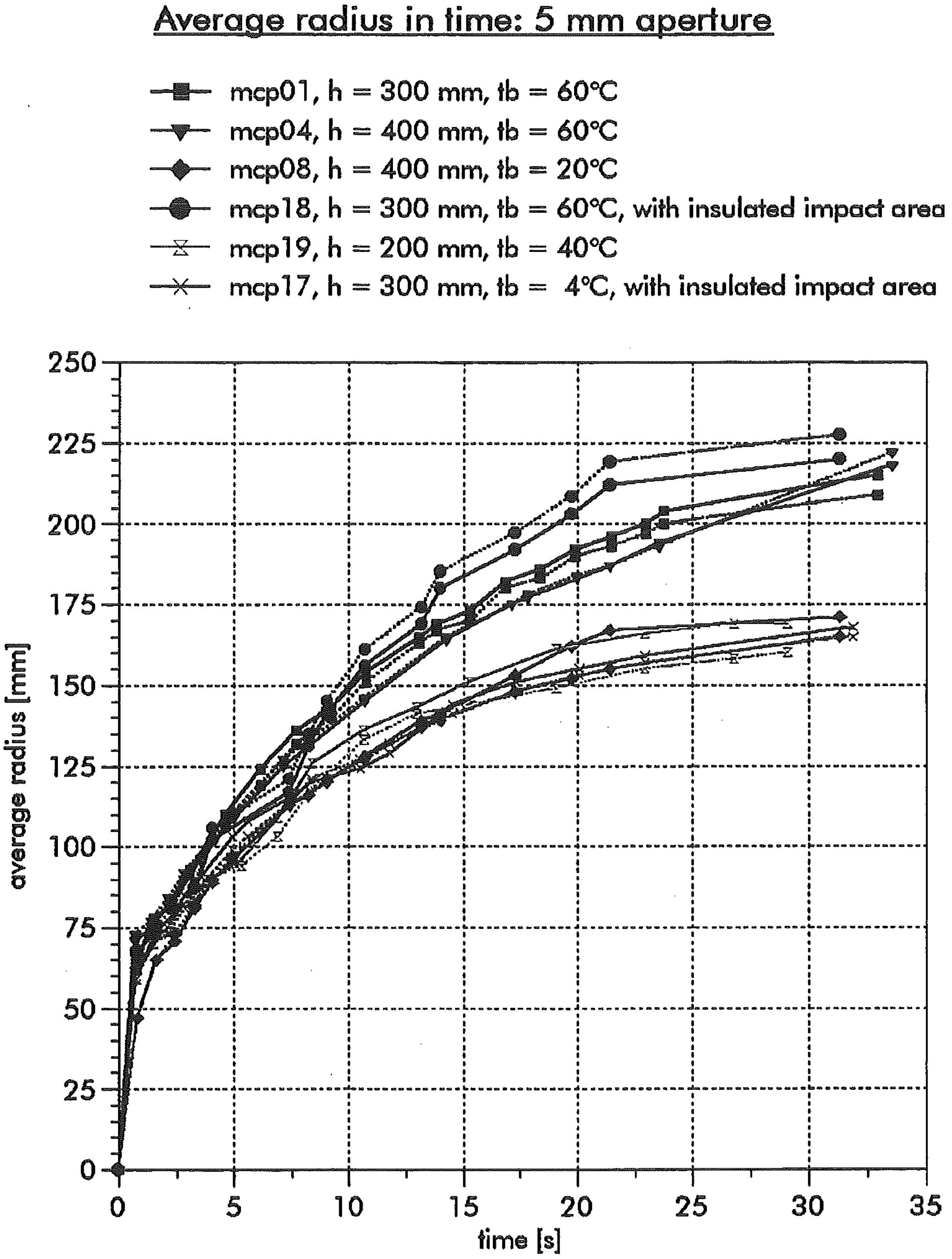

Figure 30: Results for the average radius - 5 *mm* aperture.

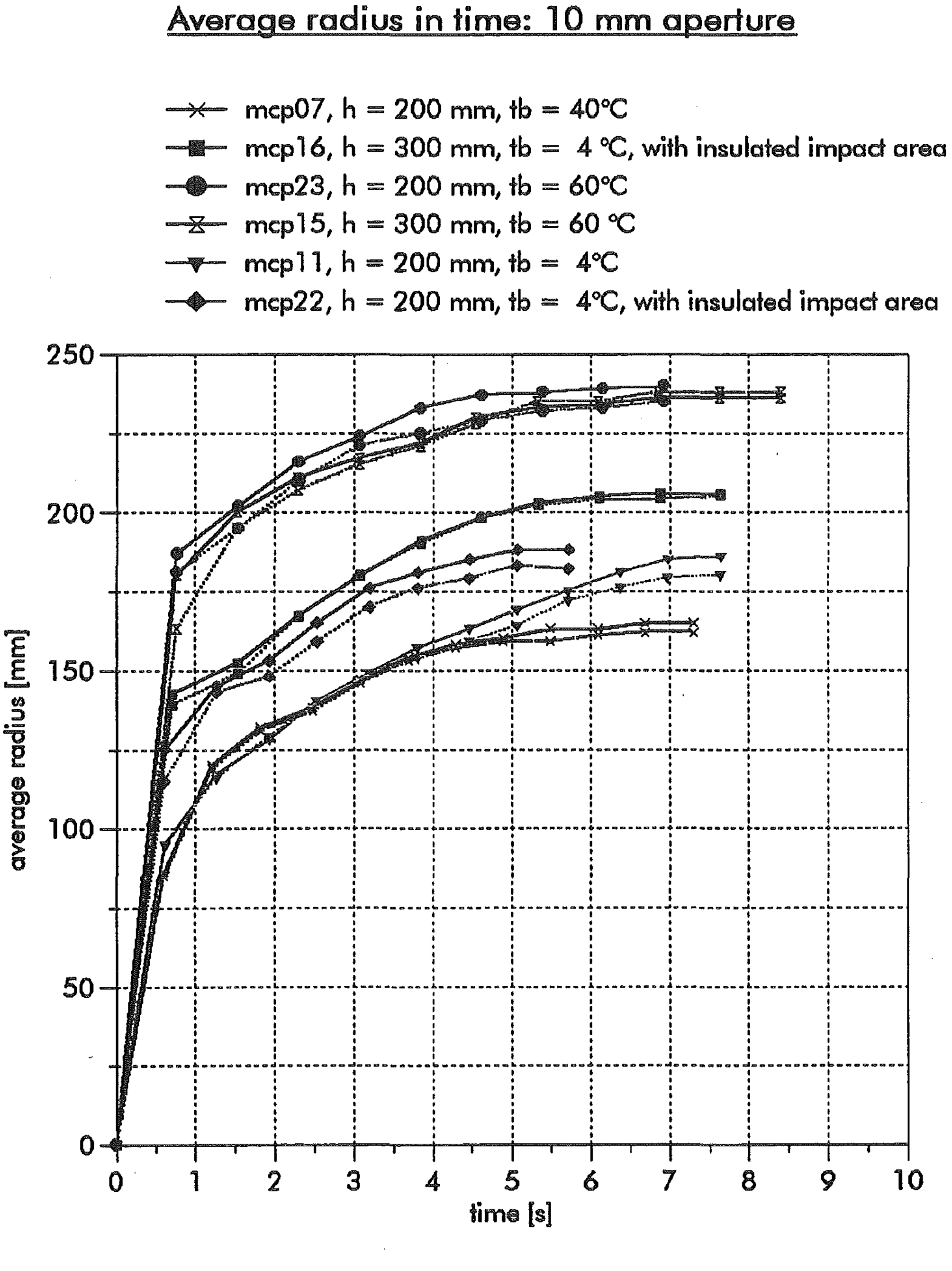

Figure 31: Results for the average radius - 10 *mm* aperture.

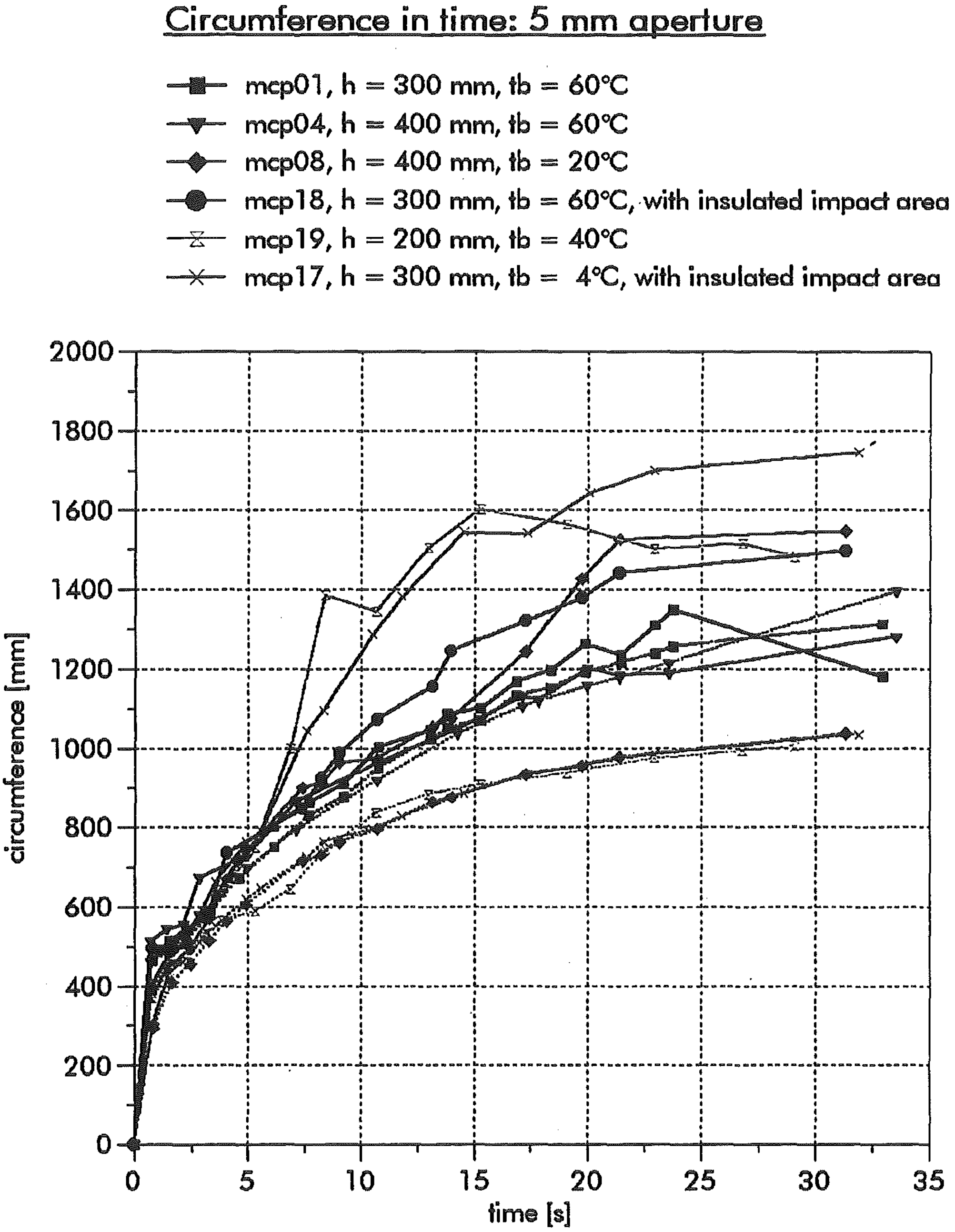

Figure 32: Results for the circumference - 5 *mm* aperture.

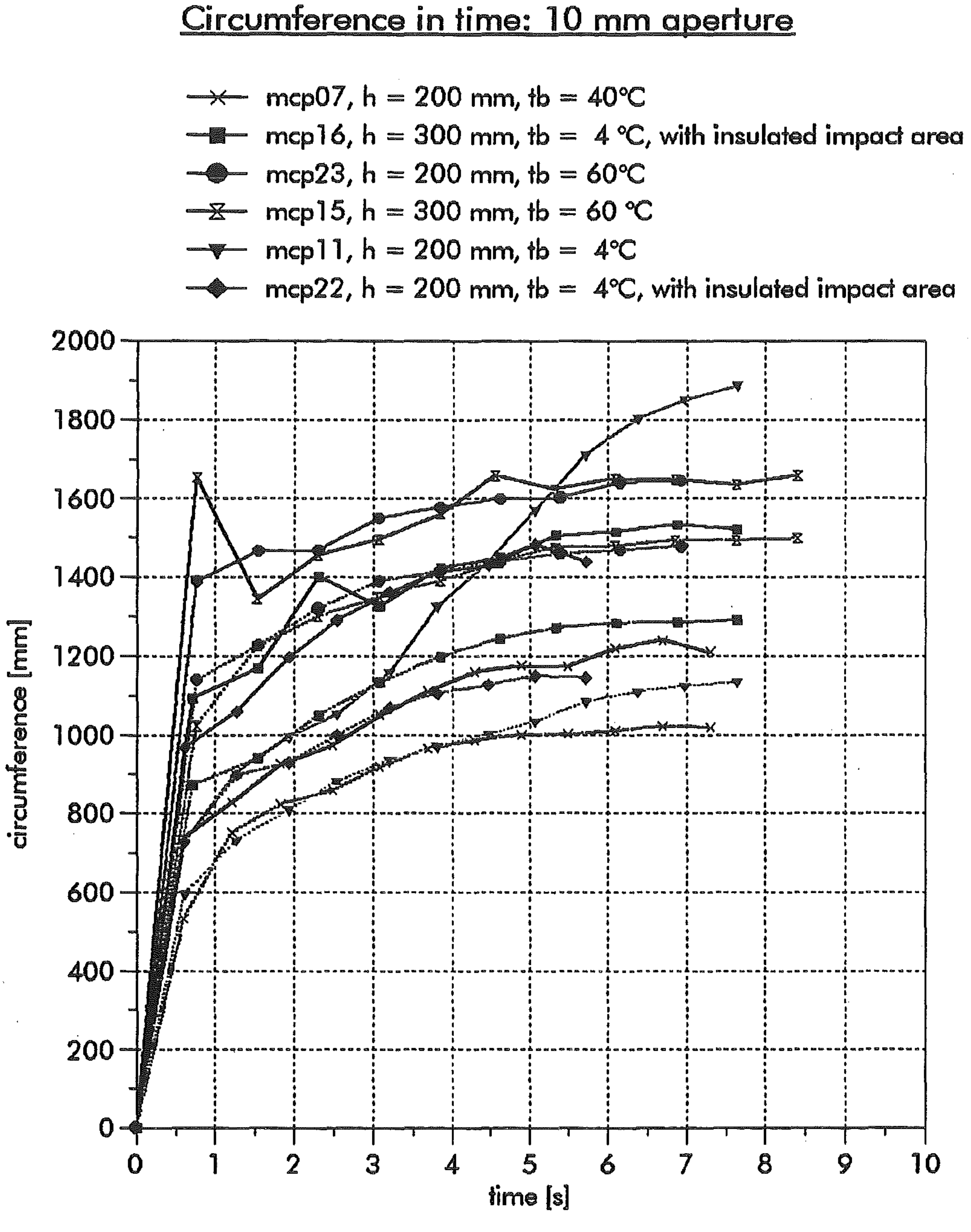

Figure 33: Results for the circumference - 10 *mm* aperture.

Spreading area, average radius and circumference - 2 mm aperture

With the 2 *mm* aperture, only a few experiments have been done. The reasons are:

- Very slow spreading because of the low volumetric flow rate, sometimes non-continuous spreading (pulsating, compare description of experiment no. 5);
- No hydraulic jump formed;
- The interpolation points do not have to decrease or to increase monotonously;
- Spreading is strongly influenced by the adjustment of the base plate (small abberations from the horizontal position causes a directed flow);
- Non-isothermal experiments difficult to evaluate because of the thickness of the melt body (up to 2-3 centimeters).

The results of these experiments are summarized in the figure below. All values are normalized in the following way:

$$\text{spreading area:} \qquad a = \frac{\text{actual area}}{\text{final area}};$$

$$\text{circumference:} \qquad c = \frac{\text{actual circumference}}{\text{final circumference}};$$

$$\text{radius:} \qquad r = \frac{\text{actual radius}}{\text{final radius}}.$$

In figure 33, we can see the spreading characteristics of the melt as a function of time when a 2 *mm* aperture is used. The slope of the curve for the spreading area is nearly linear for isothermal spreading, the volumetric flow rate can be taken to be constant over a long period. The behaviour of radius and circumference is corresponding. As mentioned before, the spreading is non-continuous in a later phase of the experiments (second half). A stepwise behaviour, as qualitatively indicated in figure 33 is present. The few data points taken in time do, however, not allow to reproduce this behaviour exactly . The curves of the non-isothermal experiment no. 09 show some special properties and it can be viewed as representative for all non-isothermal experiments with the 2 mm aperture. The spreading area grows normally in the first half of the experiment, and then solidification starts and the spreading is prevented for some time. The melt body grows in height during this period, the result is a rather thick melt body. These experiments do not give too useful information and, therefore, no further experiments have been performed.

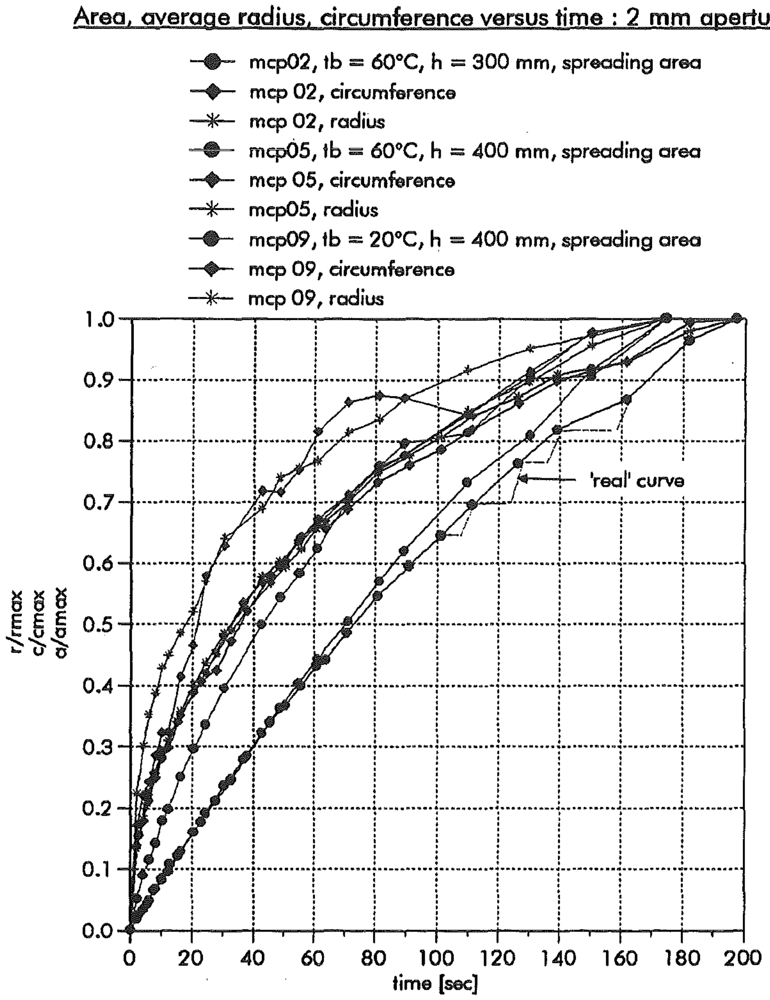

Figure 34: Results for 2 *mm* aperture.

Experiment	area $[mm^2]$	circumference $[mm]$		average radius $[mm]$	
	real	real	ideal	real	ideal
mcp02	138498	1407	1319	215	210
mcp05	128636	1353	1271	204	202
mcp09	57363	1203	849	136	135

Table 9: Final sizes of area, circumference and average radius.

Approximation functions for the spreading area

The curves for the spreading area can be approximated by power law functions. The spreading area (and consequently the average radius) depends on time t and volumetric flow rate Q. A function that fits the experimental behaviour is of the type:

$$A = c_1 Q^{c_2} t^{c_3} \quad ,$$

where A represents the spreading area, Q the volumetric flow rate and t time. The size of the spreading area can easily be replaced by the radius (as seen before, radius calculated with spreading area corresponds good with measured values). In case of the 5 *mm* aperture, only two approximations are done, one for the isothermal case and one for the non-isothermal case. The experiments with the 10 *mm* aperture are all approximated by separate functions. The constants c_1, c_2 and c_3 are listed in table 10.

diam.	temp. $°C$	experiment	c1	c2	c3
5 *mm*	4	mcp17	0,06860	0,17258	0,64869
	20	mcp08	0,02609	0,09127	0,68932
	40	mcp19	0,06986	0,16954	0,80179
	60	mcp01	0,06442	0,16955	0,80179
	60	mcp04	0,01109	-0,01949	0,68258
	60	* mcp18	0,05732	0,14871	0,81135
10 *mm*	4	mcp11	0,04563	0,02247	0,53022
	4	mcp16	0,15691	0,10188	0,45178
	4	* mcp22	0,14255	0,11594	0,48113
	40	mcp07	0,32383	0,23561	0,56863
	60	mcp15	0,14580	0,04249	0,33371
	60	mcp23	0,21290	0,07241	0,29186

Table 10: Constants c_1, c_2 and c_3 of the approximation functions.

The isothermal experiments with the 5 *mm* aperture are represented by mcp01, the non-isothermal experiments by mcp17. The experiments with the 2 *mm* aperture are excluded from this approximation. A correlation of the constants c_1, c_2, c_3 and the outlet conditions, respectively the spreading conditions, does not occur obvious. A first view on the constants gives no fitting point for a dependence on these parameters. The diagrams with the approximated time behaviour curves are displayed in figure 35 and figure 36.

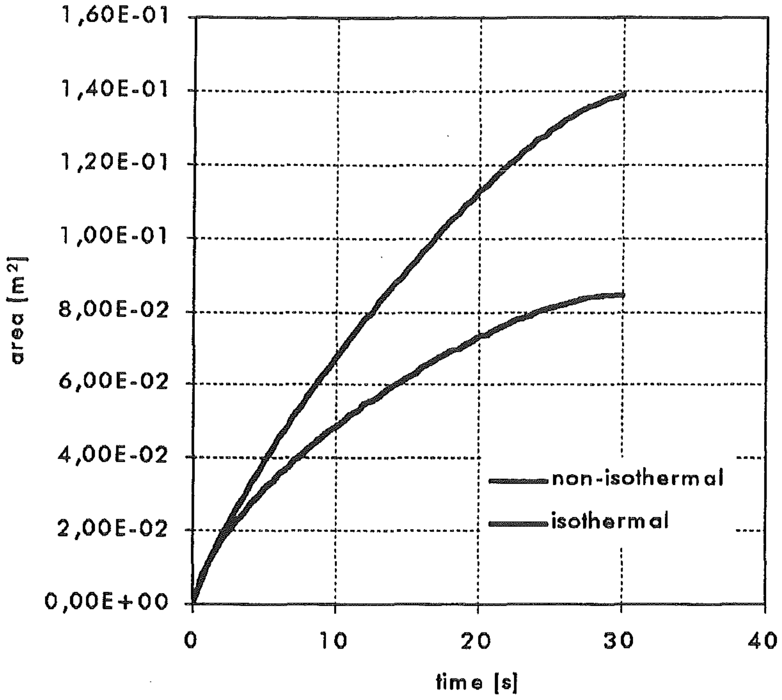

Figure 35: Approximated curves for spreading area - 5 *mm* aperture.

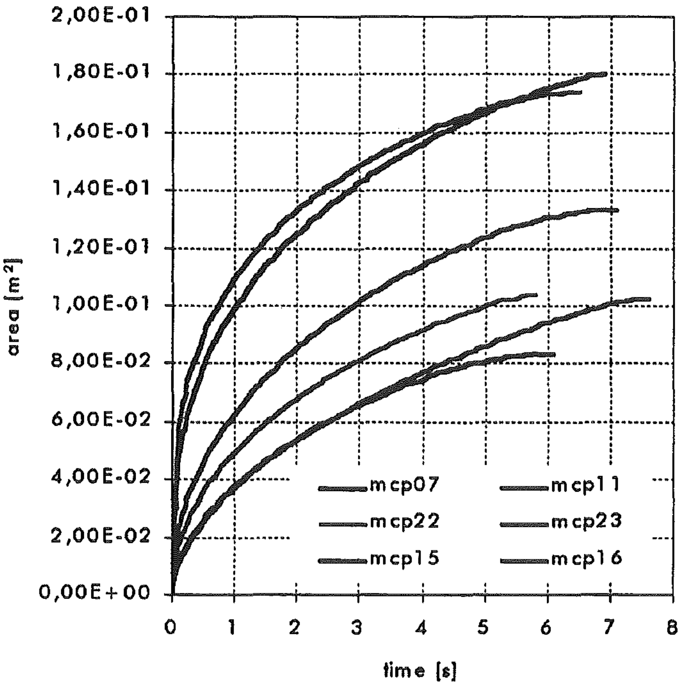

Figure 36: Approximated curves for spreading area - 10 *mm* aperture.

The hydraulic jump radius

The hydraulic jump appears when the liquid jet impinges on the horizontal plate and spreads radially outward. One can observe a shooting flow area around the impact area. This is characterized by a thin fluid layer and by high flow velocities. At a critical radius, the shooting flow transits into a streaming flow. The transition itself is not smooth, in fact there is a sudden jump of height of the fluid layer and in the flow velocity. A detailed description of the flow structure and the phenomena can be found in [3]. This phenomenon can be observed in all experiments, except if a 2 *mm* aperture is used. In the latter case, the volumetric flow rate is too low to form a shooting flow and, thus, no hydraulic jump occurs.

The hydraulic jump radius - 5 mm aperture

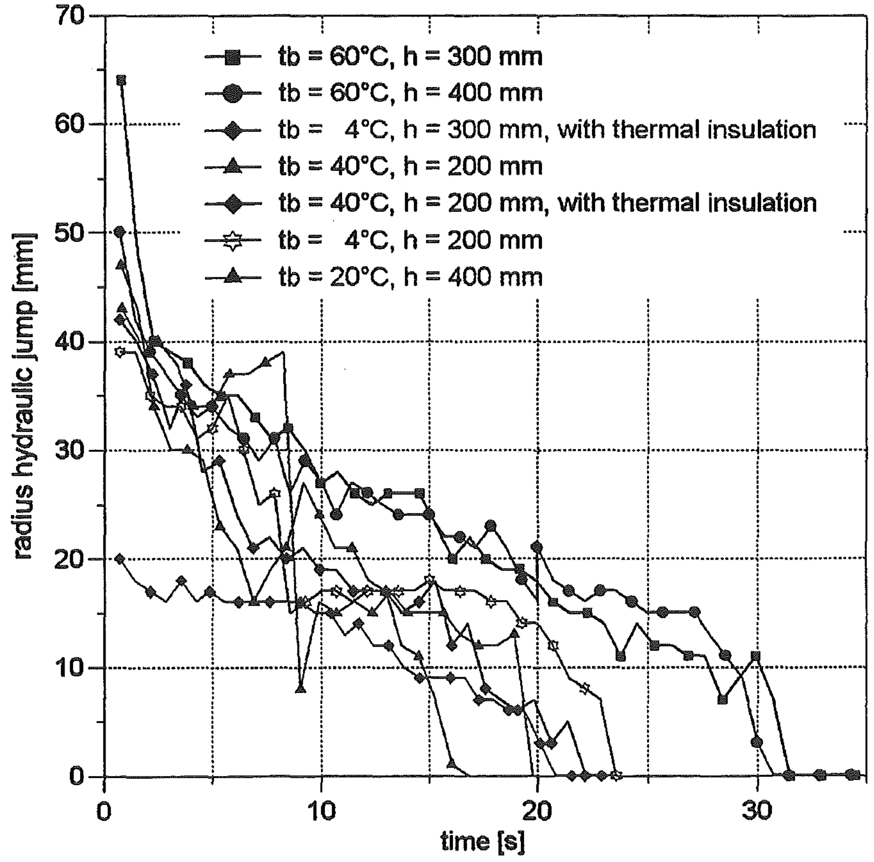

Figure 37: Hydraulic jump radius in time for the experiments with the 5 *mm* aperture.

In figure 37, the results for the 5 *mm* aperture are displayed. All curves are recorded starting from $t \approx 1,5s$ after impact. The recording of the first image is not simultaneously done with the impigment of the liquid jet. During the first second, the radius of the hydraulic jump decreases very fast. In this period, the measured radius depends strongly on the instant of the first image. As there is no synchronisation this would lead to false conclusions. Thus, we exclude the first measured data and discuss the situation in a later stage.

As in the case of the spreading area, the hydraulic jump radius depends strongly on the base plate temperature. One can see a distinct difference between isothermal (red and black curve) and non-isothermal conditions. In the isothermal case the hydraulic jump is present almost until the end of the experiment. Its time behaviour corresponds well with the volumetric flow rate (cf. figure 19). An influence of the height of the melt above the plate cannot be determined.

In the non-isothermal case, we can clearly see a dependence of the hydraulic jump radius on the base plate temperature. In all cases, the hydraulic jump radius decreases first, then it increases followed by a period of fast decrease. Then the radius remains remarkably constant for some time before it disappears. This observation is true at lower base plate temperatures, while in case of a base plate temperature of $40°C$, this effect is not seen. The re-increase of the jump radius starts later for larger plate temperatures. A possible explanation for this effect is the solidification of the melt in the area of the shooting flow. Solidification in this area reduces the ratio of the heights of the fluid layer before and after the hydraulic jump This leads to a relocation of the jump outwards. Generally, the jump disappears after approximately two-thirds of the duration of the spreading experiment.

Some experiments are done with a thermally-insulated impact area (compare the description of the respective experiments mcpl0/17 and mcpl9/20). The influence of the thermal insulation on the behaviour of the hydraulic jump radius is shown in figure 38. We can see that the thermally insulated impact area leads to a more regular decrease of the hydraulic jump radius. The trend of the curves is again closely-linked to the volumetric flow rate.

The hydraulic jump radius - 10 mm aperture

In case of the 10 *mm* aperture, the hydraulic jump radius depends also on the kind of spreading (isothermal or non-isothermal). The results for the hydraulic jump radius are shown in figure 38 In the non-isothermal case, the jump radius is remarkably smaller. The differences between various non-isothermal experiments are clearly related to the different starting mass, respectively the different volumetric flow rate at the beginning of each experiment.

The temperature of the base plate itself has no significant influence on the behaviour of the jump. The influence of the height of the melt above the base plate is also very low in this case. The trend of the curves again is similar to the behaviour of the volumetric flow rate. The geometric form of the hydraulic jump is only in the late phase of each experiment circular, in an early stage the form changes from rotating ellipses to irregular shapes. This behaviour is caused by the high volumetric flow rate, which partly occurs to be not perfectly axissymmetric. A higher volumetric flow rate leads to a larger area of shooting (supercritical) flow and consequently to a greater radius of the hydraulic jump.

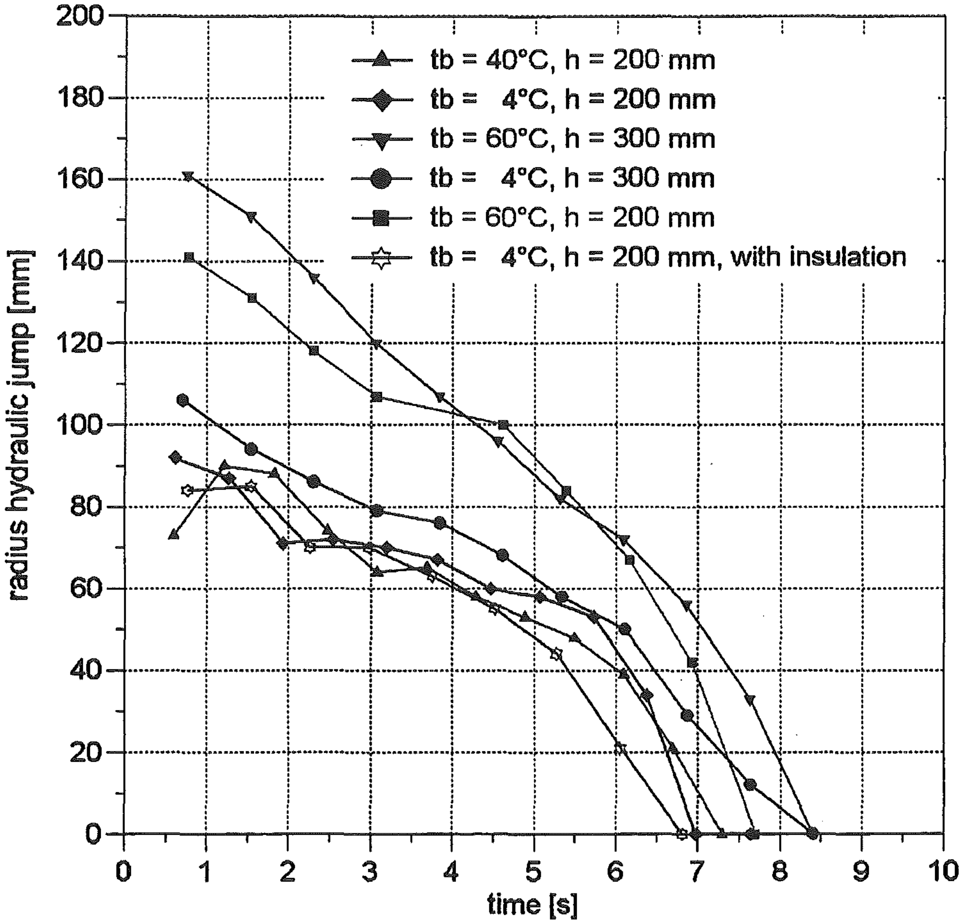

Figure 38: Hydraulic jump radius in time for the experiments with the 10 *mm* aperture.

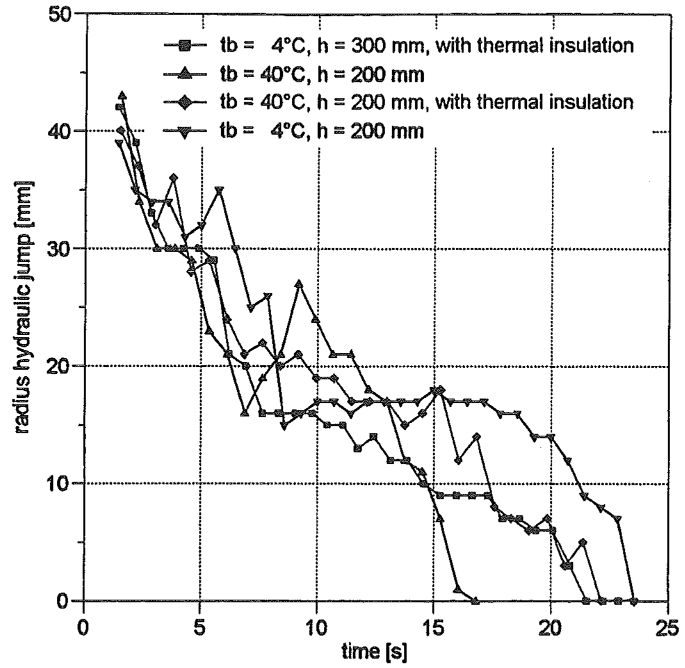

Figure 39: The hydraulic jump radius in time with and without thermally-insulated impact area, aperture diameter 5 *mm*.

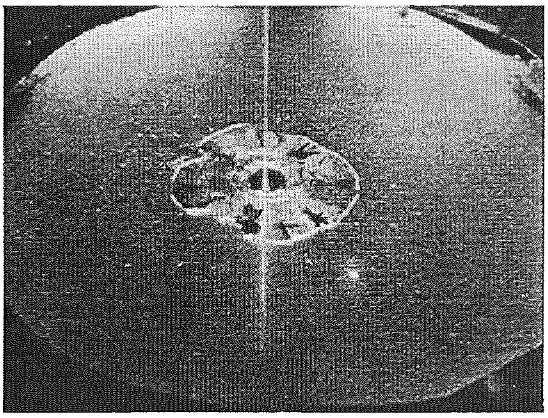

Figure 40: Hydraulic jump with insulated impact area

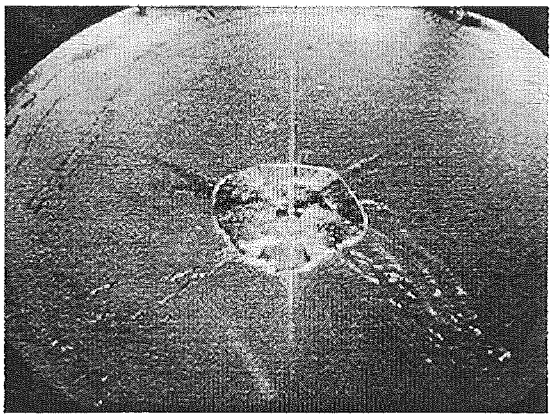

Figure 41: Hydraulic jump without insulated impact area. One can see the small melt pieces thrown out of the center (caused by solidification at the impingment point.

Characteristic quantities of the flow

The flow velocity

Jet velocity at outlet aperture

The flow velocity at the outlet aperture can be calculated with the knowledge of the volumetric flow rate and the outlet geometry. We have

$$u_{jet,1} = \frac{4\dot{V}}{d^2\pi}$$

where d the diameter of the outlet aperture. The flow velocity is time-dependent and its maximum value is $u_{jet,1} = 1,585 m/s$ for the 10 mm aperture and $m_0 = 6,5 kg$.

The values for the other cases are

$u_{jet,1} = 1,495 m/s$ for the 10 mm aperture and $m_0 = 5,0 kg$
$u_{jet,1} = 1,556 m/s$ for the 5 mm aperture and $m_0 = 6,5 kg$
$u_{jet,1} = 1,358 m/s$ for the 5 mm aperture and $m_0 = 5,0 kg$

The liquid jet is accelerated by gravity after passing through the outlet aperture. The difference in velocity depends on the height of the melt container above the base plate. If the height of the melt is 300 mm, the jet velocity is increased by

$$u_{jet,2} = \sqrt{2 h_{melt} g}$$

where h_{melt} is the height of the melt container above the base plate and g the gravitational acceleration. The values are

$u_{jet,2} = 2,801 m/s$ for $h_{melt} = 400 mm$,
$u_{jet,2} = 2,426 m/s$ for $h_{melt} = 300 mm$,
$u_{jet,2} = 1,980 m/s$ for $h_{melt} = 200 mm$.

The resulting jet velocity before redirection into horizontal flow on the base plate is the sum of both partial velocities, i.e.

$$u_{jet} = u_{jet,1} + u_{jet,2}$$

For heights of 300 *mm* and 200 *mm* over the base plate, the jet velocity is displayed in dependence of time in figures 40 and 41.

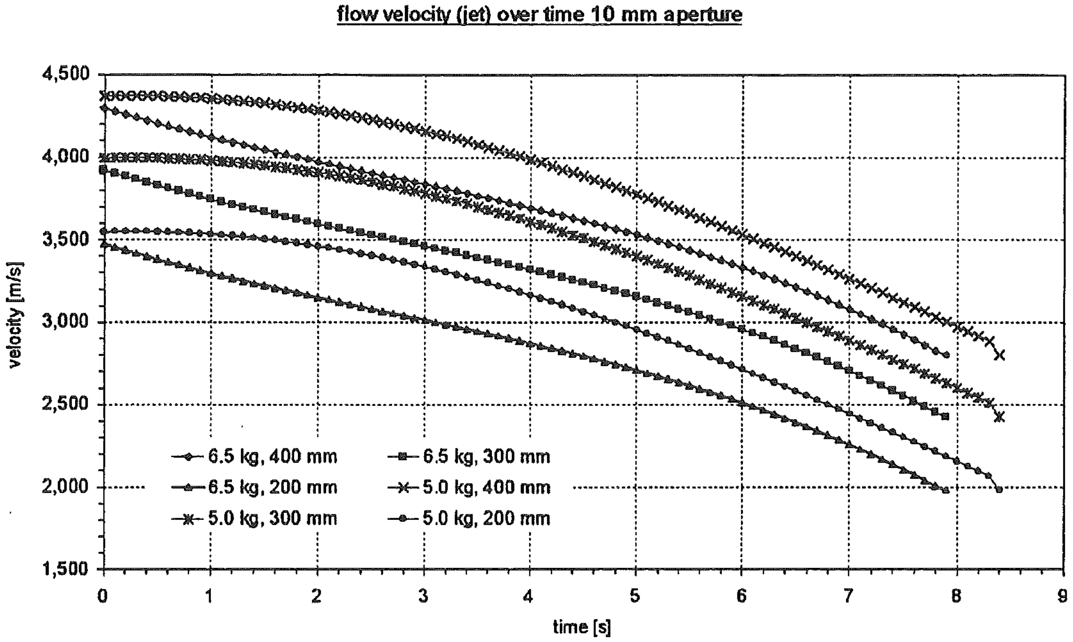

Figure 42: Flow velocity in time - 10 *mm* aperture.

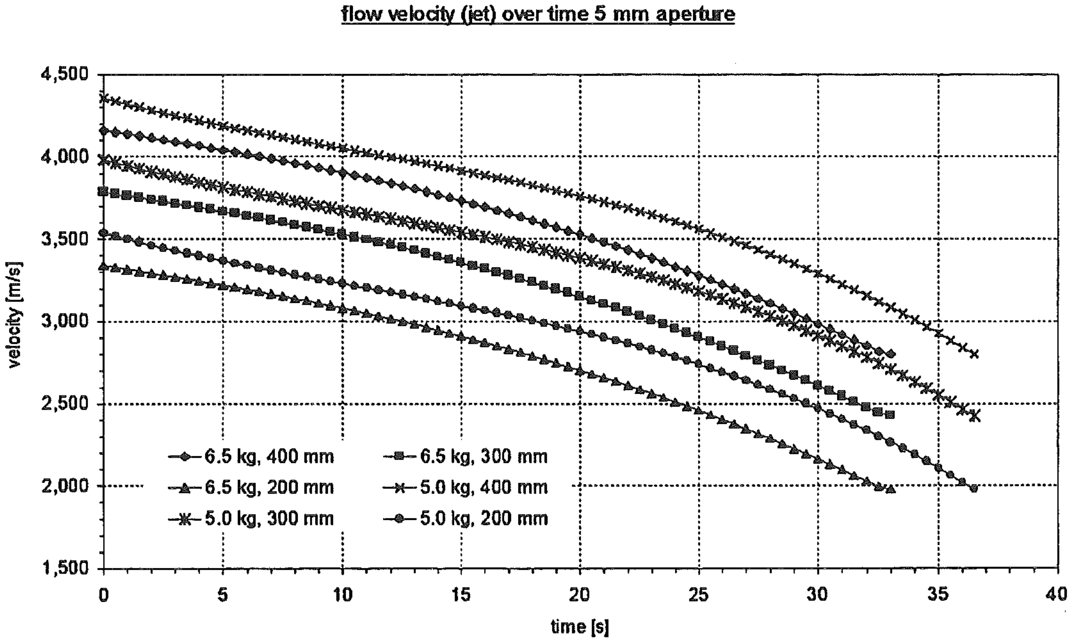

Figure 43: Flow velocity in time - 5 *mm* aperture.

Flow velocity on the base plate

The flow velocity on the base plate depends both on time and on location. The exact value of the flow velocity cannot be determined because an important information is missing: the height of the fluid layer. An average height of the fluid layer can be estimated based on the spreading area and the mass of melt. The major problem in estimating the height of the fluid layer is the ratio of heights before and after the hydraulic jump. For this point, several assumptions for the flow have to be made:

- The thickness of the fluid layer in the area of the shooting flow is assumed to be constant at all times during the experiment;
- The Froude-Number Fr has to be $Fr > 1$ in the area of the shooting flow and $Fr < 1$ behind the hydraulic jump (definiton see page 49);
- Behind the hydraulic jump, the thickness of fluid layer is time dependent;
- The integral volumetric flow rate is identical at each radius (inside and outside the hydraulic jump);
- The melt spreads axisymmetrically.

In general, the average height of the fluid layer can be calculated as follows:

$$h = \frac{m}{\rho A},$$

where A is the size of the spreading area and m the mass of melt on the plate. The thickness h is an average value, in fact we have two different heights, one for the shooting fluid layer and one for the streaming fluid layer behind the hydraulic jump. To meet the assumption of a constant fluid height inside the hydraulic jump, the ratio of heights h_{sh}/h_{str} has to be set $h_{sh}/h_{str} = 0.2$. The assumption of a constant height is only justified for isothermal experiments, for non-isothermal experiments, we may have solidification of the melt inside the hydraulic jump. If we neglect the amount of melt inside the hydraulic jump, the height of the fluid layer outside the hydraulic jump can be calculated based on the mass of melt on the plate. We assume an average height inside the hydraulic jump of 0.5 to 0.6 mm for the experiments with the 5 mm aperture and 0.3 to 0.4 mm for the experiments with the 10 mm aperture. For $Fr = 1$, the height has to be around 1 mm. For the isothermal experiments with the 5 and 10 mm aperture, the averaged flow velocities on the base plate are given by

$$v = \frac{\dot{V}}{2\pi h} \quad .$$

The detailed calculation of the velocity is done for the two isothermal experiments mcp01 (5 *mm* aperture) and mcp23 (10 *mm* aperture). The results are shown in figures 44 and 45. The dotted line segments mark the actual position of the hydraulic jump, the heights on both sides of the jump are estimated based on the above assumptions.Thus, the velocities are really based on these estimates and are averaged across the melt layer.

Flow velocities on the base plate

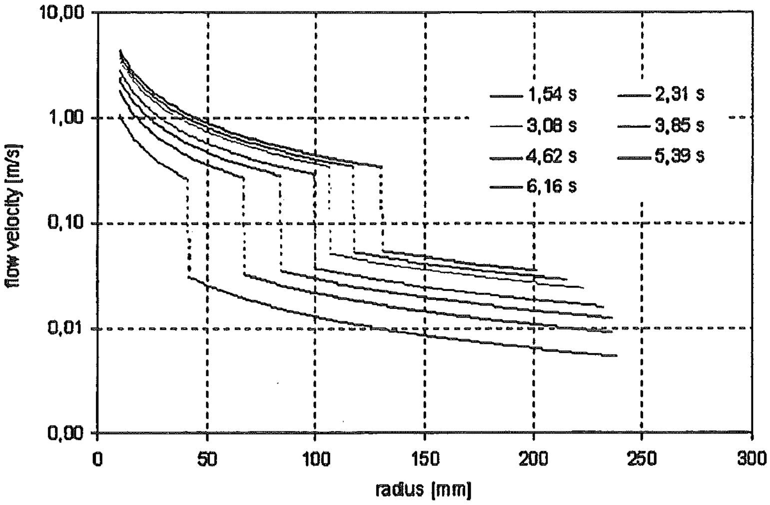

Figure 44: Flow velocity base plate (ap. diam.= 10 mm, $t = 60°C$, $h_{melt} = 200\,mm$).

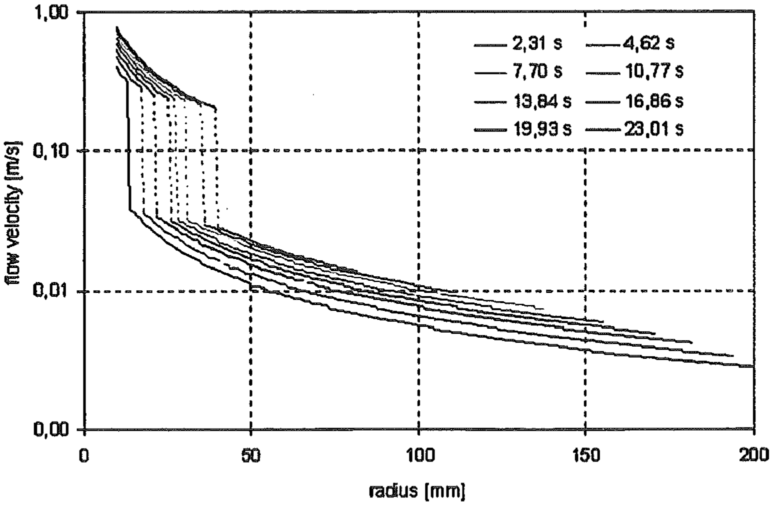

Figure 45: Flow velocity base plate (ap. diam.= 5 mm, $t = 60°C$, $h_{melt} = 300\,mm$).

The estimated height of the fluid layer in the area of the shooting flow is 0,35 *mm* (10 *mm* aperture) respectively 0,56 *mm* (5 *mm* aperture). The following calculations of the Reynolds- and Froude-number are based on these velocity results.

The Reynolds- and the Froude-number

The Reynolds- and the Froude-number depends both on volumetric flow rate (consequently on time) and the position. Around the impignition point, we have the greatest values of both numbers. The Reynolds-number decreases to zero during the spreading process. The equations for the determination of the Reynolds- and Froude-number are [2]:

$$Fr = \frac{v}{\sqrt{gh}} \qquad Re = \frac{vh}{\nu}$$

If we set $v = \frac{\dot{V}}{2\pi r h}$,we obtain

$$Fr = \frac{\dot{V}}{2\pi}(gh^3)^{-\frac{1}{2}} \qquad Re = \frac{\dot{V}}{2\pi\nu} \quad .$$

The above equations clarify that the Froude-number remains an estimation, as it is based on the estimated liquid height h. In contrast, the Reynolds-number is directly linked to the measured flow rate and, thus, well known. The diagrams in the figures 46-49 show both dimensionless groups, *Re*, *Fr* as function of radius, and as function of time.

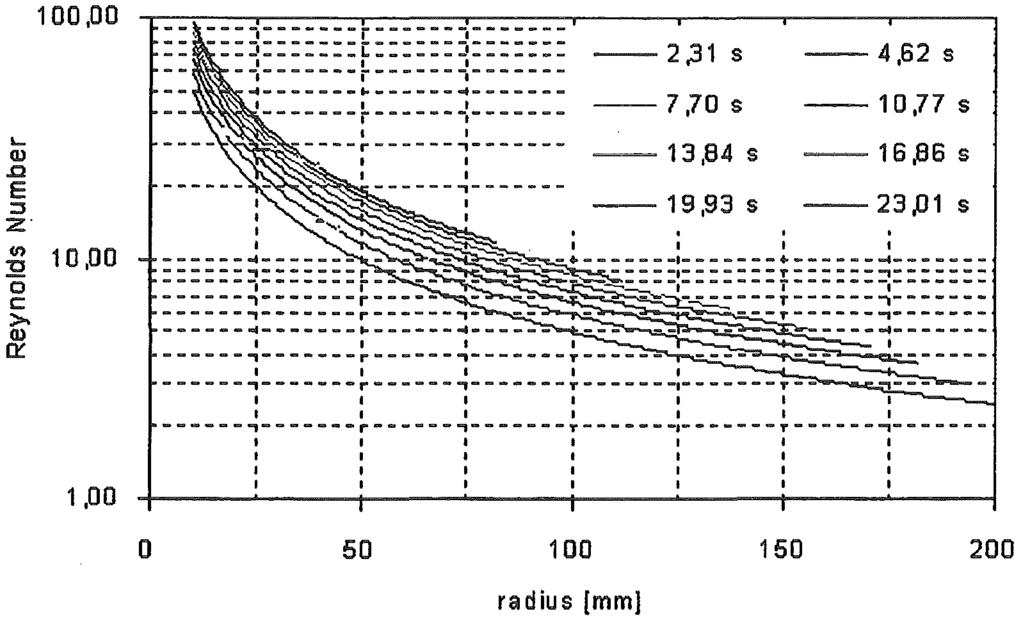

Figure 46: The Reynolds-number for experiment mcp01 (ap. diam.= 5 mm, $t = 60°C$, $h_{melt} = 300\,mm$).

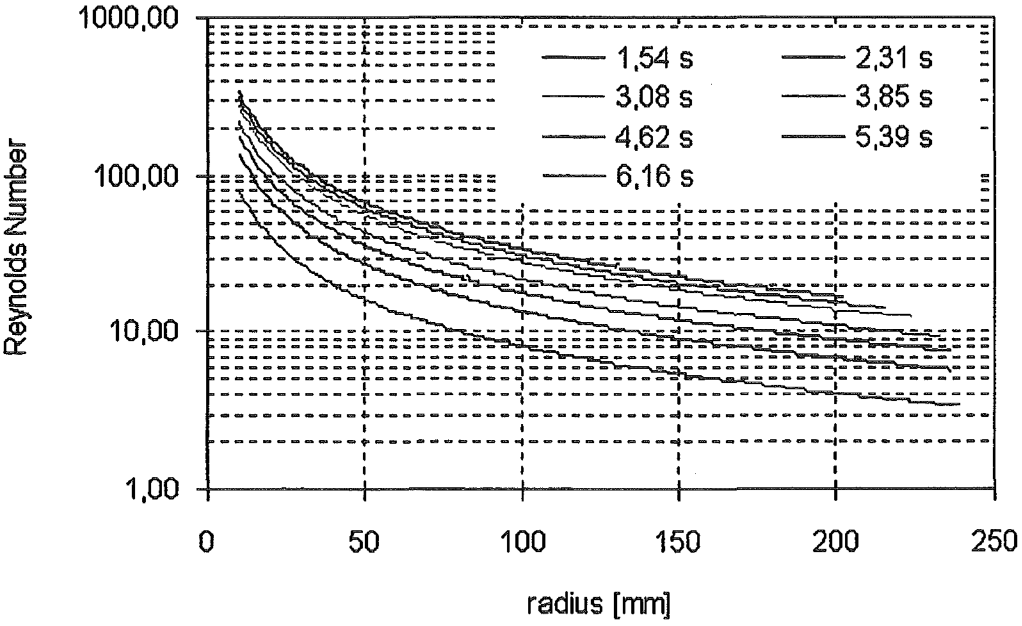

Figure 47: The Reynolds-number for experiment mcp23 (ap. diam.= 10 mm, $t = 60°C$, $h_{melt} = 200\,mm$).

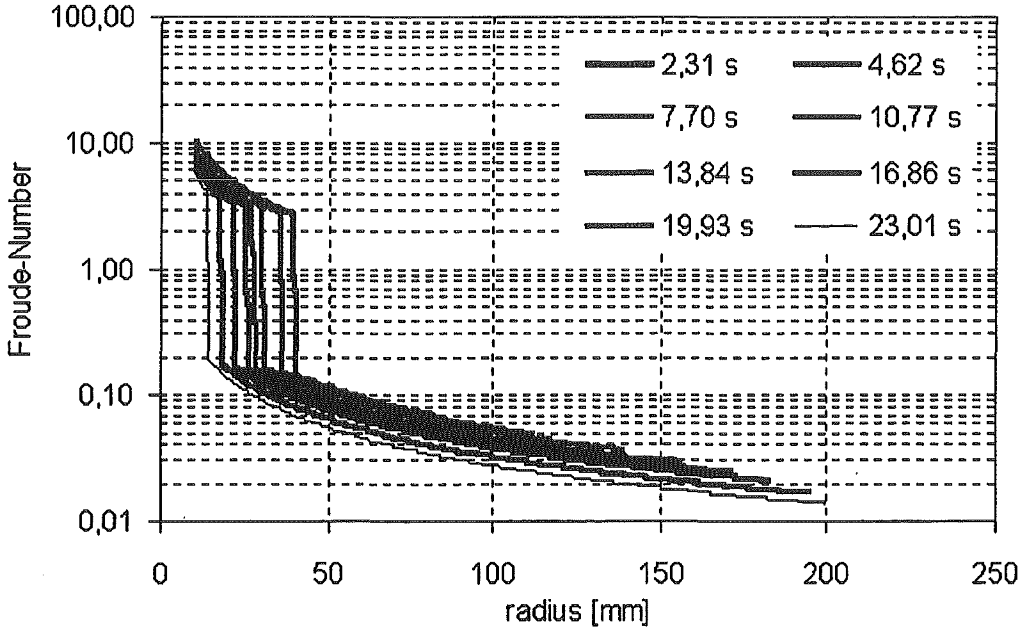

Figure 48: The Froude-number for experiment mcp01 (ap. diam.= 5 mm, $t = 60°C$, $h_{melt} = 300\,mm$).

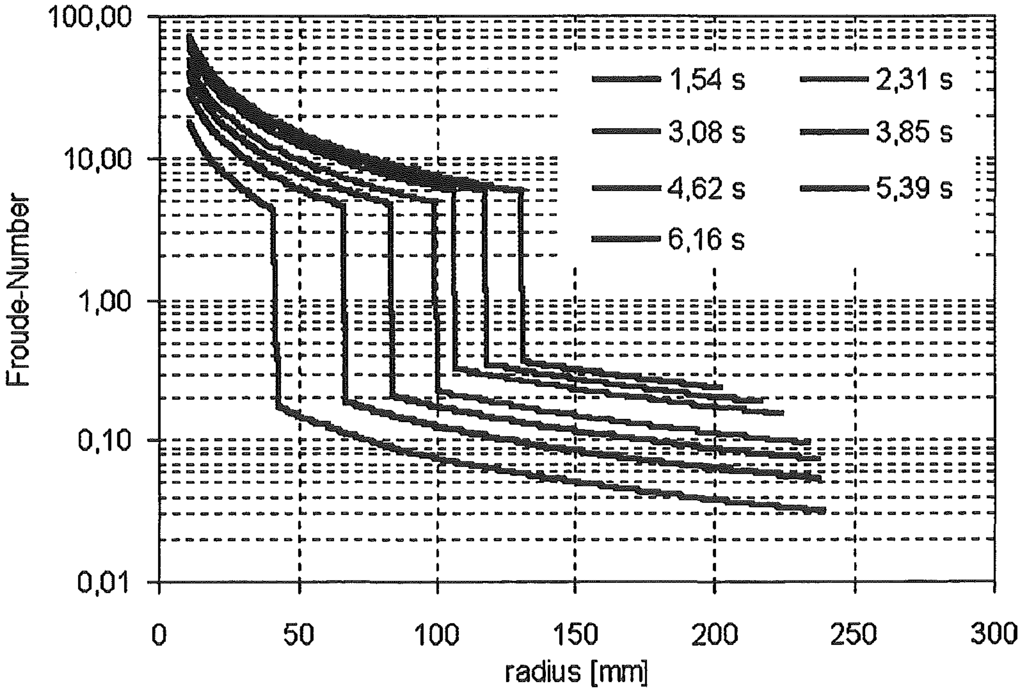

Figure 49: The Froude-number for experiment mcp23 (ap. diam.= 10 mm, $t = 60°C$, $h_{melt} = 200\,mm$).

Summary and outlook

We have conducted a set of experiments with a metallic melt of Prandtl-number $Pr = 0.74$ spreading axisymmetrically on a horizontal plate of controlled temperature. With the plate temperature equal to initial melt temperature we, thus, obtain isothermal, purely-liquid spreading.

For plate temperatures below the solidification temperature of the melt non-isothermal spreading occurs in conjunction with the built- up of a basal crust.

Most of the experiments are characterized by a shooting inner flow, a hydraulic jump and a streaming outer spreading flow. This goes along with a jump of the Froude-number from a value $Fr > 1$ towards $Fr < 1$ radially-outward at the position of the hydraulic jump.

In all experiments the volumetric flow rate of melt into the spreading varies in time, in detail a roughly-linear decrease is present during the experimental period.

For isothermal conditions we recover former results of axisymmetric spreading, featuring with increasing radius a circular hydraulic jump and a smooth circular contact line. The hydraulic jump moves inward in time, according to the time behaviour of. The contact line moves outward in time roughly until goes to zero.

For non-isothermal conditions the same features are present. However, firstly, the hydraulic jump radius is generally smaller for cooled plates. Secondly, the progression of the contact line is slower for cooled plates and, thirdly the contact line strongly departs from a circular shape. In detail strong fingering and oscillating spreading is observed for cooled plates.

The conducted experiments clearly demonstrate that basal cooling or/and basal solidification has a pronounced influence on both the hydraulic jump and the progressing contact line. As particularly the hydraulic jump position varies in time both with and basal crust built-up, further experiments with constant should allow to isolate and clarify the effect from basal crust built-up. These experiments should further be able to link the present problem to experiments and theories in literature on the influence of downstream liquid height on the hydraulic jump.

If further significant improvement of the experiment should be obtained by implementing a height profile measuring technique. This, however, requires a resolution of the complete height profile (or at least the height profile of the outer streaming flow) at a reasonable number of time steps. Thus, the estimation of the height profile, as performed in the present work, could be replaced by reliable measurements and a much more detailed comparison with theoretical predictions would be possible.

Bibliography

[1] Engeln-Müllges/Reutter. *Numerik - Algorithmen mit FORTRAN77 - Programmen*

[2] E. Truckenbrodt. *Fluidmechanik Bd.1*

[3] T. Bohr and others. *Hydraulic jumps, flow separation and wave breaking: An experimental study*. PHYSICA B 228, pp. 1–10

List of Figures

Appendix A:

Description of the experiments

Description of experiment No. 1

Base plate temperature :	60	°C
Melt temperature :	61,6	°C
Height of the melt:	300	mm
Aperture diameter :	5	mm
Mass of solidified melt :	5785	g

At the beginning of the experiment, the spreading is nearly axisymmetric. The hydraulic jump is well formed and its shape is circular up to its disappearance. In the second half of the experiment, the spreading becomes directional. This may be caused by a not exactly horizontal adjustment of the base plate. The final shape of the solidified melt is not an ideal circle. The bottom side has a nearly mirrorfinished surface, only around the impact area some enclosed bubbles are to see. A pattern of flow can be seen on the surface (cf. fig. A1.4).

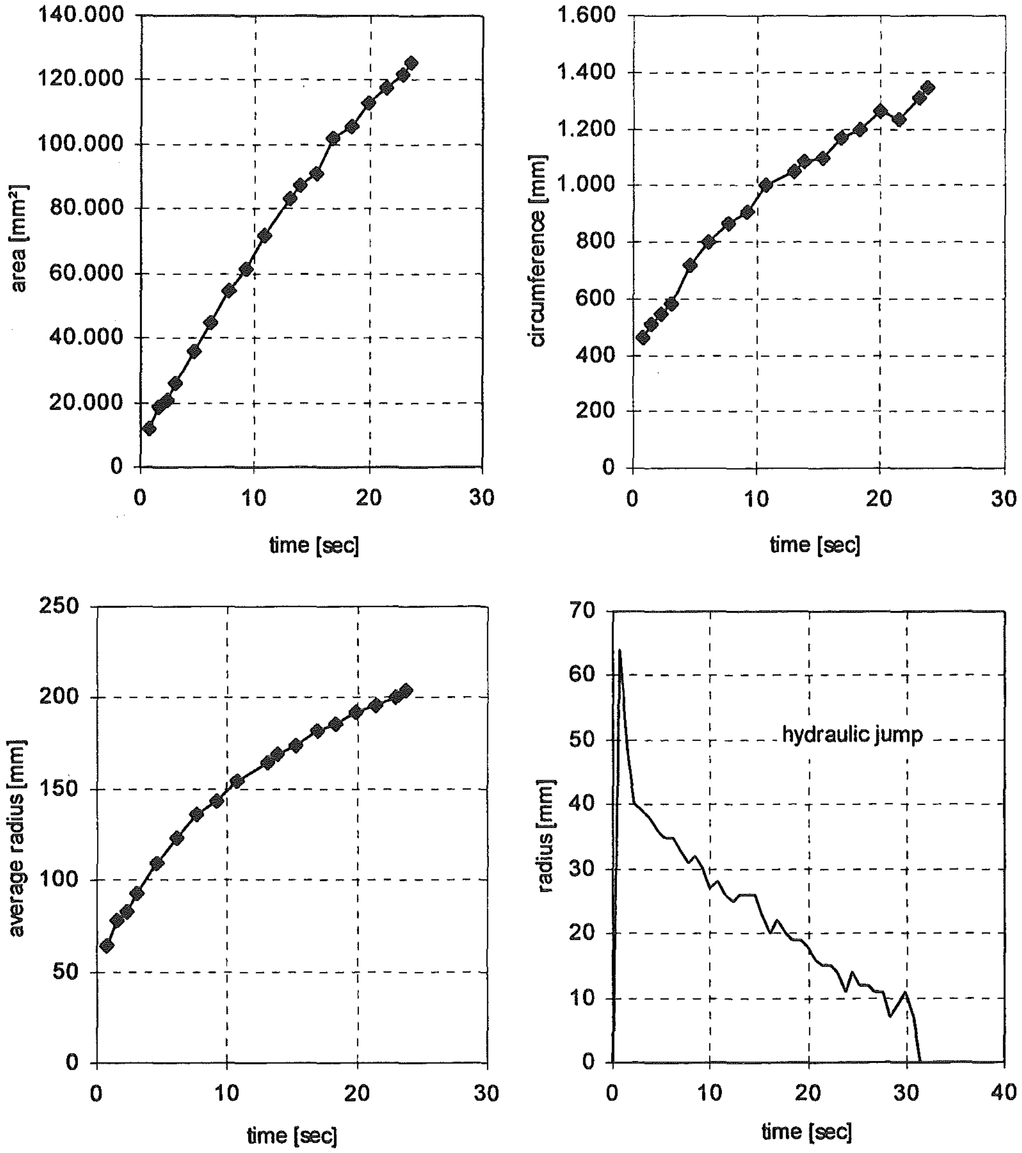

Fig. A1.1: Size of area, radius, circumference and hydraulic jump in time.

The thickness of the solidified melt is nearly constant. A final area of 137000 mm² and a mass of 5785 g leads to an average thickness of 4.57 mm.

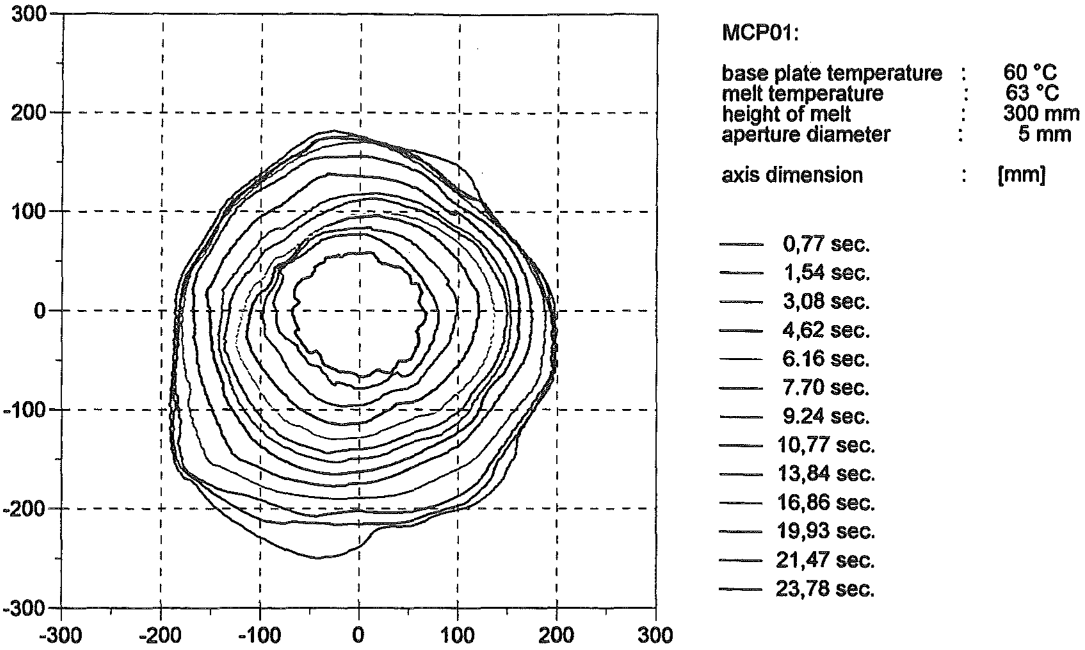

Fig. A1.2: Diagramm of the single phases of spreading. The final curve is not displayed because the recorded area is smaller than the spreading area. The values of the final area, radius and circumference are determined with fig A1.3.

Fig A1.3 Top view of the solidified melt.

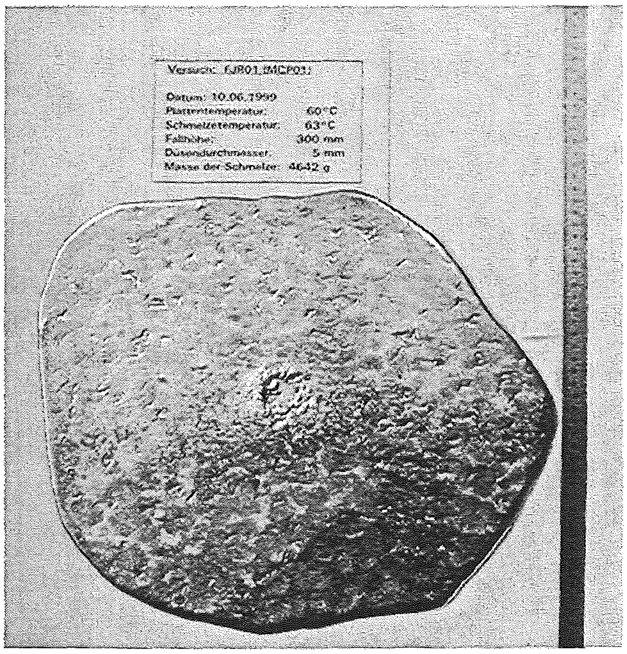

Fig A1.4 Bottom view of the solidified melt.

Experiment mcp01 : Temperatures [°C]

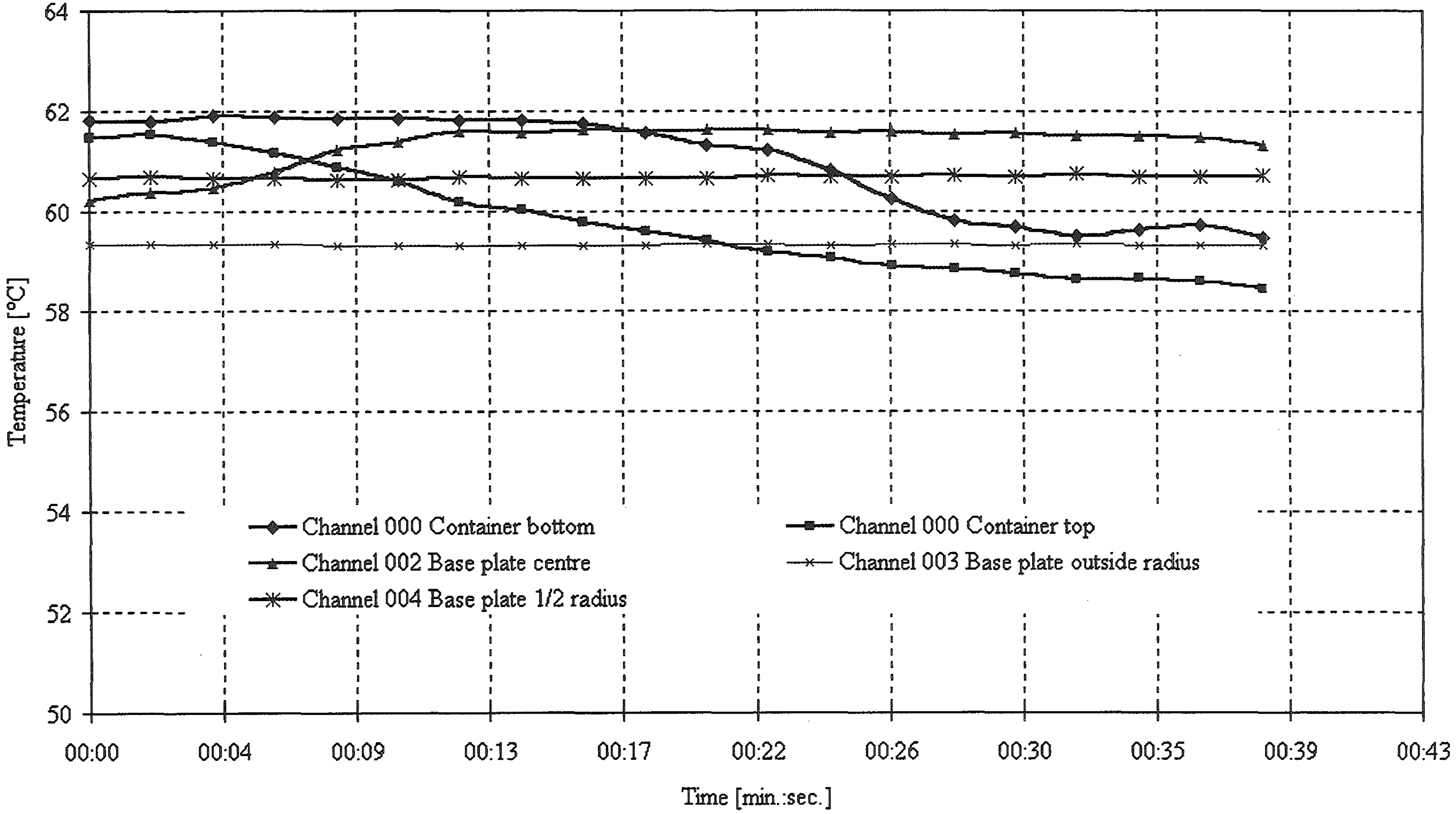

Description of experiment No. 2

Base plate temperature :	60	°C
Melt temperature :	61,8	°C
Height of melt :	300	mm
Aperture diameter :	2	mm
Mass of solidified melt :	4993	g

This experiment is characterized by a rather slow spreading of the melt. The spreading progresses in some preferred directions. The reason for that is the higher sensitivity of the spreading process for a non-horizontal adjustment of the base plate (the max. reachable accuracy is 0.1 $^{mm}/_{m}$). This effect is strongest for the 2 mm aperture. The hydraulic jump appeares only in the first second of the experiment. After its collapse, an active zone with higher flow rates and bubble forming is seen around the impact area. It remains constant nearly all the time. The final form of the solidified metal is elliptic. The surface of the bottom side is mirrorfinished and only a few enclosed bubbles in the center are to see.

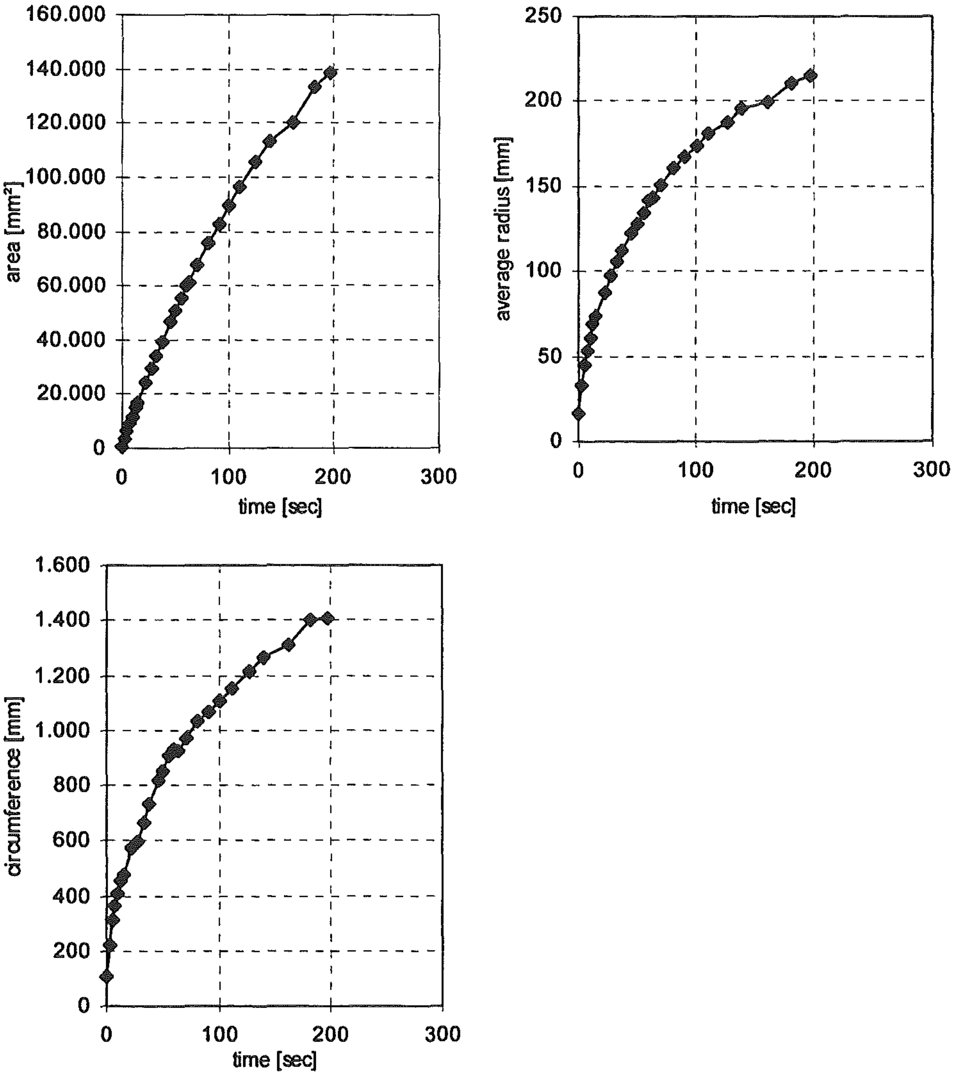

Fig. A2.1: Size of area, radius and circumference in time.

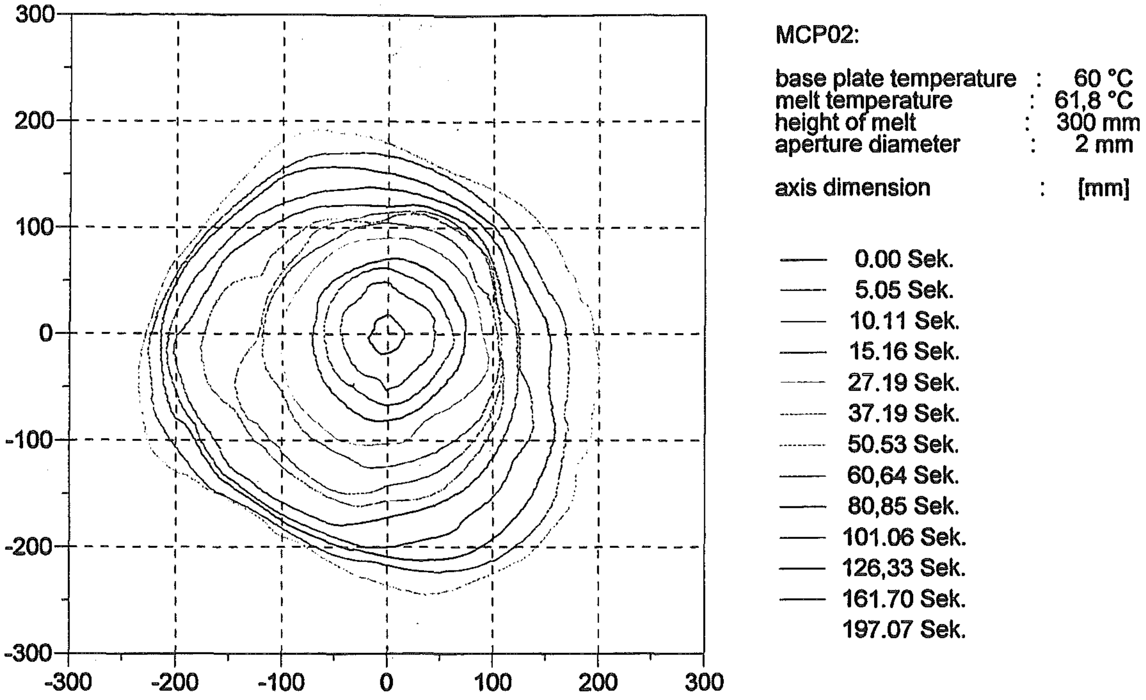

Fig A2.2: Diagramm of the single phases of the spreading.

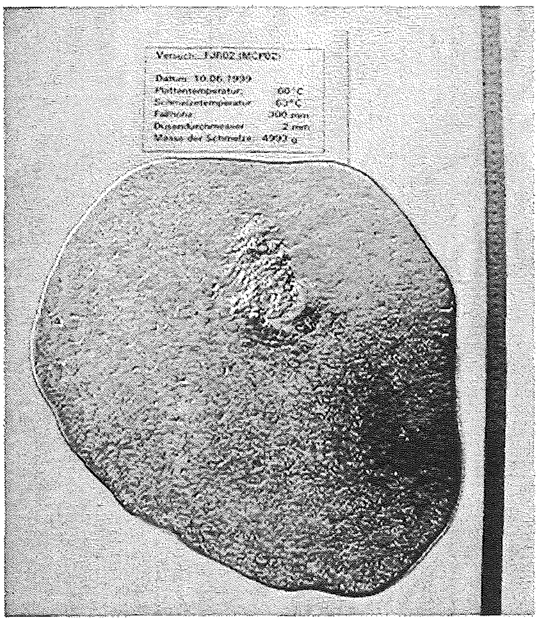

Fig A2.3 Top view of the solidified melt.

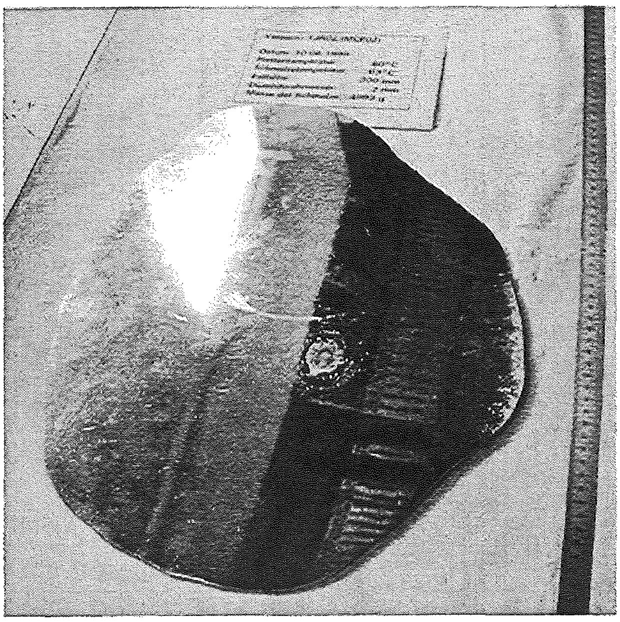

Fig A2.4 Bottom view of the solidified melt.

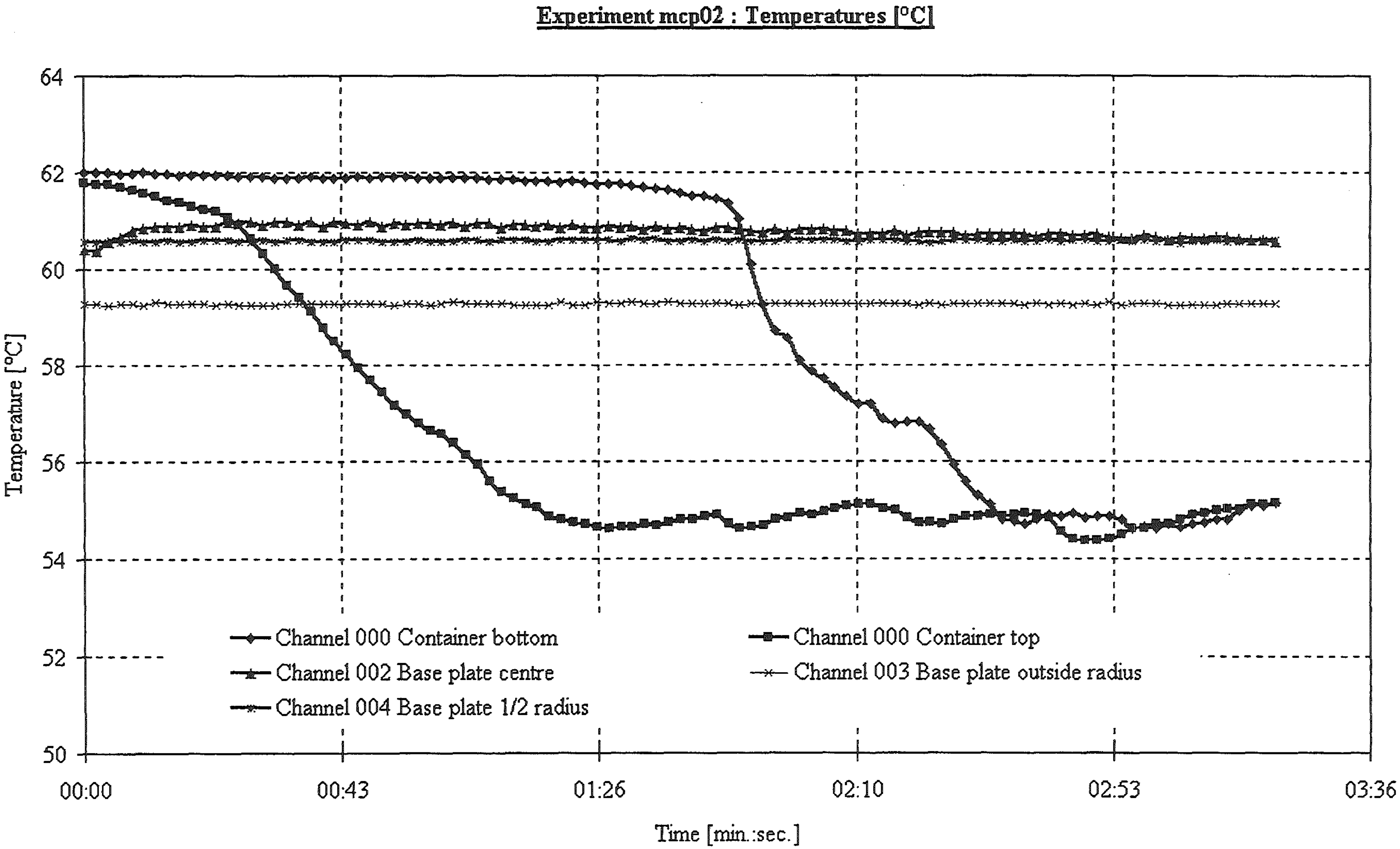
Experiment mcp02 : Temperatures [°C]
Temperature [°C]
64
62
60
58
56
54
52
50
Time [min.:sec.]
00:00
00:43
01:26
02:10
02:53
03:36
Channel 000 Container bottom
Channel 000 Container top
Channel 002 Base plate centre
Channel 003 Base plate outside radius
Channel 004 Base plate 1/2 radius

Description of experiment No. 4

Base plate temperature : 60 °C
Melt temperature : 61,8 °C
Height of the melt : 400 mm
Aperture diameter : 5 mm
Mass of solidified melt : 5428 g

The different height of the melt above the base plate compared to experiment no.1 leads to a higher impact energy of the liquid jet. This circumstance has no remarkable effect to the spreading and the behaviour of the hydraulic jump. The spread of the melt is axissymmetric up to the end of the experiment.

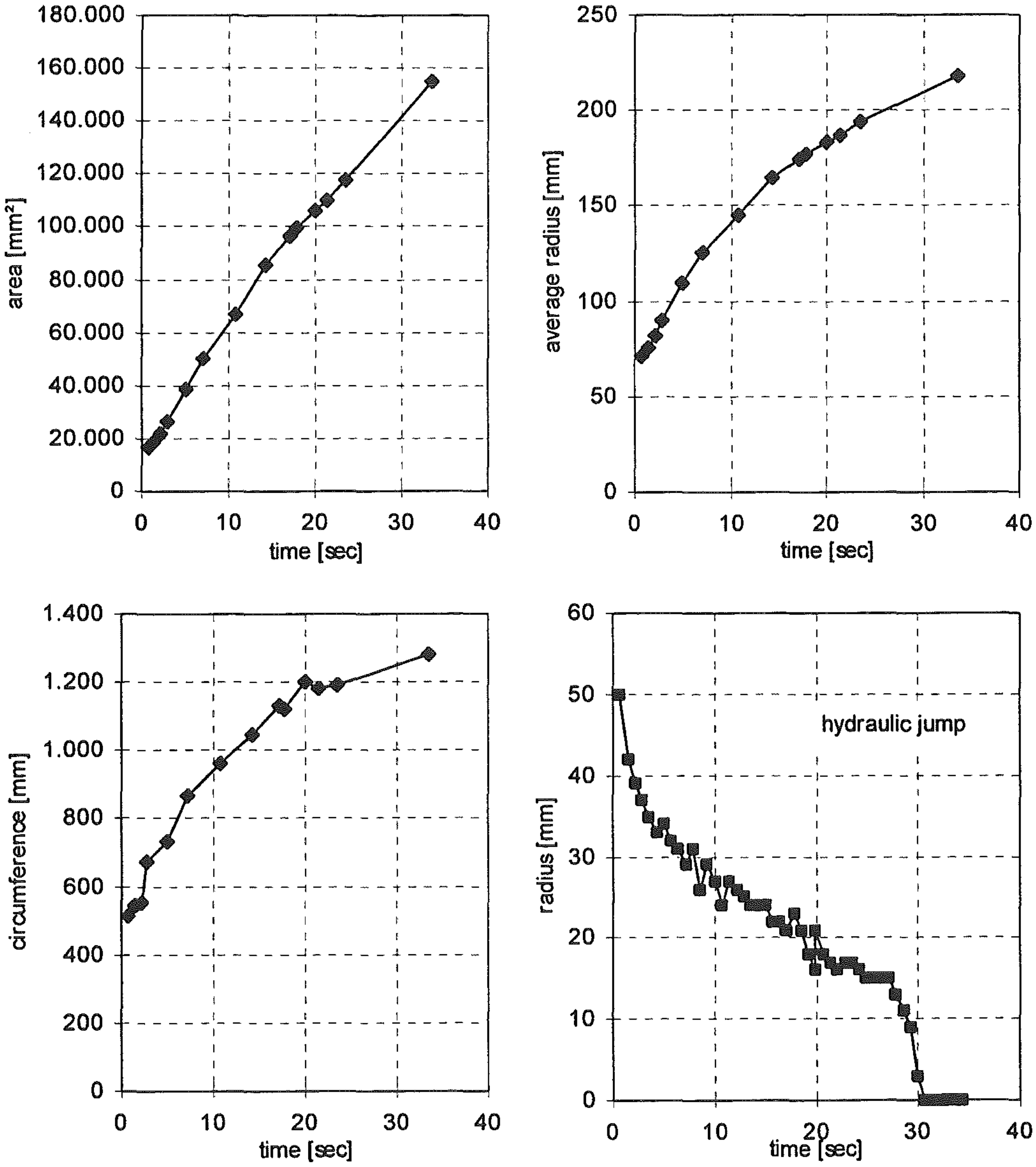

Fig. A4.1: Size of area, radius, circumference and hydraulic jump in time.

The thickness of the solidified melt is nearly constant. With an final area of 154800 mm² and a mass of 5428 g we receive an average thickness of 3,83 mm.

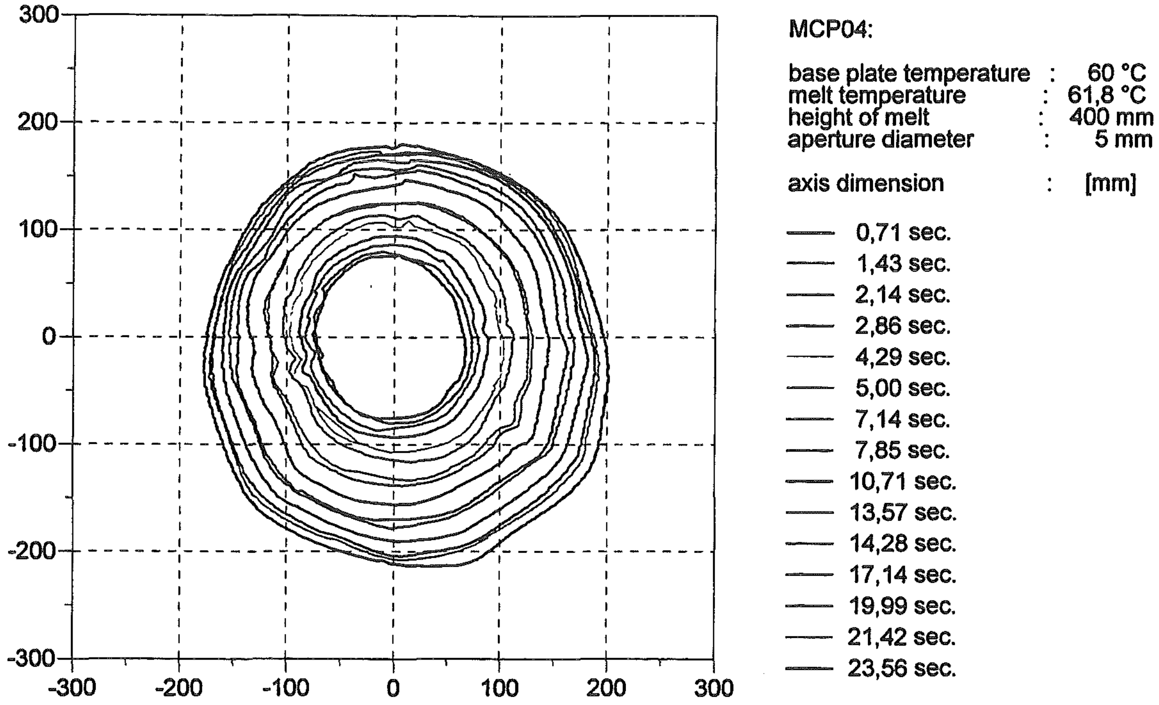

Fig. A4.2: Diagramm of the single phases of spreading. The final curve is not displayed because the recorded area is smaller than the spreading area. The values of the final area, radius and circumference are determined with fig. A4.3.

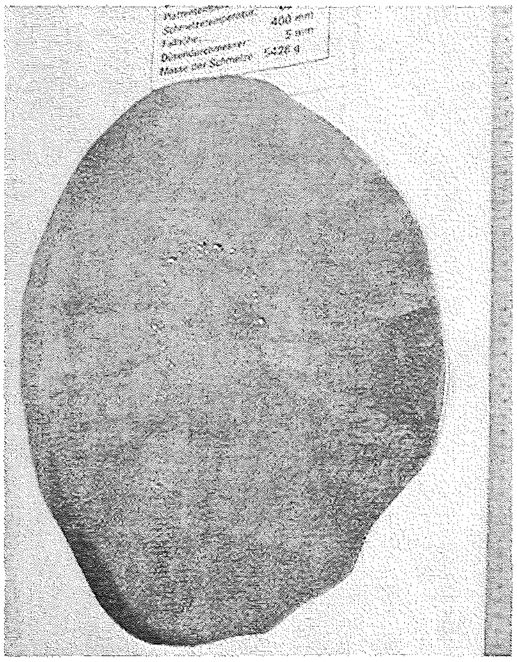

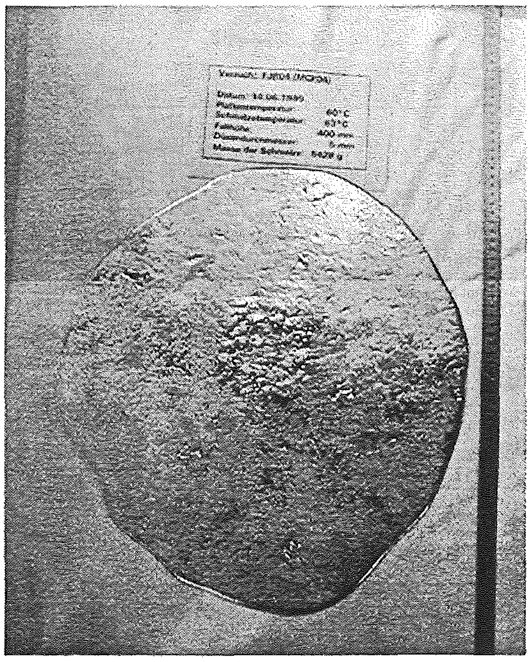

Fig. A4.3: Top view of the solidified melt. Fig. A4.4: Bottom view of the solidified melt.

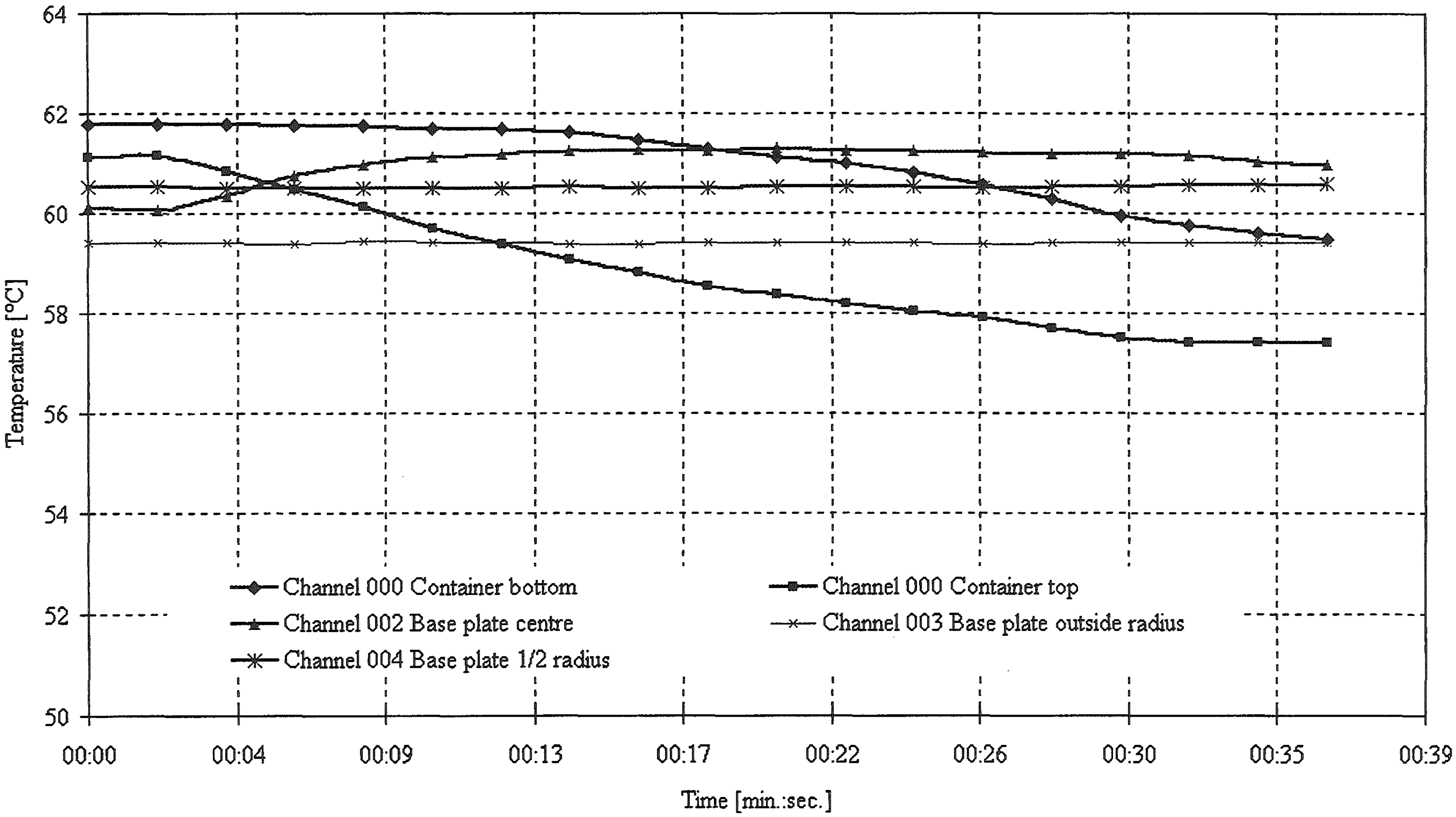

Experiment mcp04 : Temperatures [°C]

Description of experiment No. 5

Base plate temperature : 60 °C
Melt temperature : 61,4 °C
Height of the melt : 400 mm
Aperture diameter : 2 mm
Mass of solidified melt : 4952 g

In contrast to the experiment with the 5 mm aperture, the increased height of the melt seems to has no influence on the spreading. There is no hydraulic jump formed, as seen in the other experiments with the 2 mm aperture. The spreading becomes more and more oscillating with progressing time. First, the flow direction seems to follow the circumference, then the time interval between two spreading pulses increases to several (approx. 8-10) seconds.

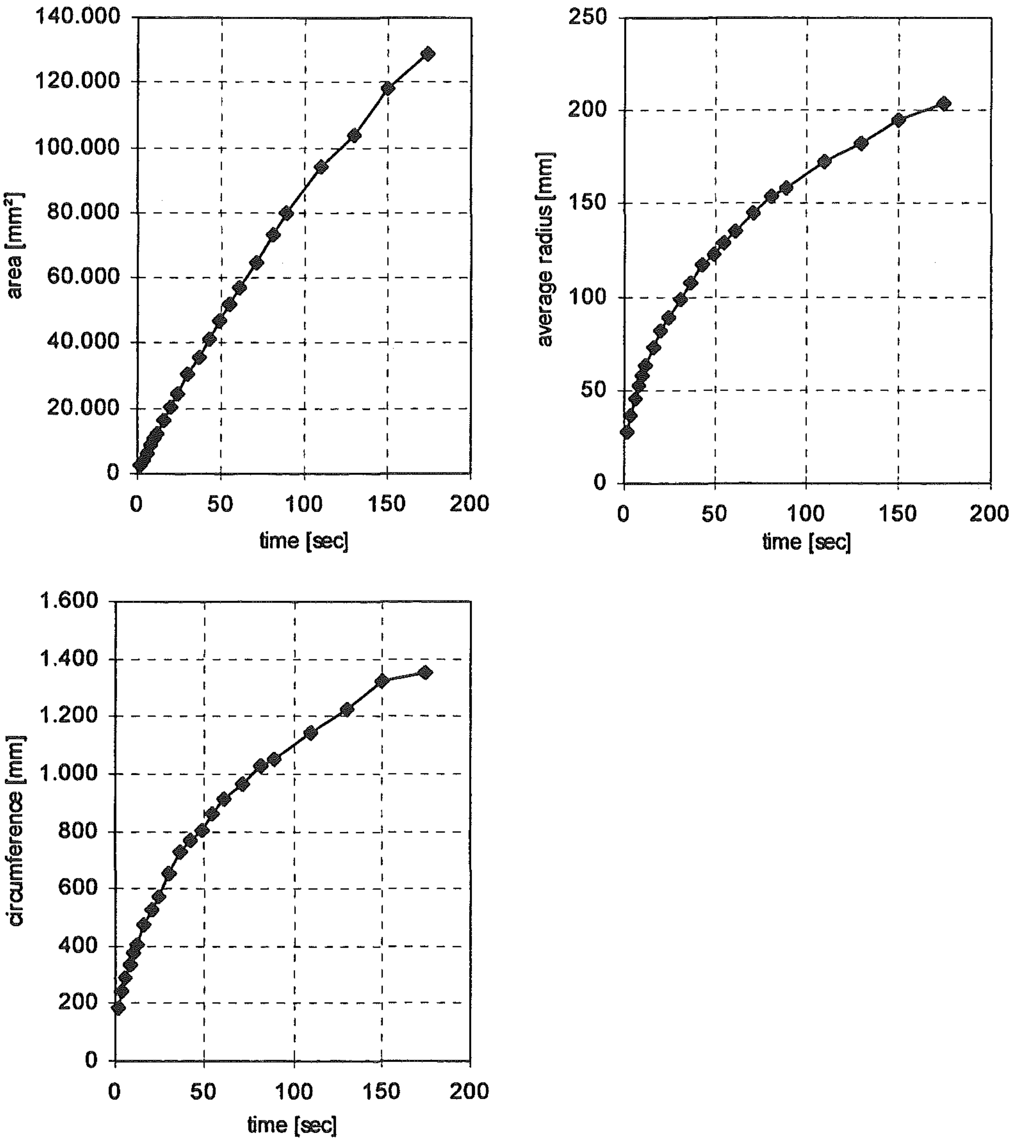

Fig. A5.1: Size of area, radius and circumference in time.

The thickness of the solidified melt is nearly constant. With an final area of 128636 mm² and a mass of 4952 g we receive an average thickness of 4.17 mm.

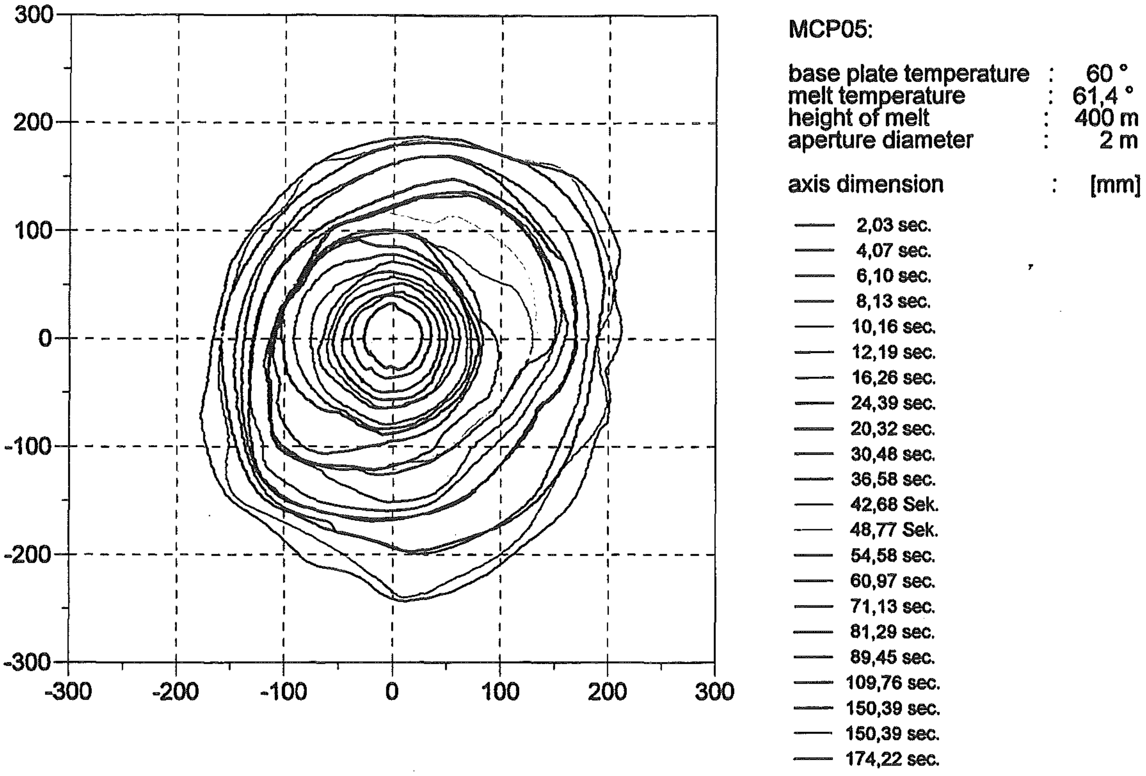

Fig. A5.2: Diagramm of the single phases of spreading.

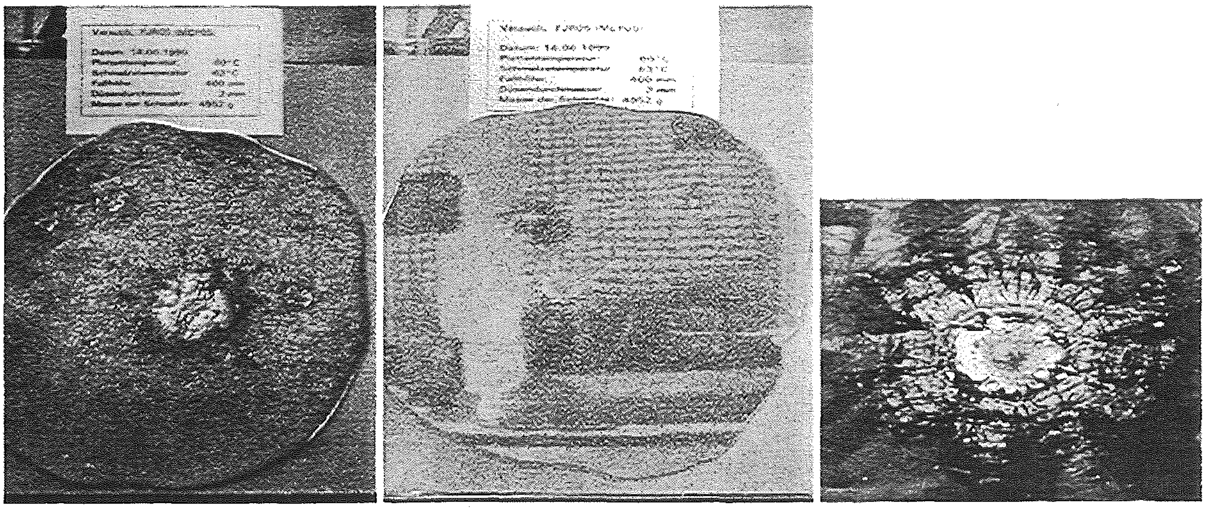

Fig. A5.3: Top view (left), bottom view (middle) and details of the impact area on the bottom view (right) of the solidified melt.

Experiment mcp05 : Temperatures [°C]

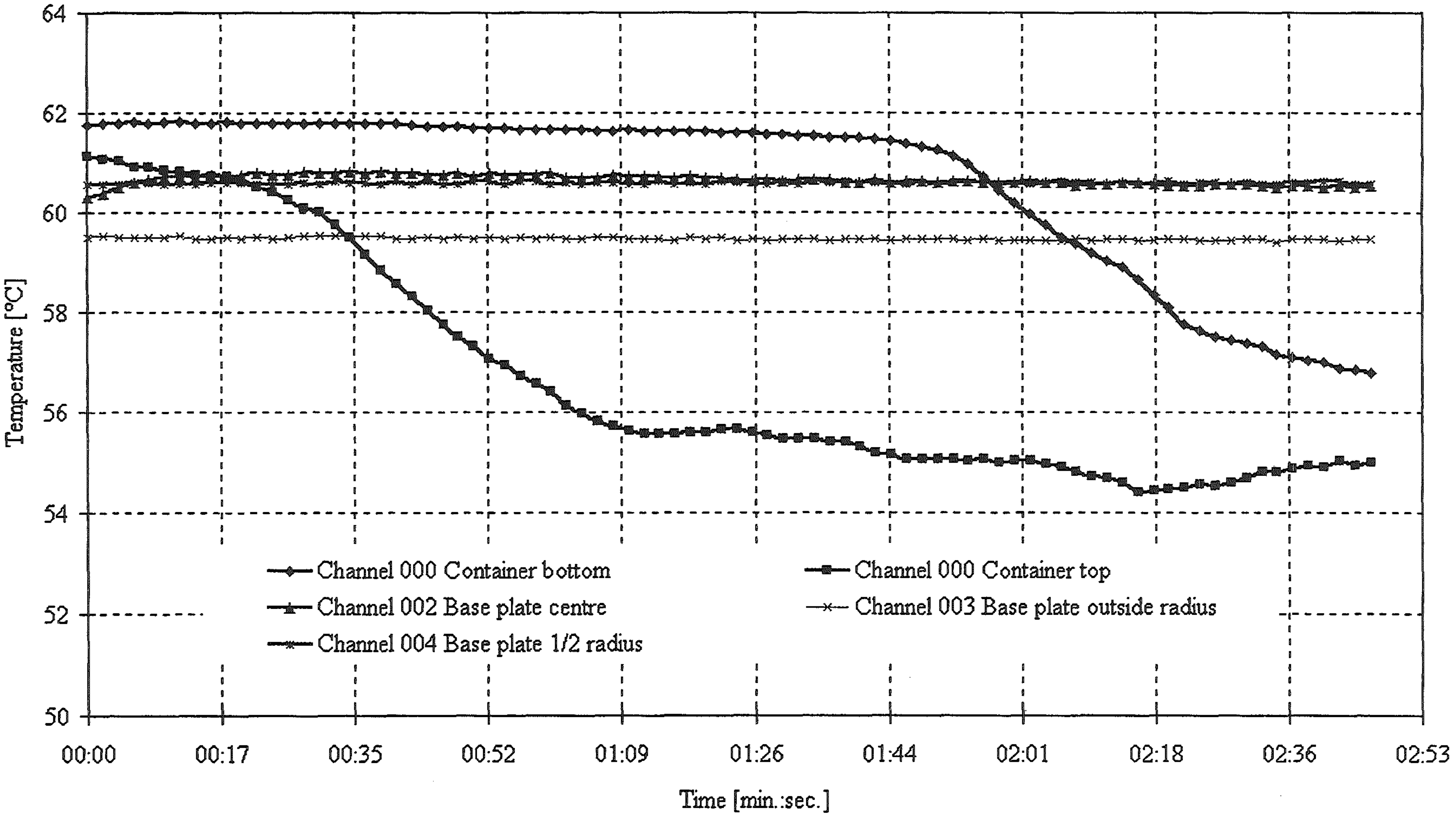

Description of experiment No. 7

Base plate temperature : 40 °C
Melt temperature : 61,35 °C
Height of the melt : 200 mm
Aperture diameter : 10 mm
Mass of solidified melt : 4911 g

This is the first experiment using the 10 mm aperture. At the beginning, there is only an area of shooting flow to see and it takes nearly one second to form a hydraulic jump. The size of the hydraulic jump radius is quite large, more than twice as much in diameter as for the 5mm aperture. The form of the area of the shooting flow is circular only in the last 2 seconds of the experiment. The rest of the time its form changes from elliptic to angular. Finally, the solidified melt has a nearly triangular form. Its thickness is quite large, compared to the past non-isothermal experiments.

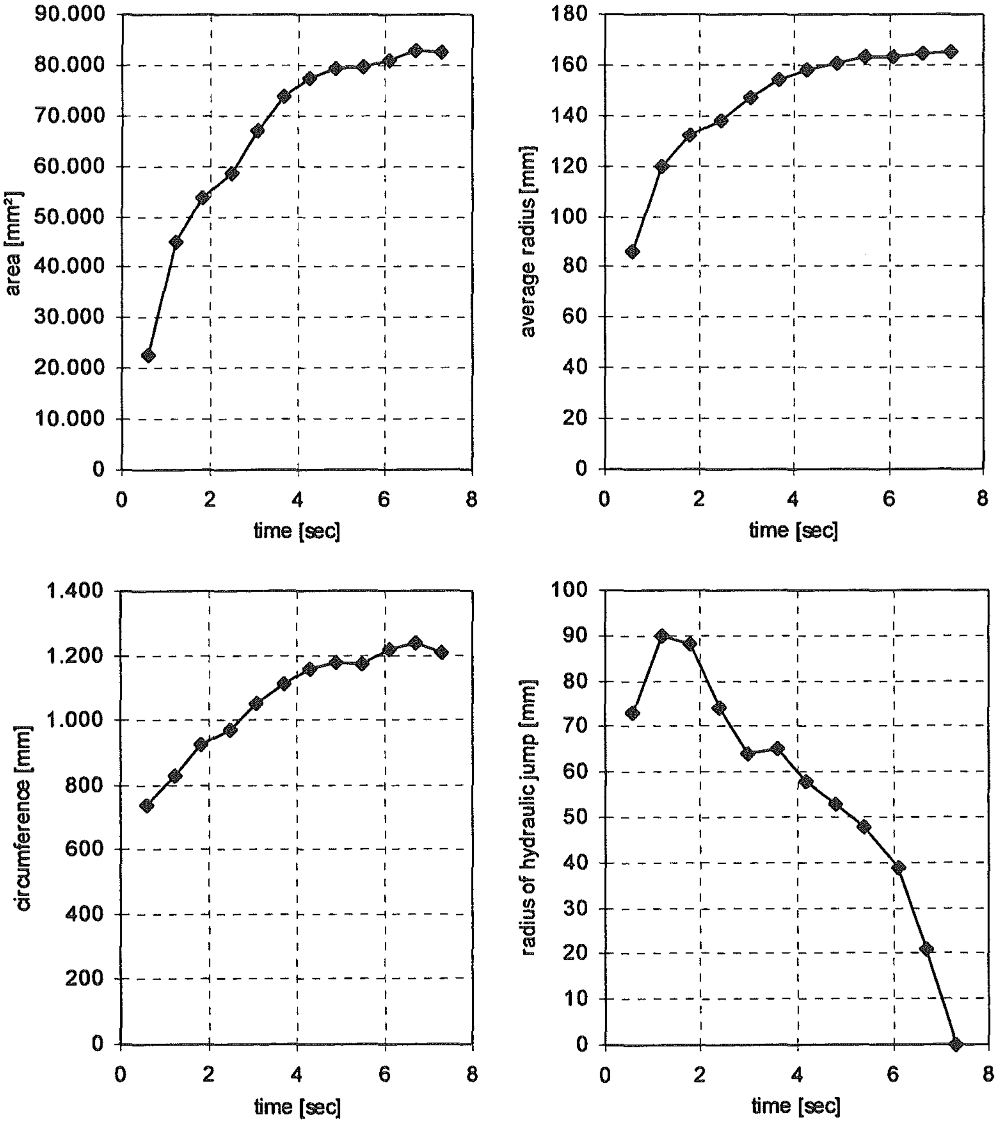

Fig. A7.1: Size of area, radius, circumference and hydraulic jump in time.

The thickness of the solidified melt is nearly constant. With a final area of 82522 mm² and a mass of 4911 g, we receive an average thickness of 6.45 mm.

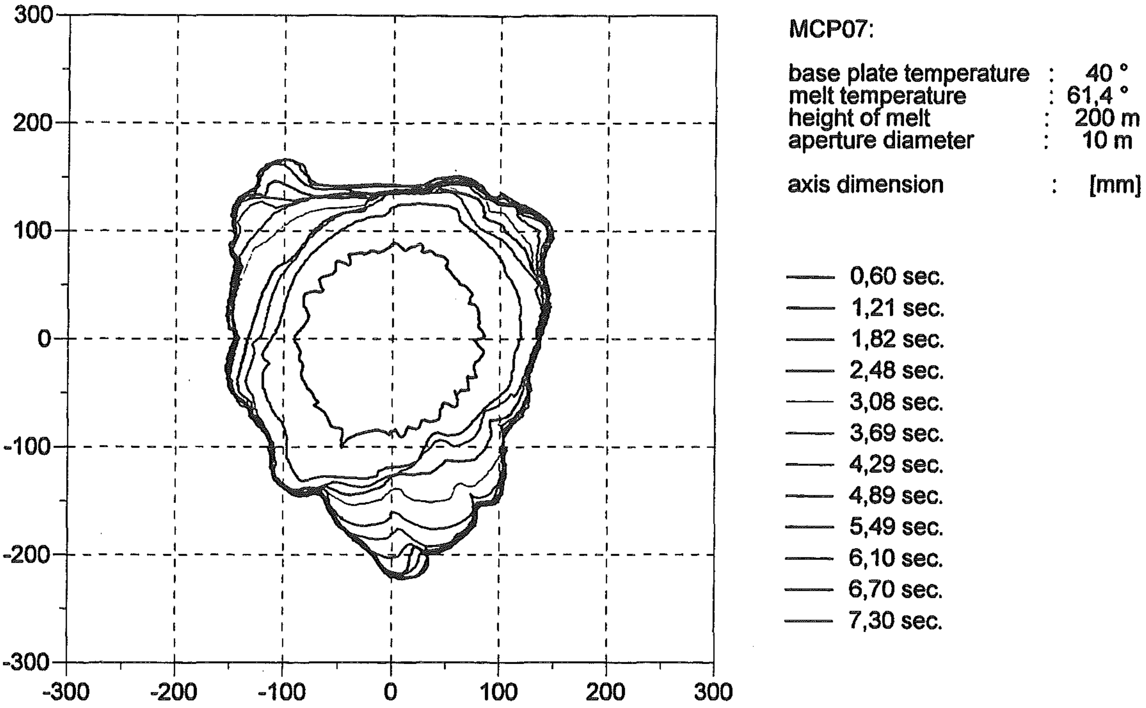

Fig. A7.2: Diagramm of the single phases of spreading.

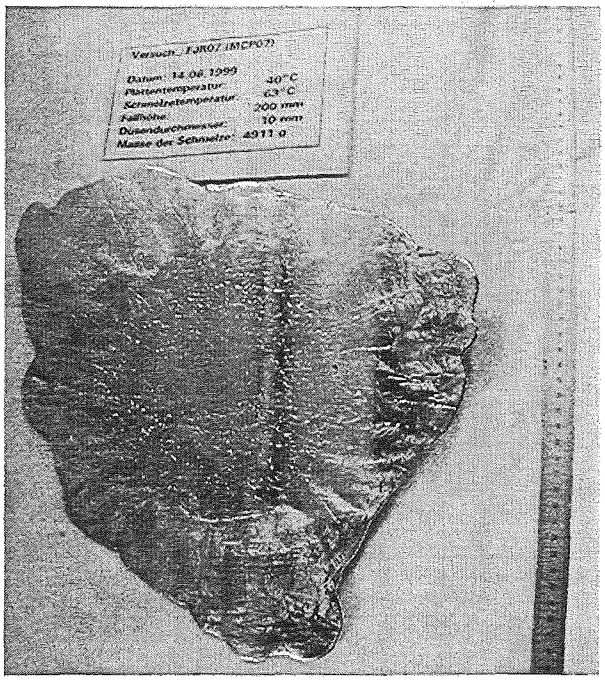

Fig. A7.3: Top view of the solidified melt.

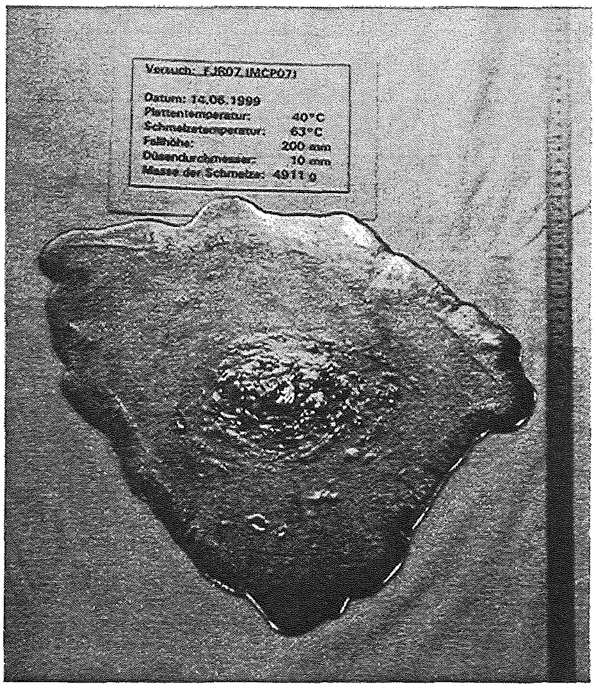

Fig. A7.4: Bottom view of the solidified melt.

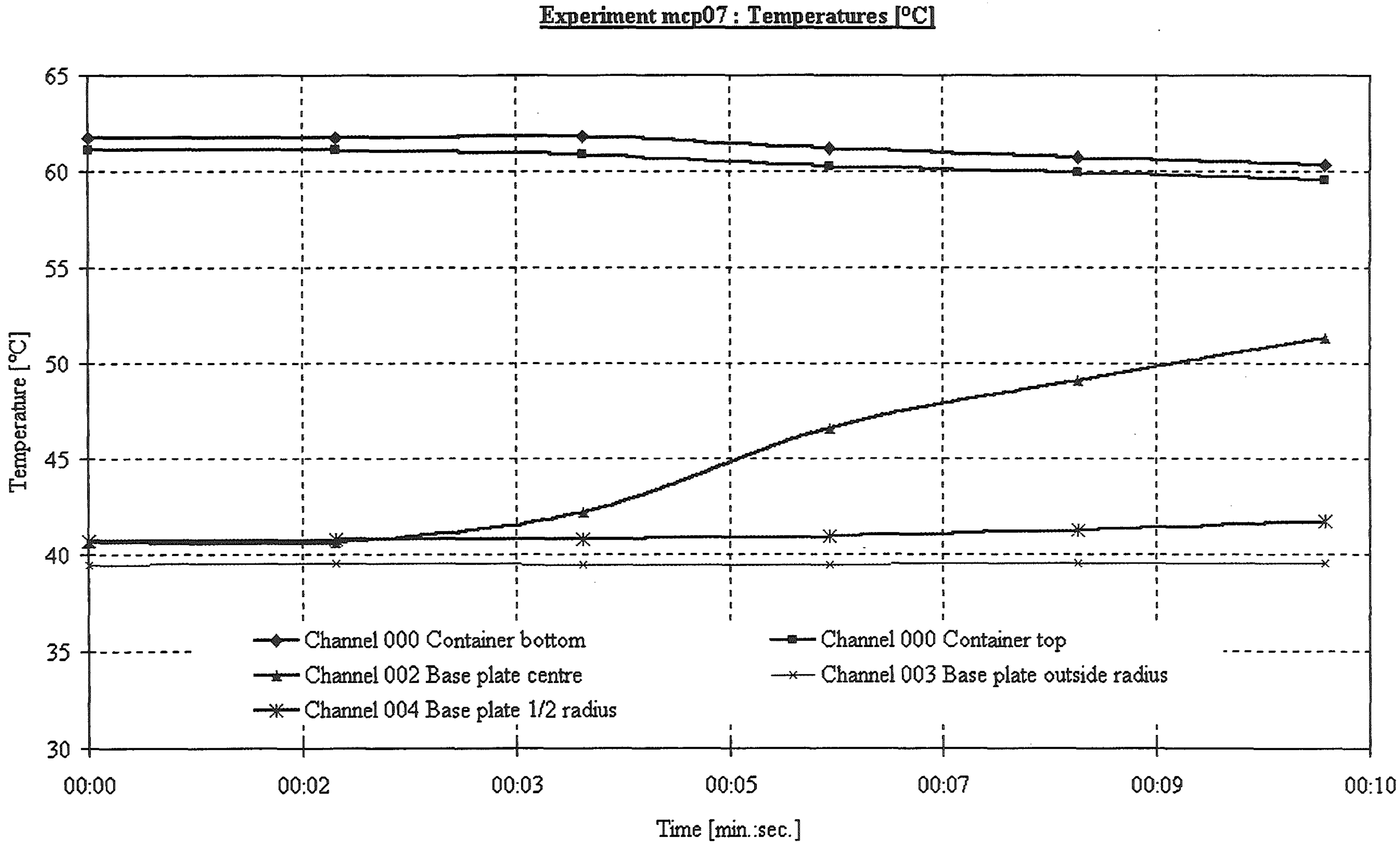
Experiment mcp07 : Temperatures [°C]
65
60
55
50
45
40
35
30
Temperature [°C]
00:00
00:02
00:03
00:05
00:07
00:09
00:10
Time [min.:sec.]
Channel 000 Container bottom
Channel 000 Container top
Channel 002 Base plate centre
Channel 003 Base plate outside radius
Channel 004 Base plate 1/2 radius

Description of experiment No. 8

Base plate temperature :	20	°C
Melt Temperature :	61,6	°C
Height of the melt :	400	mm
Aperture diameter :	5	mm
Mass of solidified melt :	5026	g

This is the first non-isothermal experiment using the 5 mm aperture. In contrast to the isothermal experiments, the spreading is quite asymmetric from starting. The impact area is soon covered with small solidified melt pieces. These pieces lead to a redirection of the liquid jet. Some fountains of molten metal appear and they cause a melt transport directly to the outer regions of the base plate. The sudden solidification of these melt pieces block the spreading of the melt. In the remaining flow directions, the melt fronts fingers out strongly. Some of the fingers disappear by the continuous flow of melt. We can also see that there are several layers of melt, at least three at the end of the experiment. The final solidified shape of the melt is irregular and less axisymmetric.

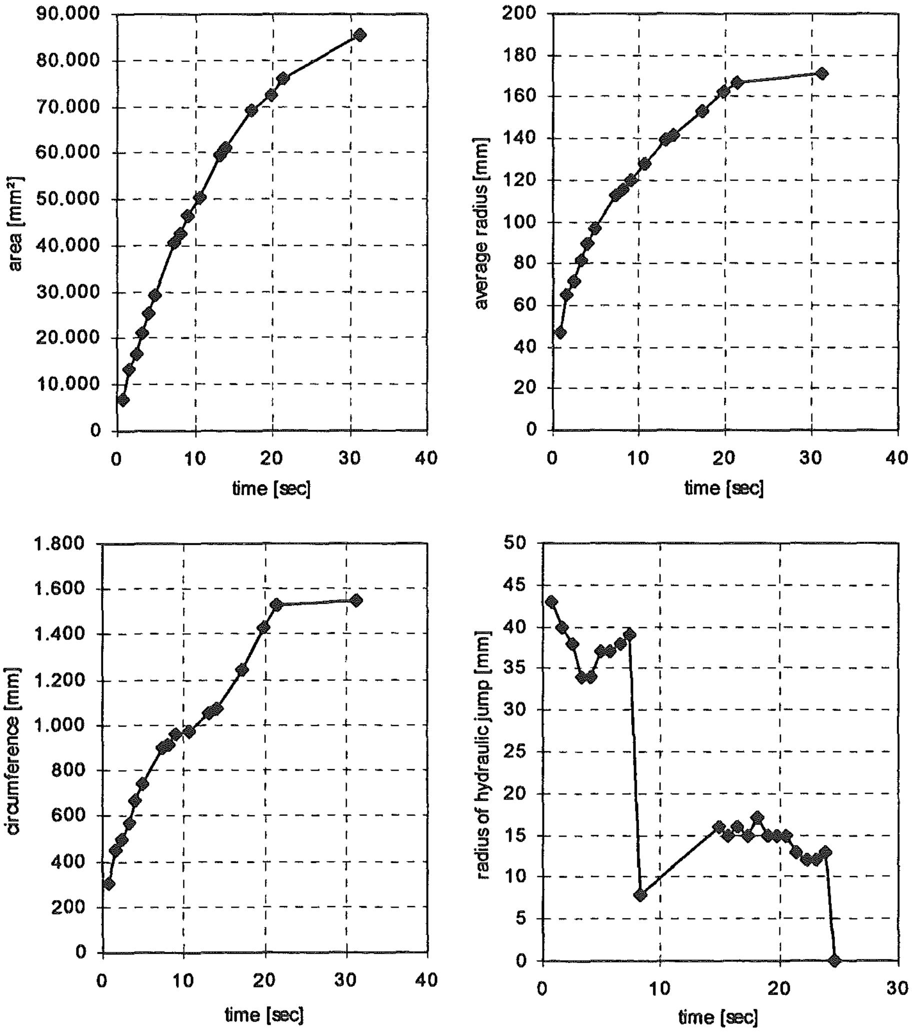

Fig A8.1: Size of area, radius, circumference and hydraulic jump in time.

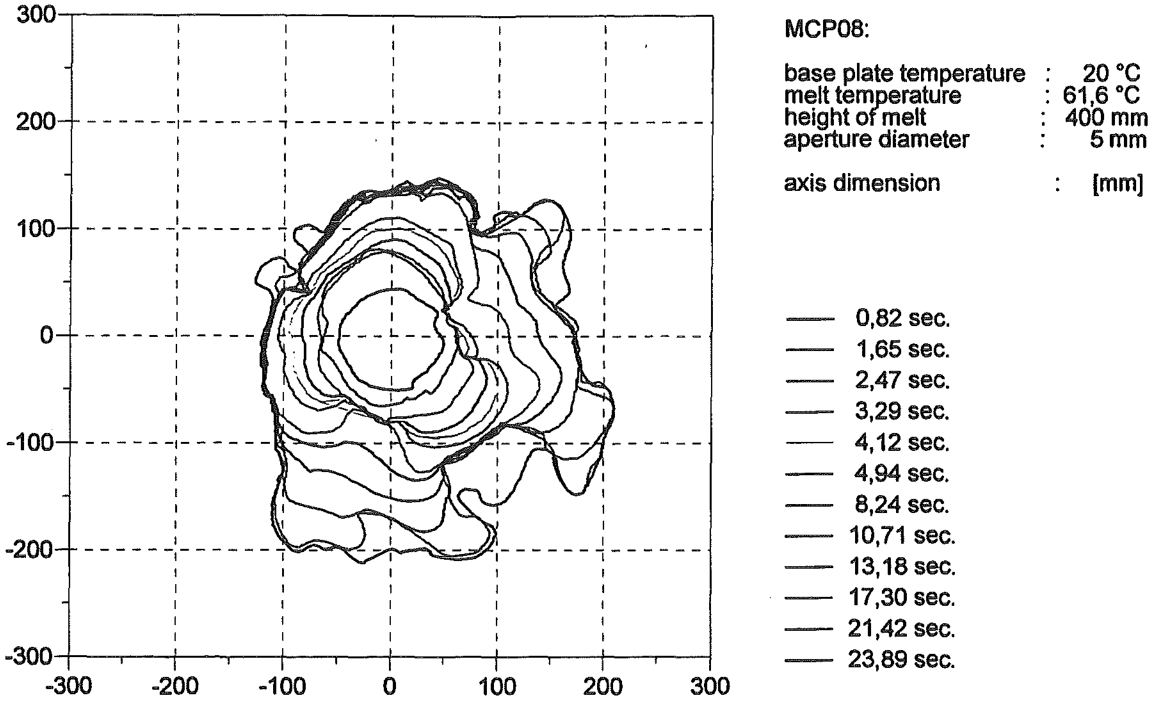

MCP08:

base plate temperature : 20 °C
melt temperature : 61,6 °C
height of melt : 400 mm
aperture diameter : 5 mm

axis dimension : [mm]

Fig A8.2: Diagramm of the single phases of spreading.

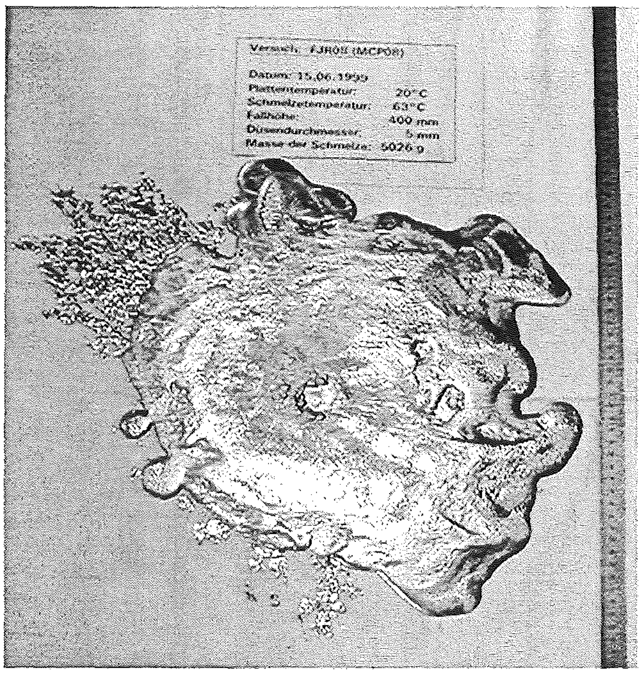

Fig. A8.3: Top view of the solidified melt.

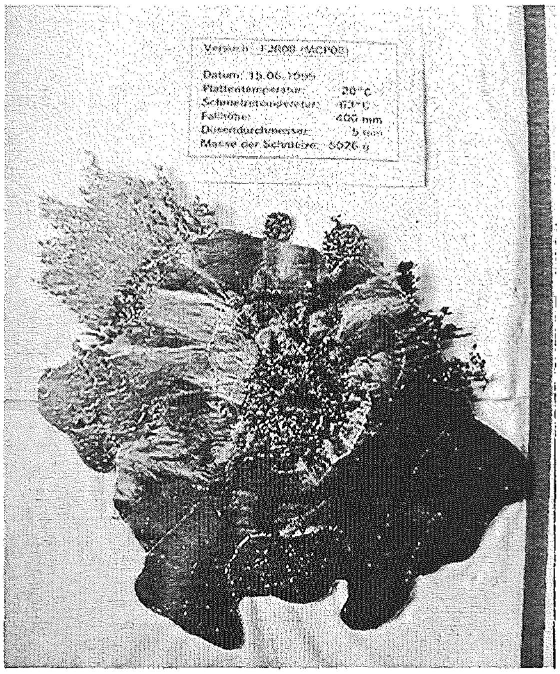

Fig. A8.4: Bottom view of the solidified melt.

Experiment mcp08 : Temperatures [°C]

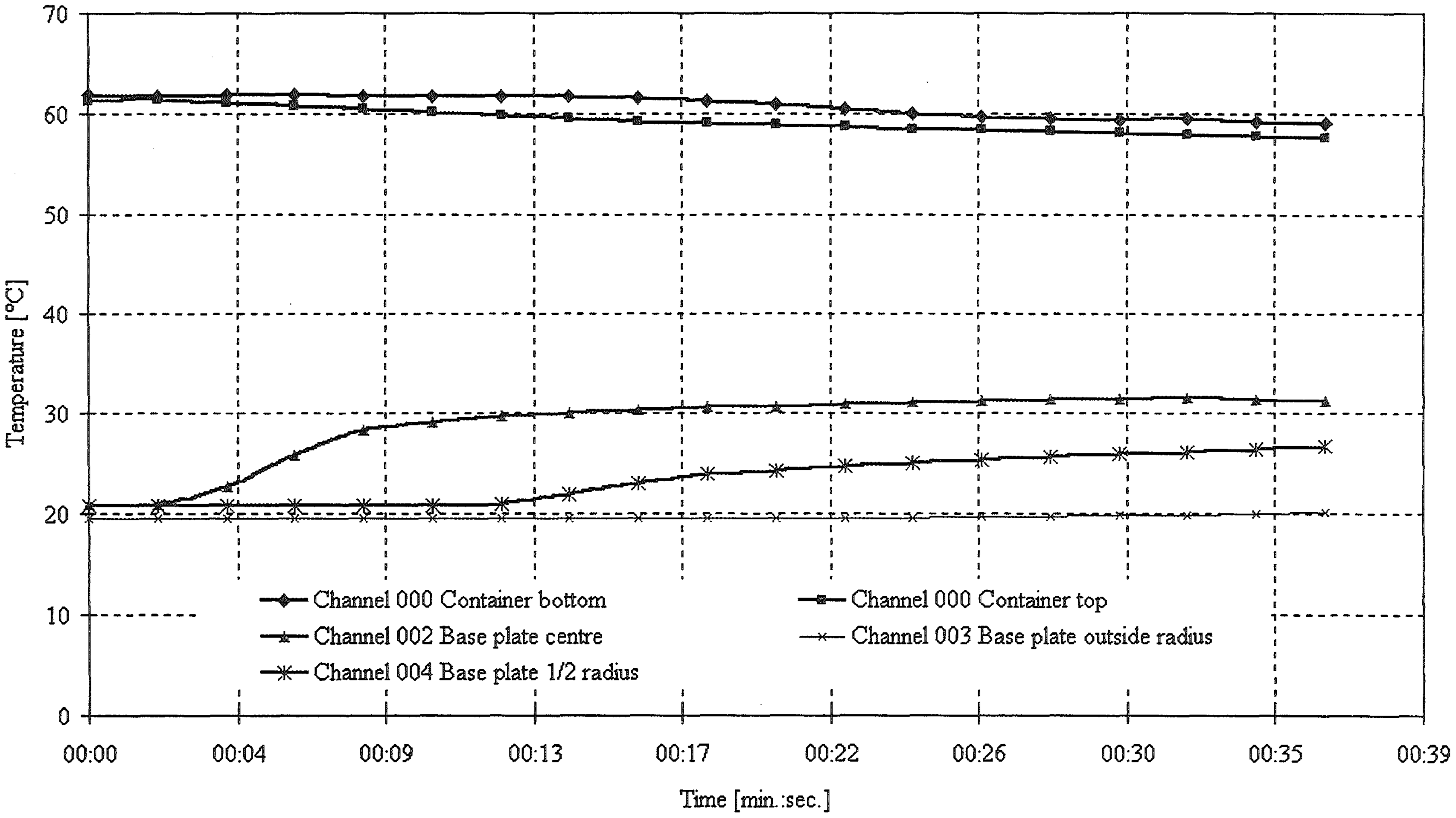

Description of experiment No. 9

Base plate temperature :	20	°C
Melt temperature :	61,35	°C
Height of the melt :	400	mm
Aperture diameter :	2	mm
Mass of solidified melt :	4774	g

As in experiment no. 8, we have a melt transport away from the central area. Here, too, the solidificating particles prevent the undisturbed flow of melt. Because of the low volumetric flow rate, the melt begins to solidify already near the impact area. A layering of melt is the result and the spreading is not axisymmetric. The solidified melt body consists of at least five distinguishable layers. A hydraulic jump is only seen in the first two seconds.

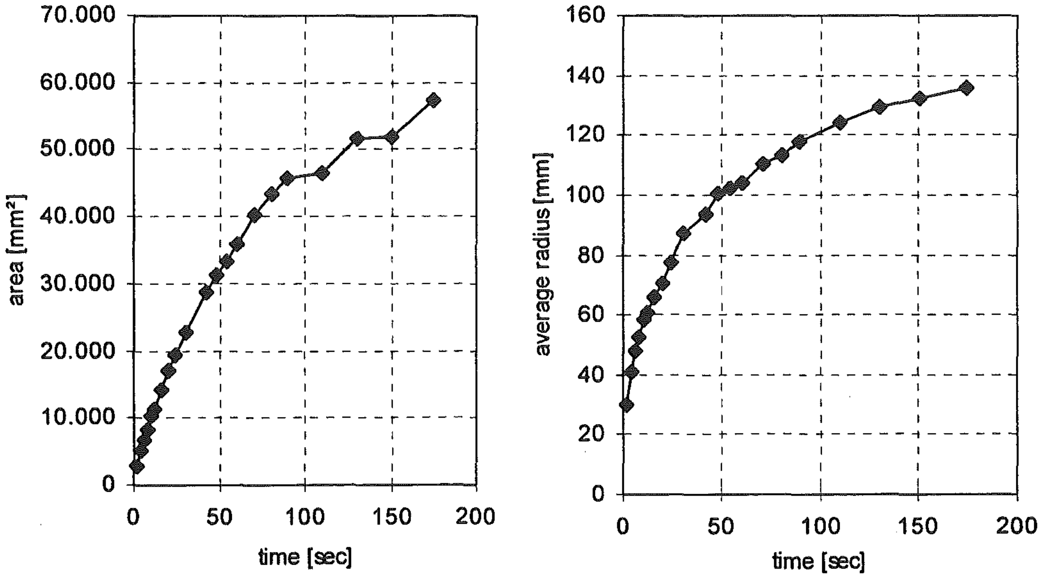

The average thickness of the solidified melt is approx. 9 mm overall. One should recover that the central area is much thicker than the outer region.

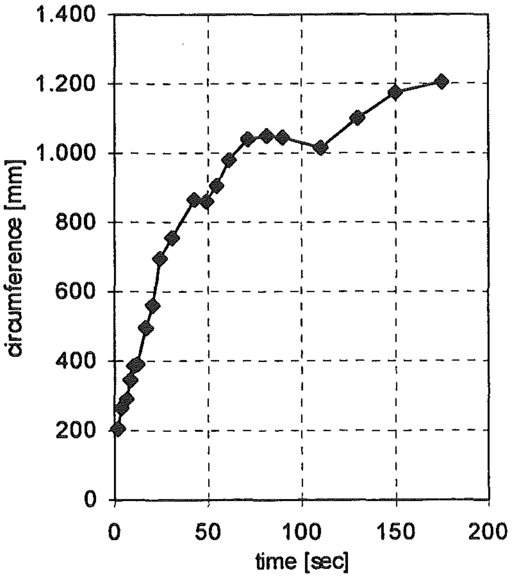

Fig. A9.1: Size of area, radius and circumference in time.

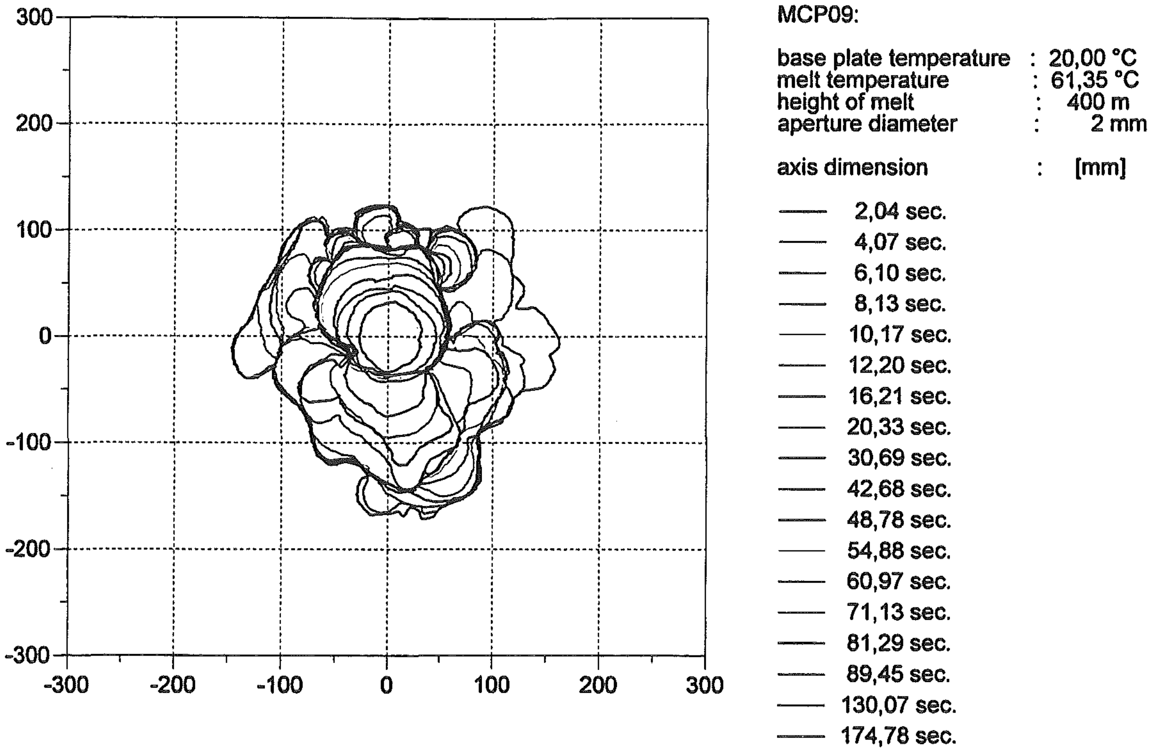

MCP09:

base plate temperature : 20,00 °C
melt temperature : 61,35 °C
height of melt : 400 m
aperture diameter : 2 mm

axis dimension : [mm]

Fig. A9.2: The single phases of spreading.

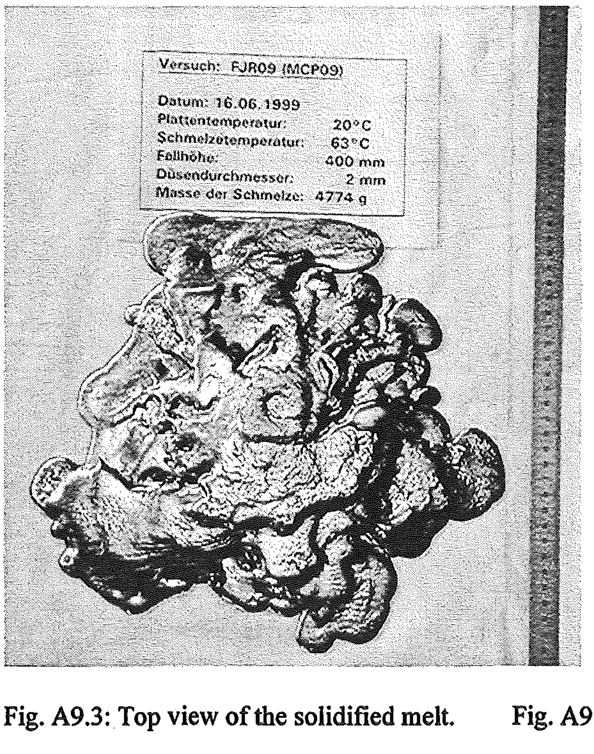

Versuch: FJR09 (MCP09)

Datum: 16.06.1999
Plattentemperatur: 20°C
Schmelzetemperatur: 63°C
Fallhöhe: 400 mm
Düsendurchmesser: 2 mm
Masse der Schmelze: 4774 g

Fig. A9.3: Top view of the solidified melt.

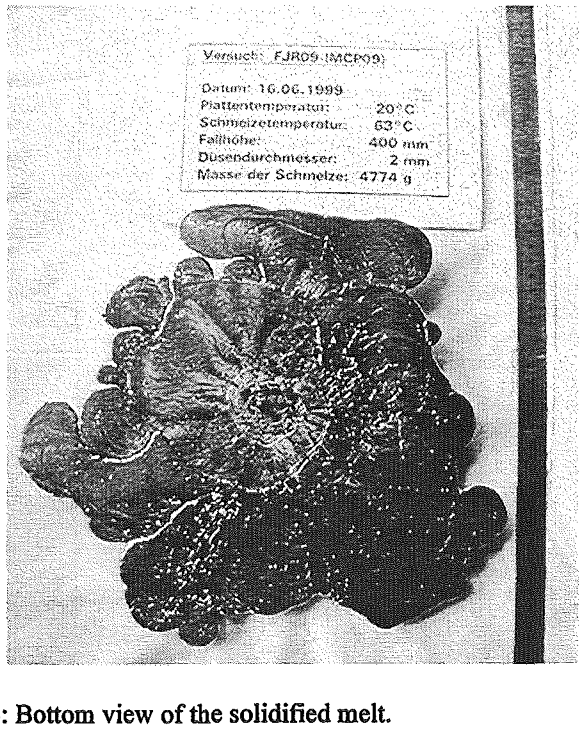

Versuch: FJR09 (MCP09)

Datum: 16.06.1999
Plattentemperatur: 20°C
Schmelzetemperatur: 63°C
Fallhöhe: 400 mm
Düsendurchmesser: 2 mm
Masse der Schmelze: 4774 g

Fig. A9.4: Bottom view of the solidified melt.

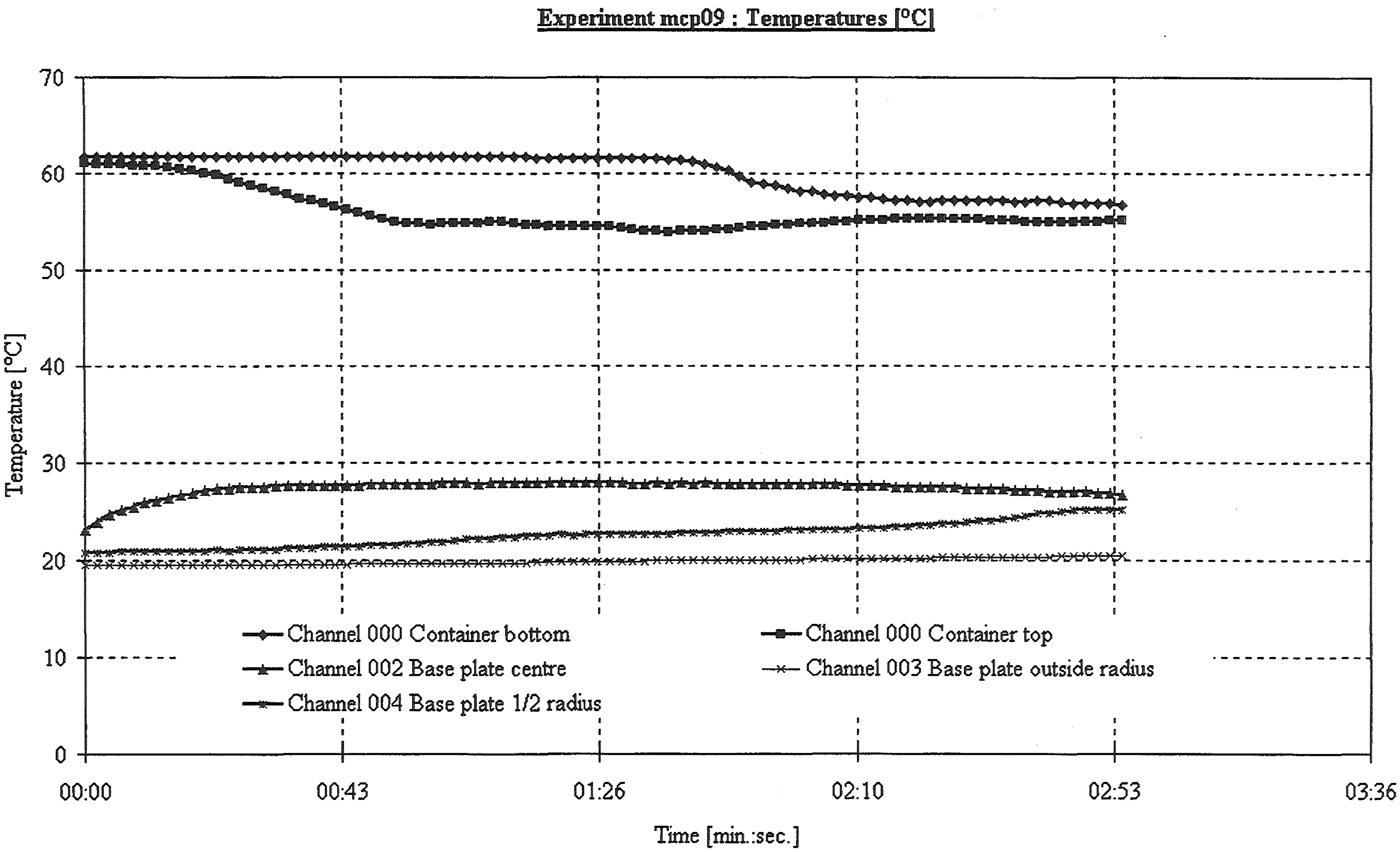
Experiment mcp09 : Temperatures [°C]
Temperature [°C]
70
60
50
40
30
20
10
0
00:00
00:43
01:26
02:10
02:53
03:36
Time [min.:sec.]
Channel 000 Container bottom
Channel 000 Container top
Channel 002 Base plate centre
Channel 003 Base plate outside radius
Channel 004 Base plate 1/2 radius

Description of experiment No. 10 and 17

	mcp 10		mcp17	
Base plate temperature :	4	°C	4	°C
Melt Temperature :	61,3	°C	61,7	°C
Height of the melt :	300	mm	300	mm
Aperture diameter :	5	mm	5	mm
Mass of solidified melt :	4697	g	5428	g

This experiment is executed twice, firstly under normal conditions, secondly with a thermally insulated impact area like described in experiment no.16. Without an insulated impact area, one can see the same effects as in experiment no. 8. As expected, the small plastic plate prevents the solidification of melt parts in the impact area. A quite regular hydraulic jump is formed and its radius size decreases slowly. In both experiments, we have solidification of melt inside the area of the shooting flow. It seems that two different hydraulic jumps appears. These two narrow annular regions can be seperated clearly. The two photos below show this effect. On fig. A10.1, one can see the hydraulic jump (white arrows) of experiment MCP10 without insulation (left image), furthermore there are the small solidified parts throwed out of the center to see. The right image in fig. A10.1, the same effect is shown for experiment MCP17 with insulation. The dark zone around the impact jet marks the 'inner hydraulic jump'. The outside hydraulic jump disappears after 6 – 7 seconds (cf. fig. A10.2), resulting in a fast decreasing of the radius of the hydraulic jump. The right picture is taken 1.5 seconds after the jet impinges the plate, the left one is taken 6.15 seconds after impignition.

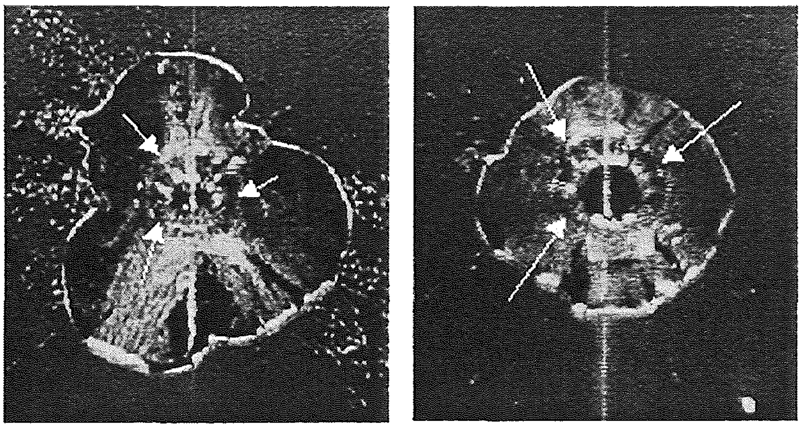

Fig. A10.1: Double appearance of a hydraulic jump.

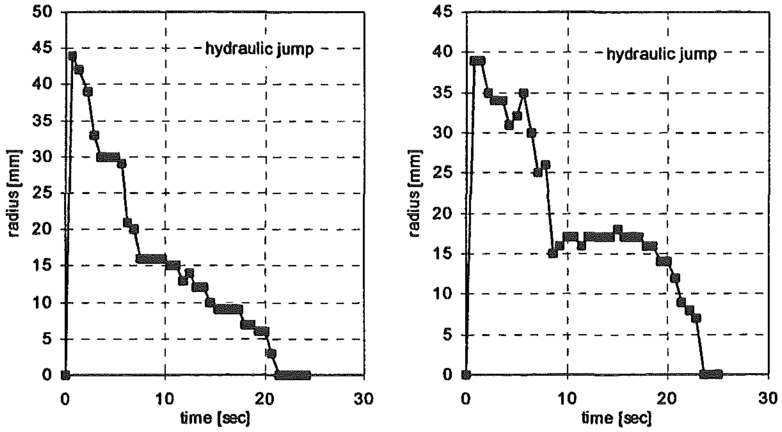

Fig. A10.2 : Size of the hydraulic jump radius in time (left mcp17, right mcp10).

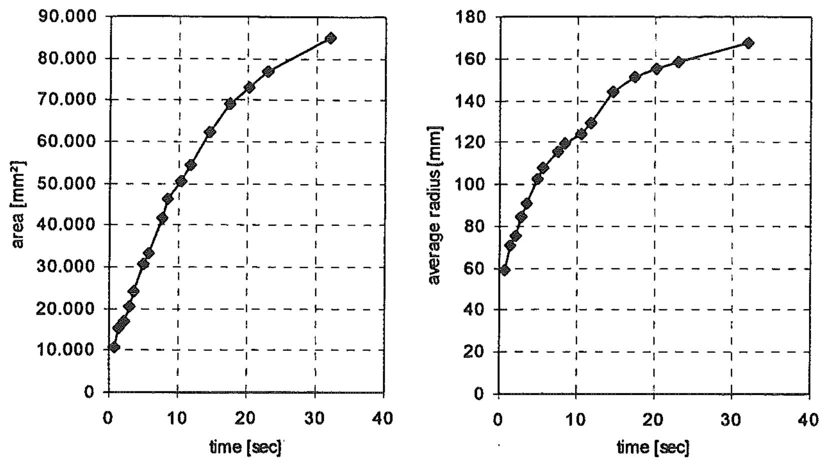

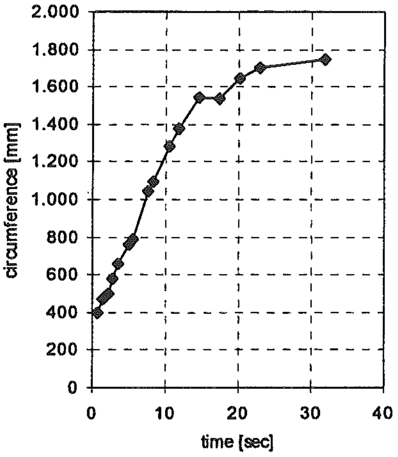

The values for experiment MCP10 differ not much from these of MCP17. The final size of the solidified melt is approx. 87.000 mm².

Fig. A10.3: Size of area, circumference and average radius for experiment MCP17.

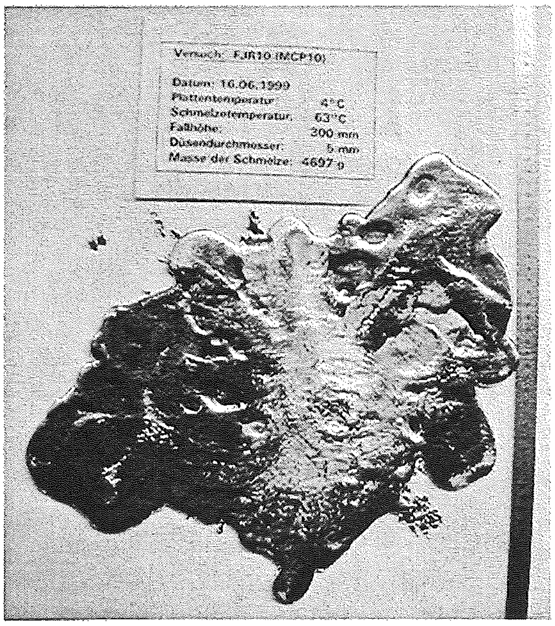

Fig. A10.4 : Top view of the solidified melt for experiment mcp17.

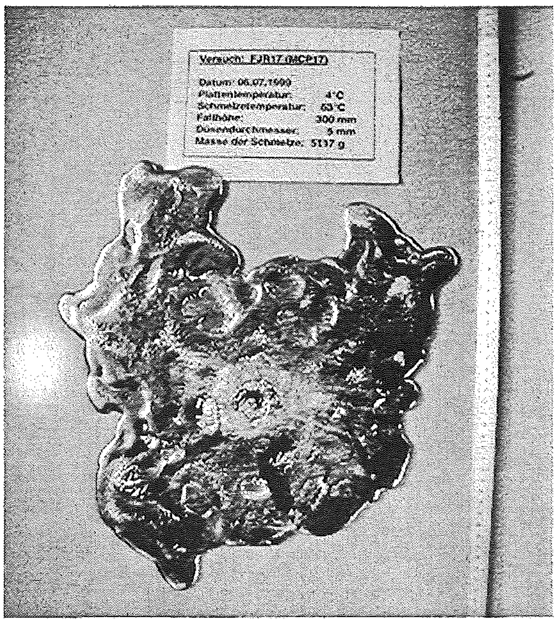

Fig. A10.5 : Top view of the solidified melt for experiment mcp10.

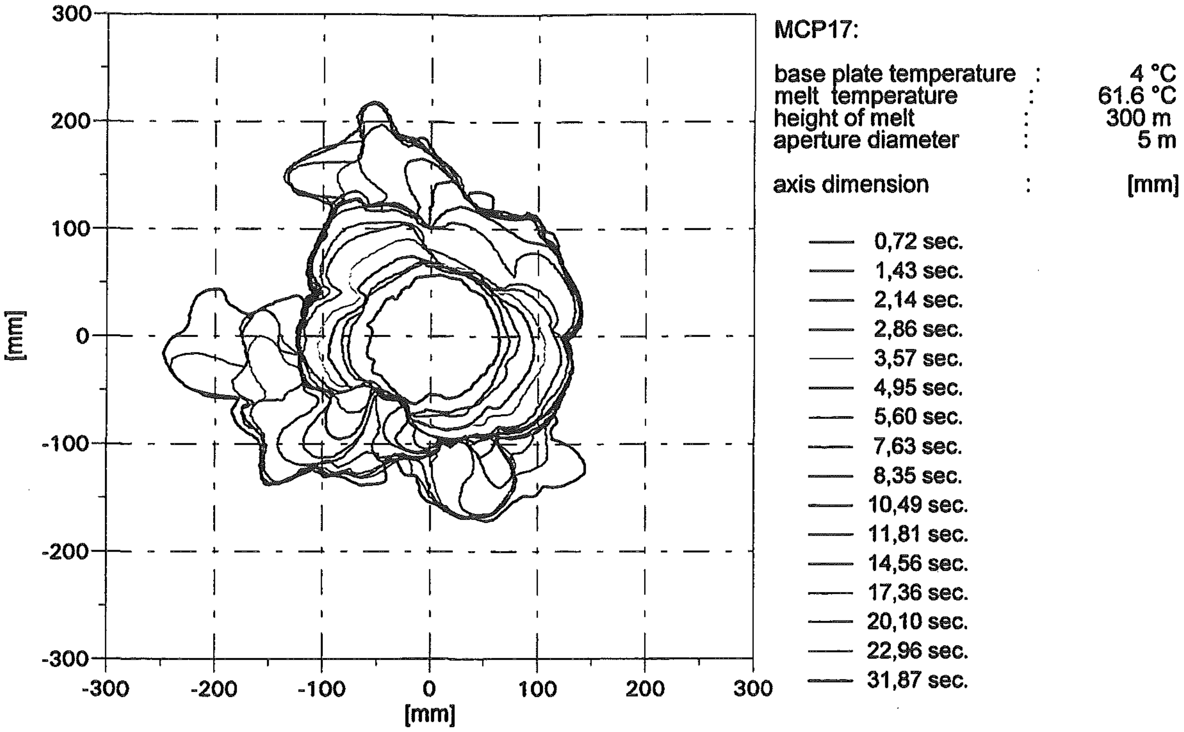
MCP17:

base plate temperature	:	4 °C
melt temperature	:	61.6 °C
height of melt	:	300 m
aperture diameter	:	5 m
axis dimension	:	[mm]

Fig. A10.6: Single phases of spreading for experiment MCP17.

Experiment mcp10 : Temperatures [°C]

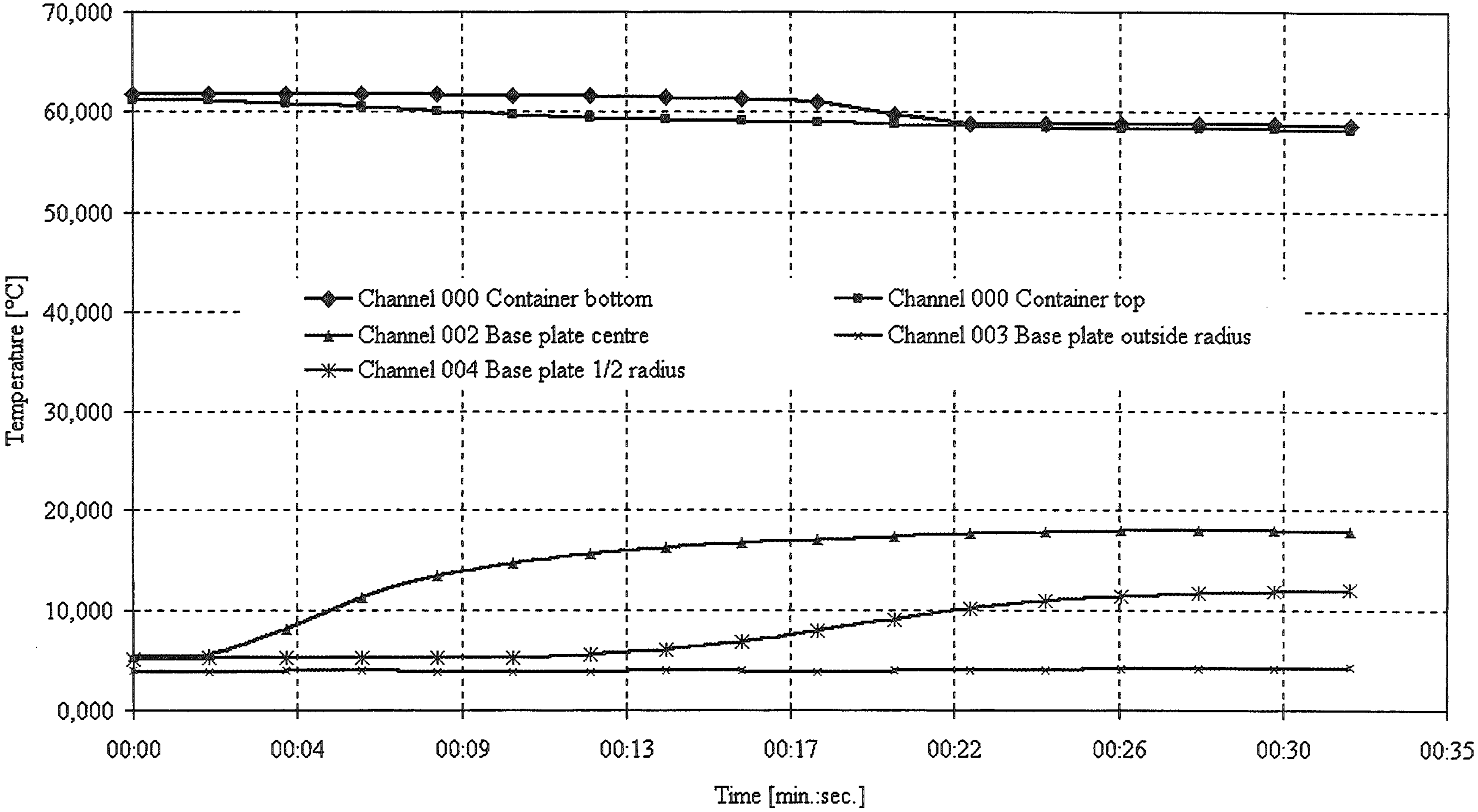

Experiment mcp17 : Temperatures [°C]

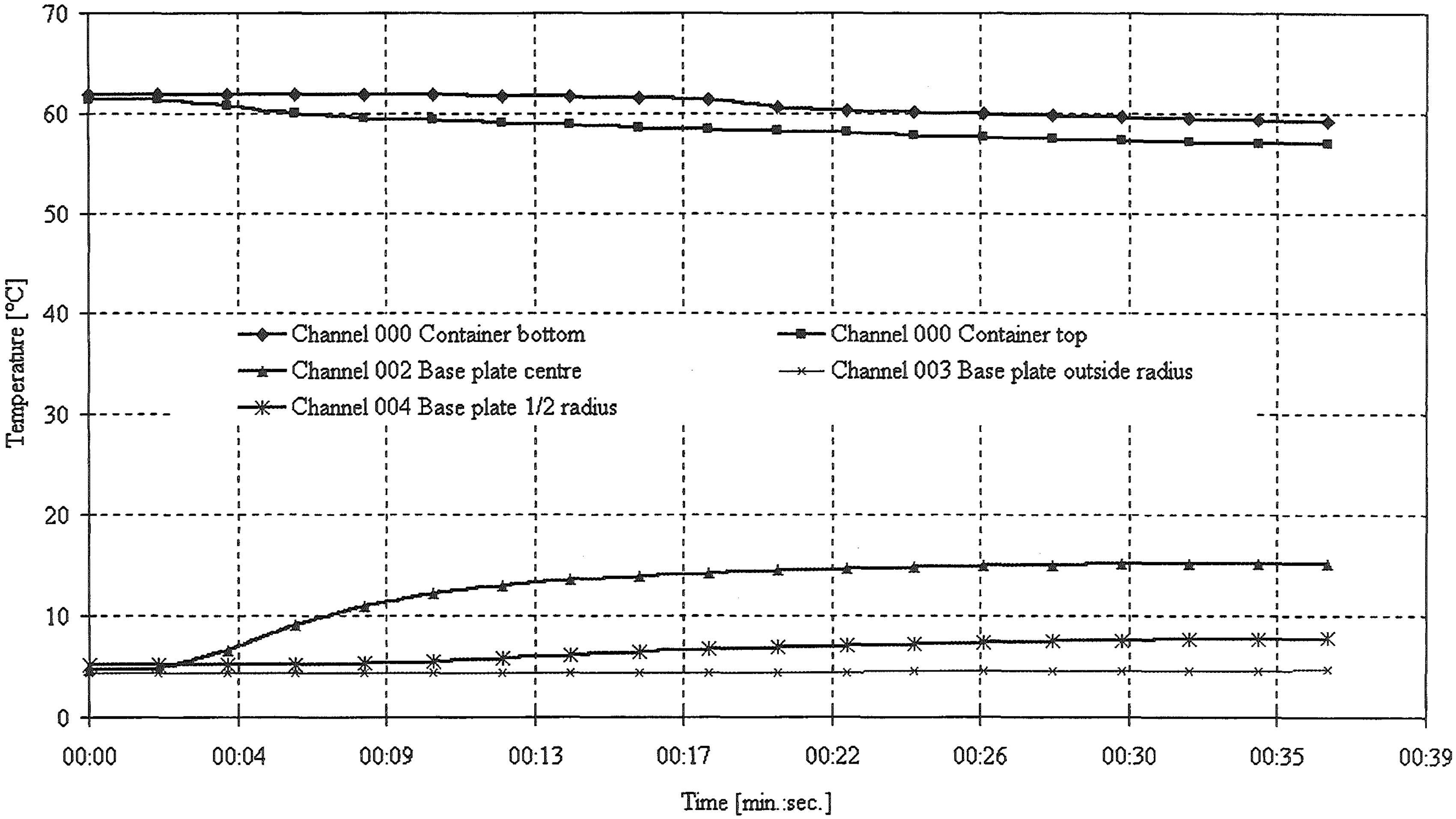

Description of experiment No. 11 and 22

	mcp 11	mcp 22	
Base plate temperature :	4	4	°C
Melt Temperature :	62	66	°C
Height of the melt :	200	200	mm
Aperture diameter :	10	10	mm
Mass of solidified melt :	4935	4590	g

This is the first experiment with a base plate temperature of 4 °C and using 10 mm aperture diameter. The hydraulic jump is some smaller in diameter than in experiment no. 7 (same height of melt, base plate temperature 40 °C), although the volumetric flow rate is nearly the same. A stratification of melt does not happen, therefore, the size of the solidified melt is quite large compared to other non-isothermal experiments. Experiment no. 22 is done with the same geometry and temperatures but here, the plate centre is insulated with a plastic plate (compare description of experiment no. 10/17). Here too, the plate does not strongly influence the spreading. The only remarkable difference is a reduced appearance of fingers during the spreading. The final spreading area is some larger in size although there is 10 % less mass flowed out. The area of shooting flow is greater in size at the beginning but behaviour is the same like in experiment no. 11.

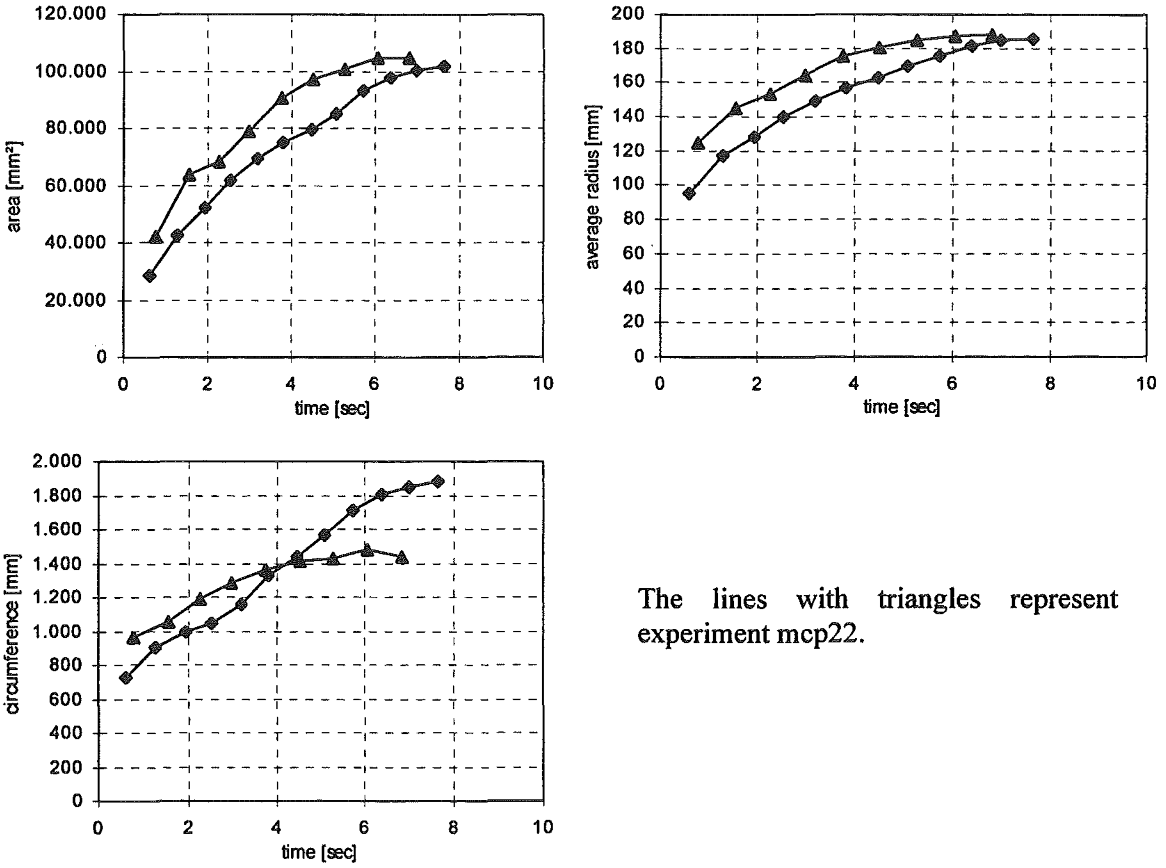

The lines with triangles represent experiment mcp22.

Fig. A11.1: Size of area, radius and circumference over time.

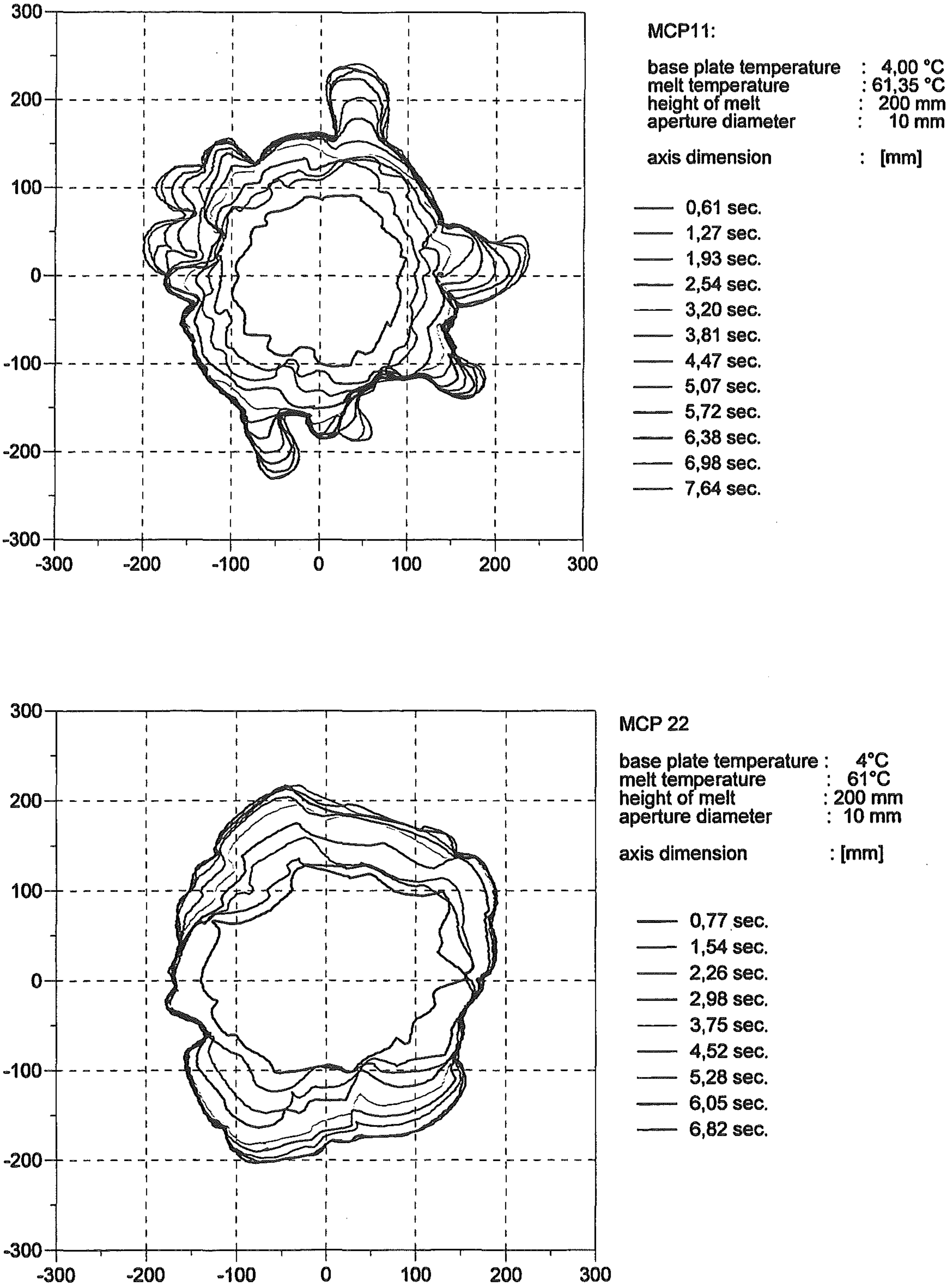

Fig. A11.2: The single phases of the spreading for both experiments.

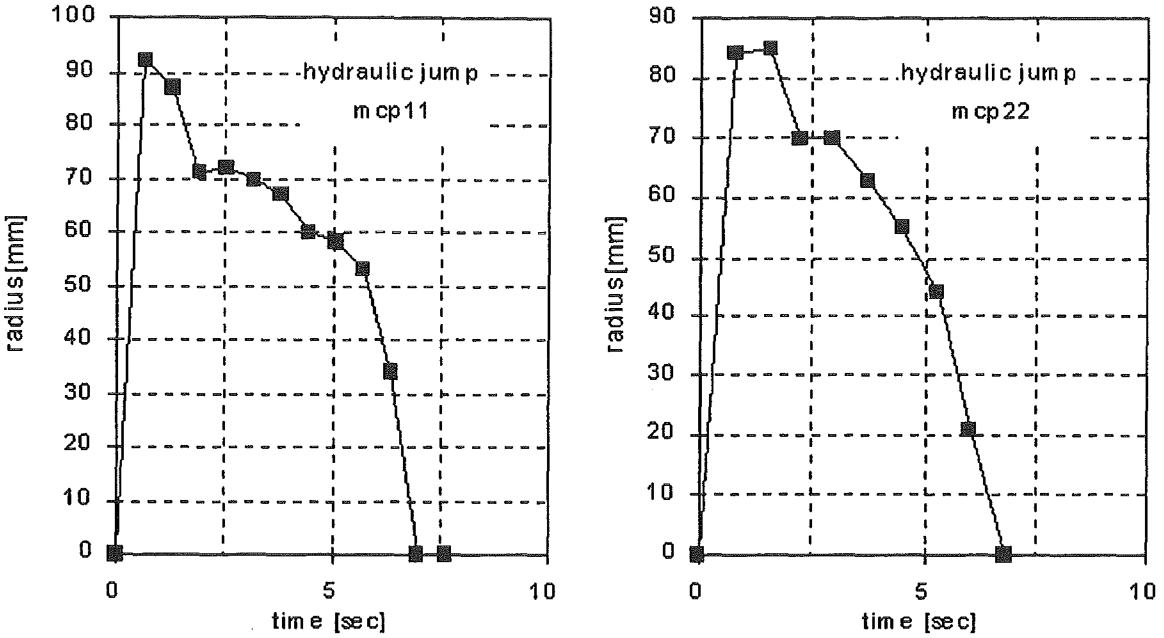

Fig. A11.3: Hydraulic jump in time

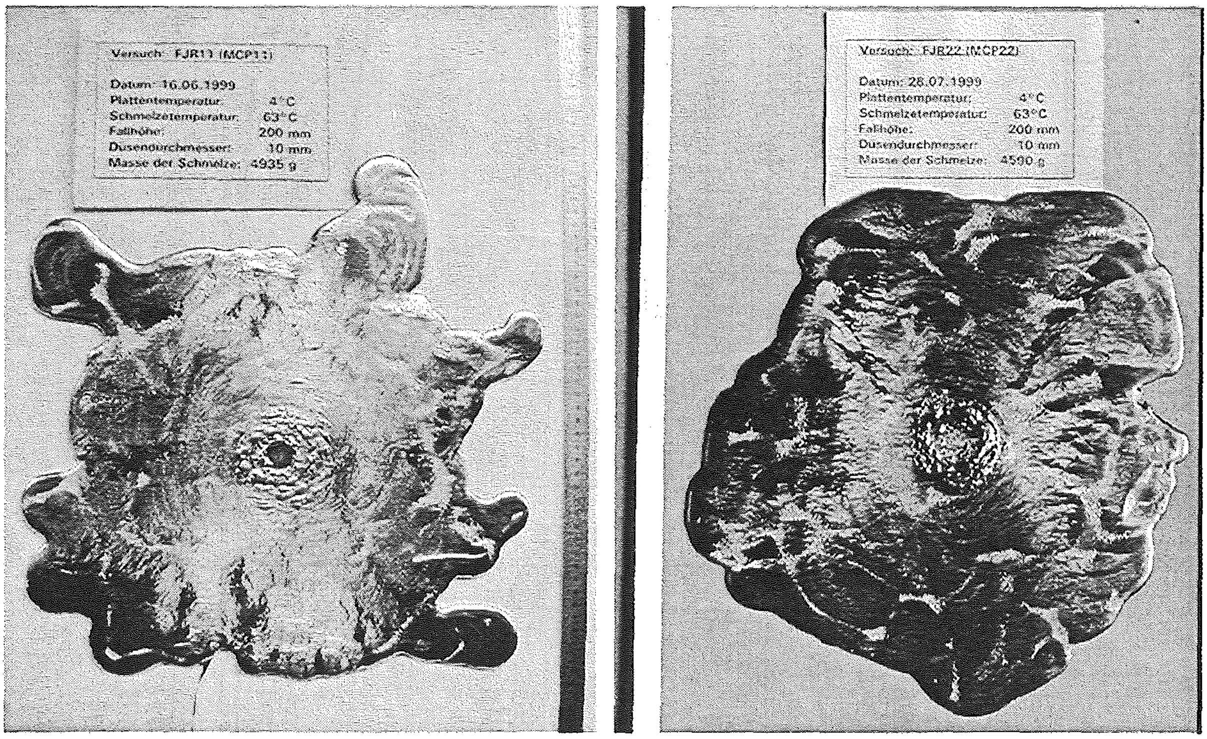

Versuch: FJR11 (MCP11)

Datum: 16.06.1999
Plattentemperatur: 4°C
Schmelzetemperatur: 63°C
Fallhöhe: 200 mm
Düsendurchmesser: 10 mm
Masse der Schmelze: 4935 g

Versuch: FJR22 (MCP22)

Datum: 28.07.1999
Plattentemperatur: 4°C
Schmelzetemperatur: 63°C
Fallhöhe: 200 mm
Düsendurchmesser: 10 mm
Masse der Schmelze: 4590 g

Fig. A11.4 : Top view of the solidified melt of experiment mcp11 (left) and mcp22 (right).

Experiment mcp11 : Temperatures [°C]

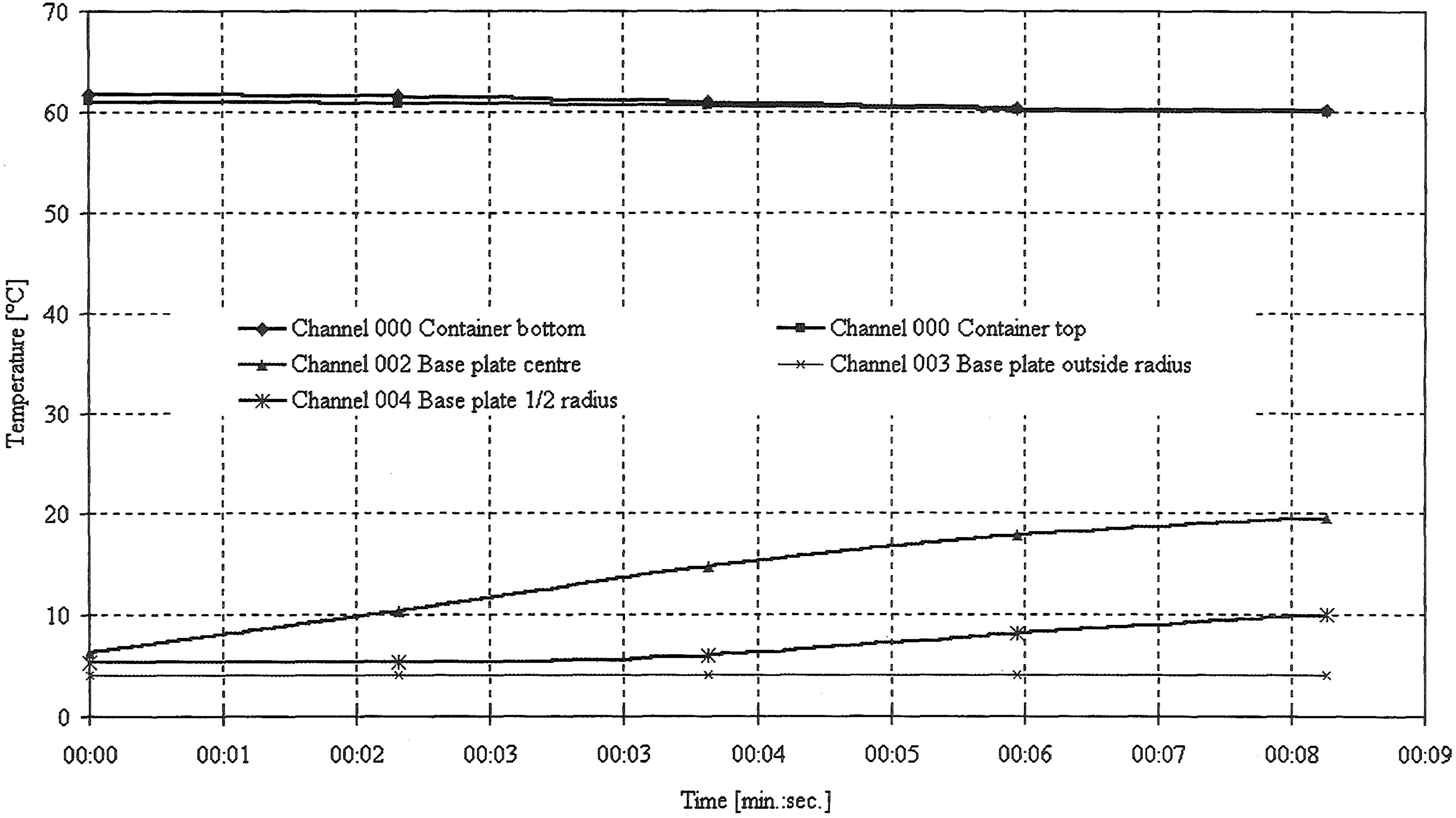

Description of experiment No. 15

Base plate temperature : 60 °C
Melt temperature : 62 °C
Height of the melt : 300 mm
Aperture diameter : 10 mm
Mass of solidified melt : 5866 g

In this experiment, we have a high impact energy combined with a high volumetric flow rate. The result is a very large spreading area and a large diameter of the area of the shooting flow. The form of the hydraulic jump is more elliptic. As the volumetric flow rate decreases to zero, the form of the area of the shooting flow becomes circular (for evaluating the size of the hydraulic jump, an average radius is used in this case). The final shape of the solidified melt is a lengthened circle, its thickness is less than in all other experiments (3,56 mm).

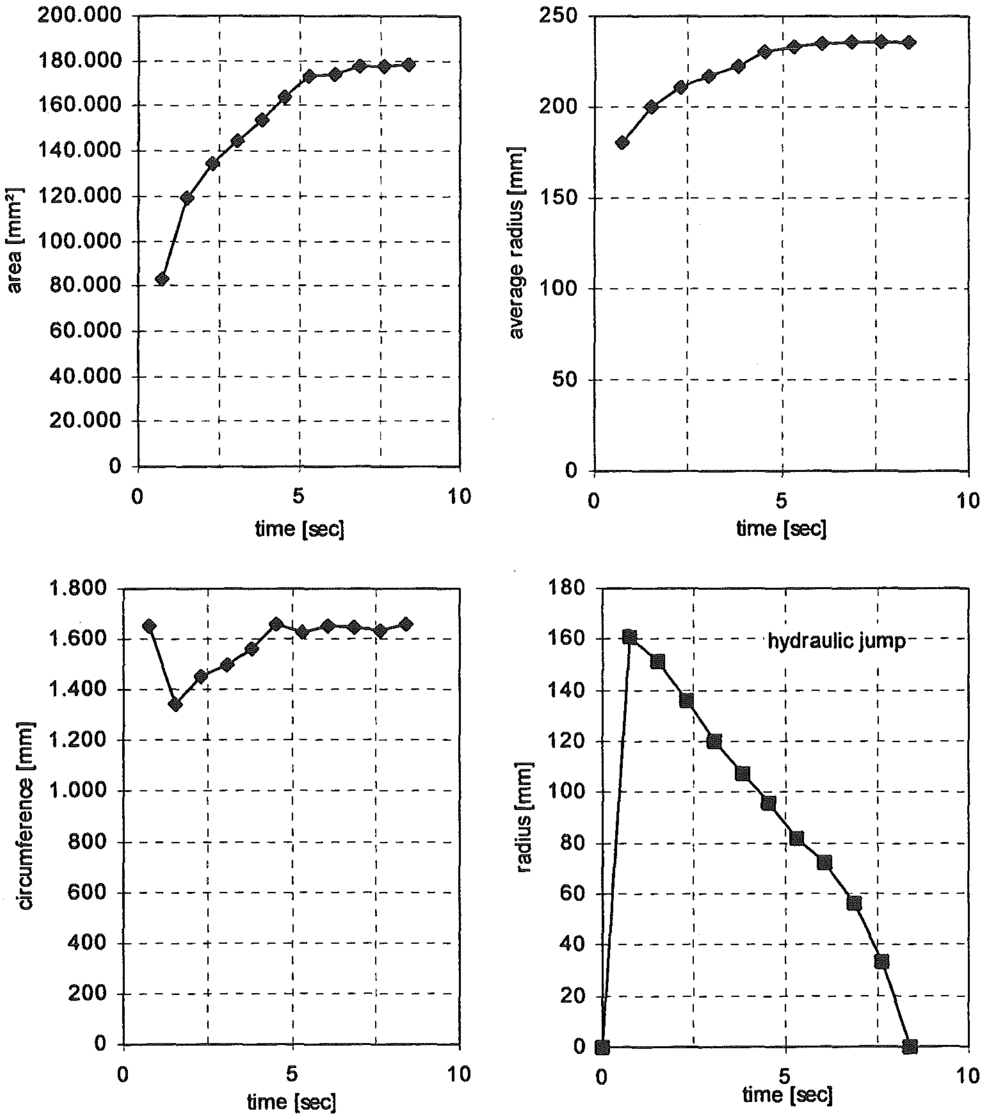

Fig. A15.1: Size of area, radius, circumference and hydraulic jump in time.

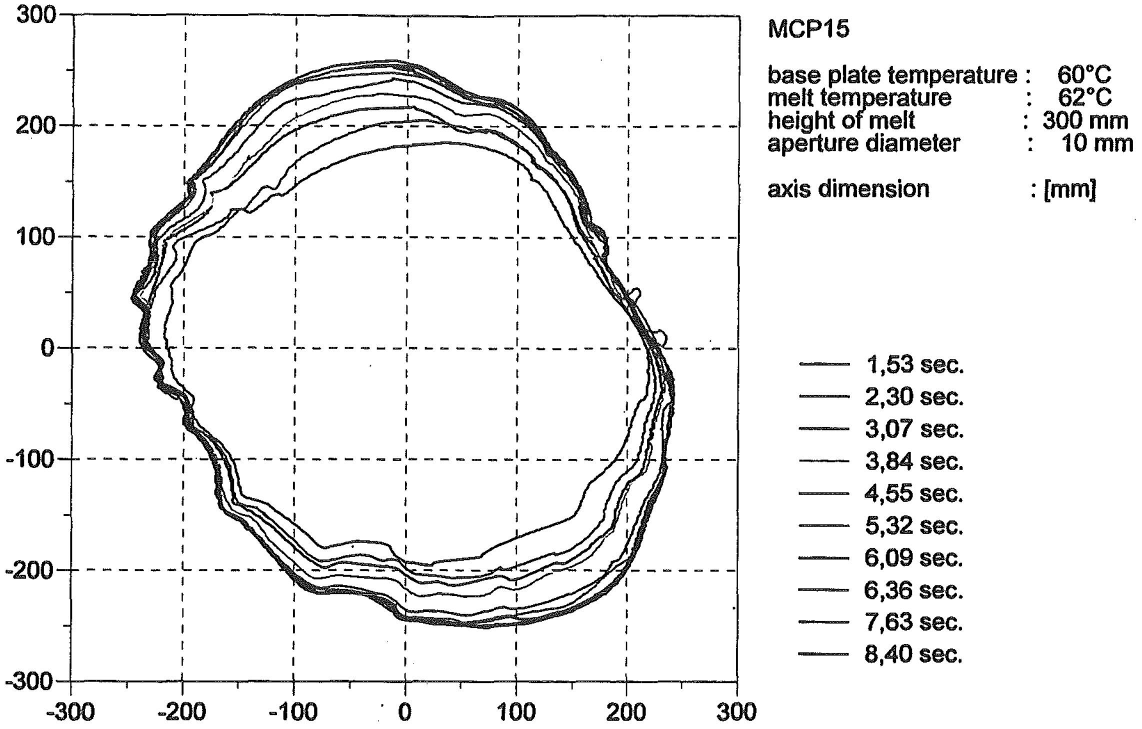

Fig. A15.2 : The single phases of spreading .

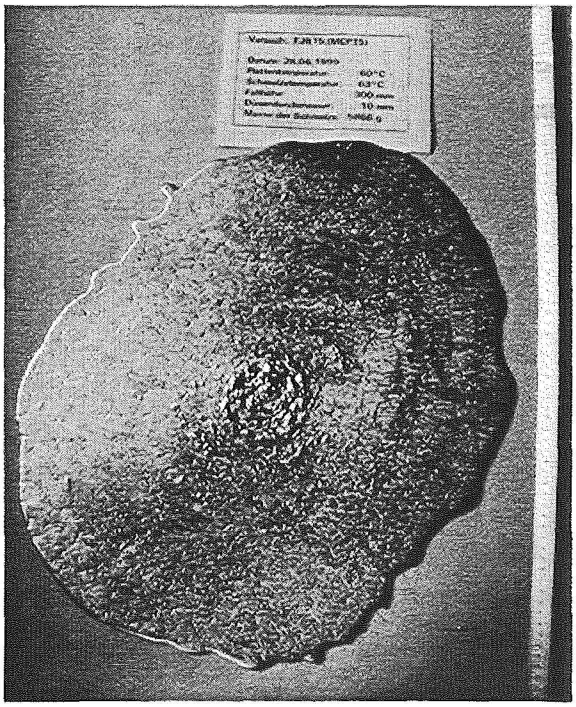

Fig. A15.3: Top view of the solidified melt.

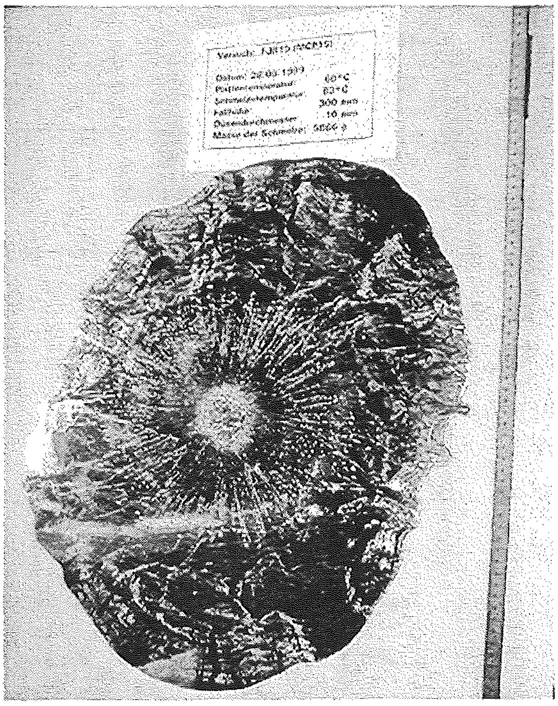

Fig. A15.4: Bottom view of the solidified melt.

Experiment mcp15 : Temperatures [°C]

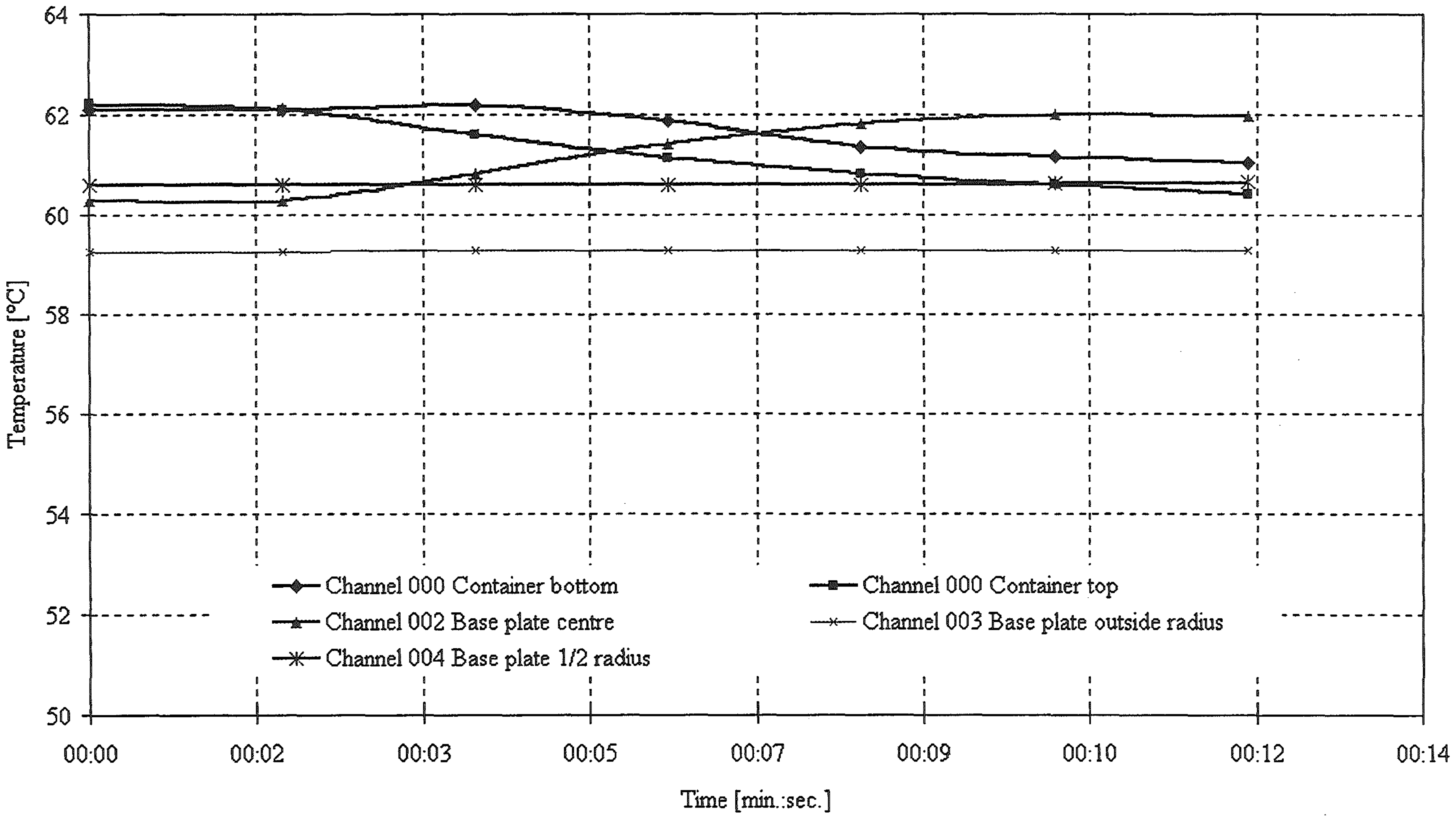

Description of experiment No. 16

Base plate temperature : 4 °C
Melt Temperature : 61,5 °C
Height of the melt : 300 mm
Aperture diameter : 10 mm
Mass of solidified melt : 5692 g

This experiment is executed to verify the influence of the height of melt to the spreading of the melt when using the 10 mm aperture. A visible effect is a faster growing of the spreading area, it reaches over 90 % of its final size after five seconds. This effect results partially from the slightly increased volumetric flow rate (the comparable experiment is no. 11 respectively no. 22). The applied thermal insulation of the impact area has no significant influence to the experiment.

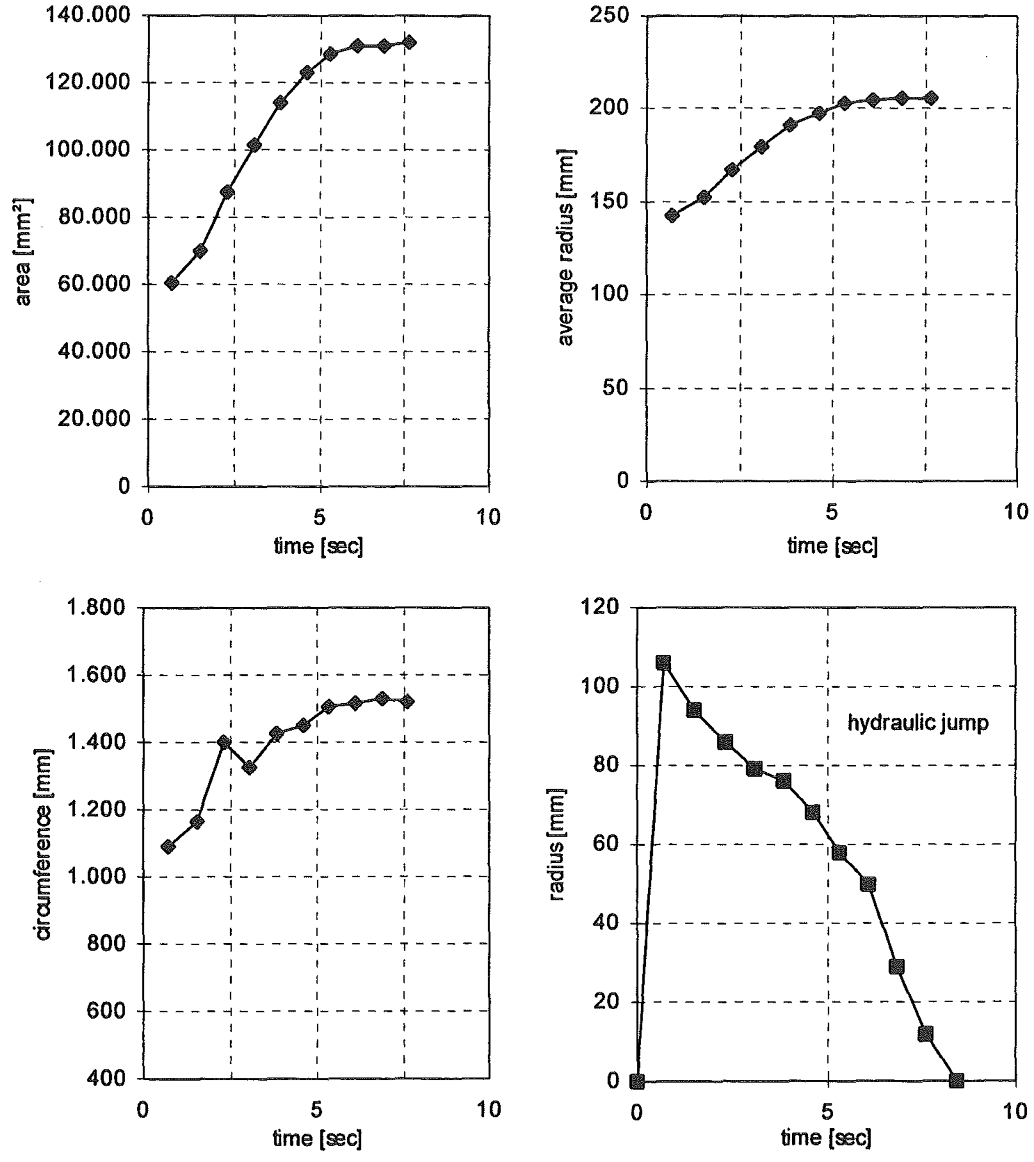

Fig. A16.1: Size of area, radius, circumference and hydraulic jump in time.

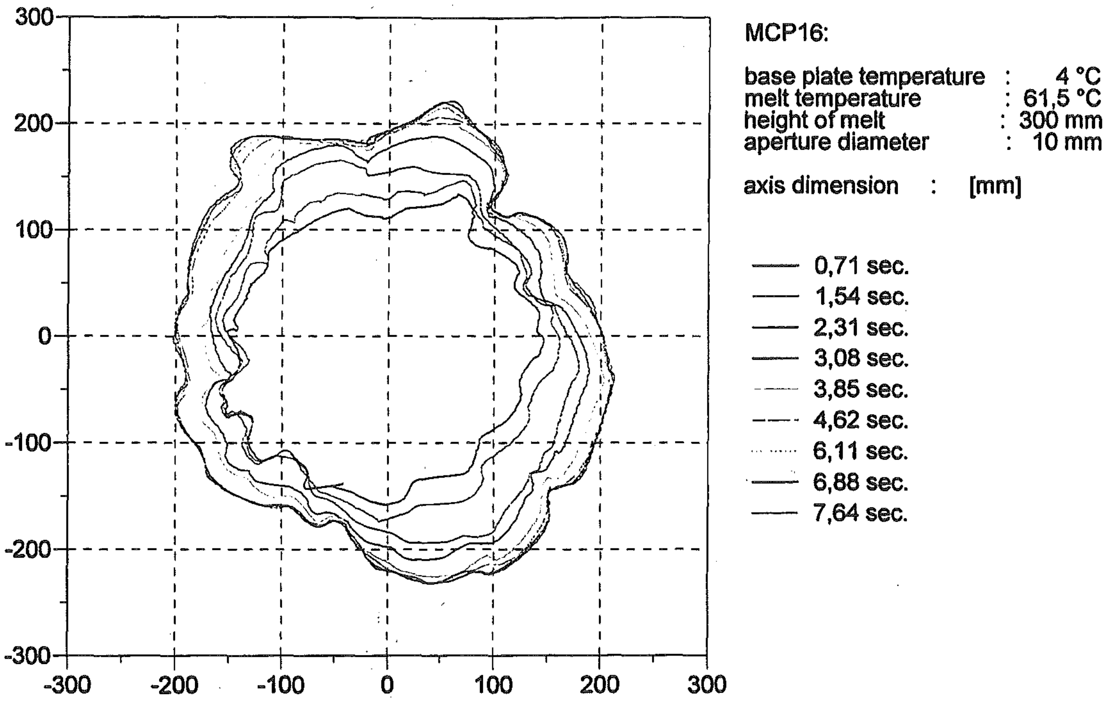

Fig A16.2: Diagramm of the single phases of spreading.

Versuch: FJR16 (MCP16)
Datum: 30.06.1999
Plattentemperatur: 4°C
Schmelzetemperatur: 63°C
Fallhöhe: 300 mm
Düsendurchmesser: 10 mm
Masse der Schmelze: 5692 g

Fig. A16.3: Top view of the solidified melt.

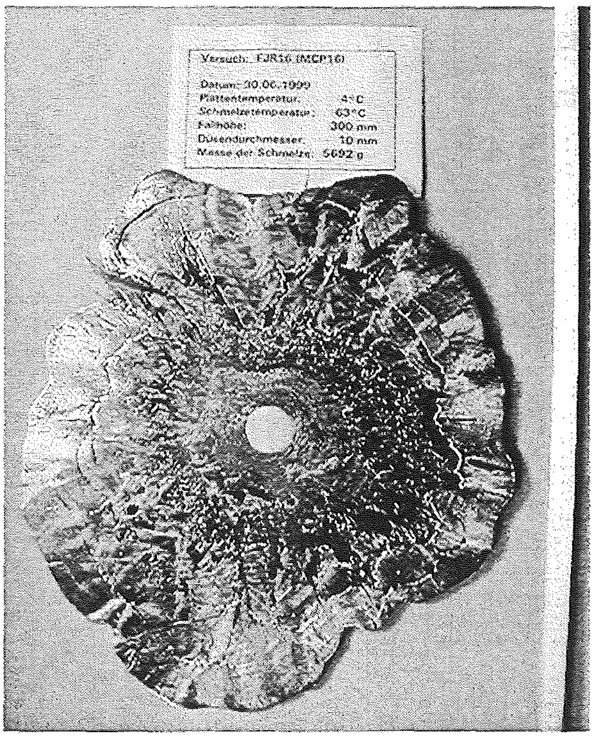

Versuch: FJR16 (MCP16)
Datum: 30.06.1999
Plattentemperatur: 4°C
Schmelzetemperatur: 63°C
Fallhöhe: 300 mm
Düsendurchmesser: 10 mm
Masse der Schmelze: 5692 g

Fig. A16.4: Bottom view of the solidified melt

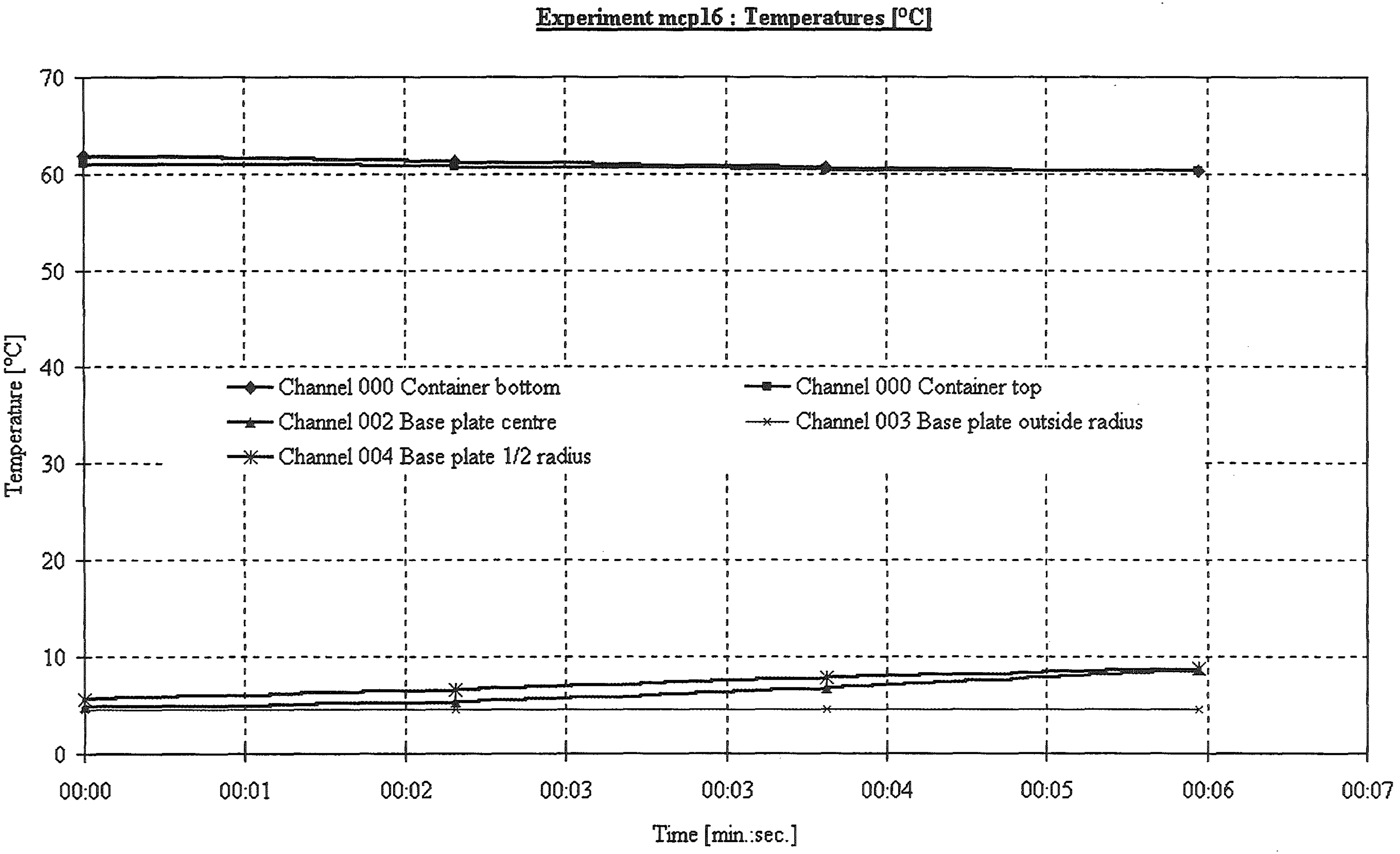
Experiment mcp16 : Temperatures [°C]
Temperature [°C]
70
60
50
40
30
20
10
0
00:00
00:01
00:02
00:03
00:03
00:04
00:05
00:06
00:07
Time [min.:sec.]
Channel 000 Container bottom
Channel 000 Container top
Channel 002 Base plate centre
Channel 003 Base plate outside radius
Channel 004 Base plate 1/2 radius

Description of experiment No. 19 and 20

	mcp 19		mcp20	
Base plate temperature :	40	°C	40	°C
Melt Temperature :	61,7	°C	61,4	°C
Height of the melt :	200	mm	200	mm
Aperture diameter :	5	mm	5	mm
Mass of solidified melt :	5328	g	4924	g

This experiment is executed twice, similar to experiment 10/17. Here, the differences are not so strong as in the set before. Only the behaviour of the hydraulic jump is different. In the experiment without insulation (MCP19) it disappears quite early and the decrease of its radius isn't as smooth as with an insulated impact area. The spreading behaviour is in both cases the same: it has some preferred directions and the melt soon begins to finger out. The result is, that in both cases the solidified melt has a quite irregular shape.

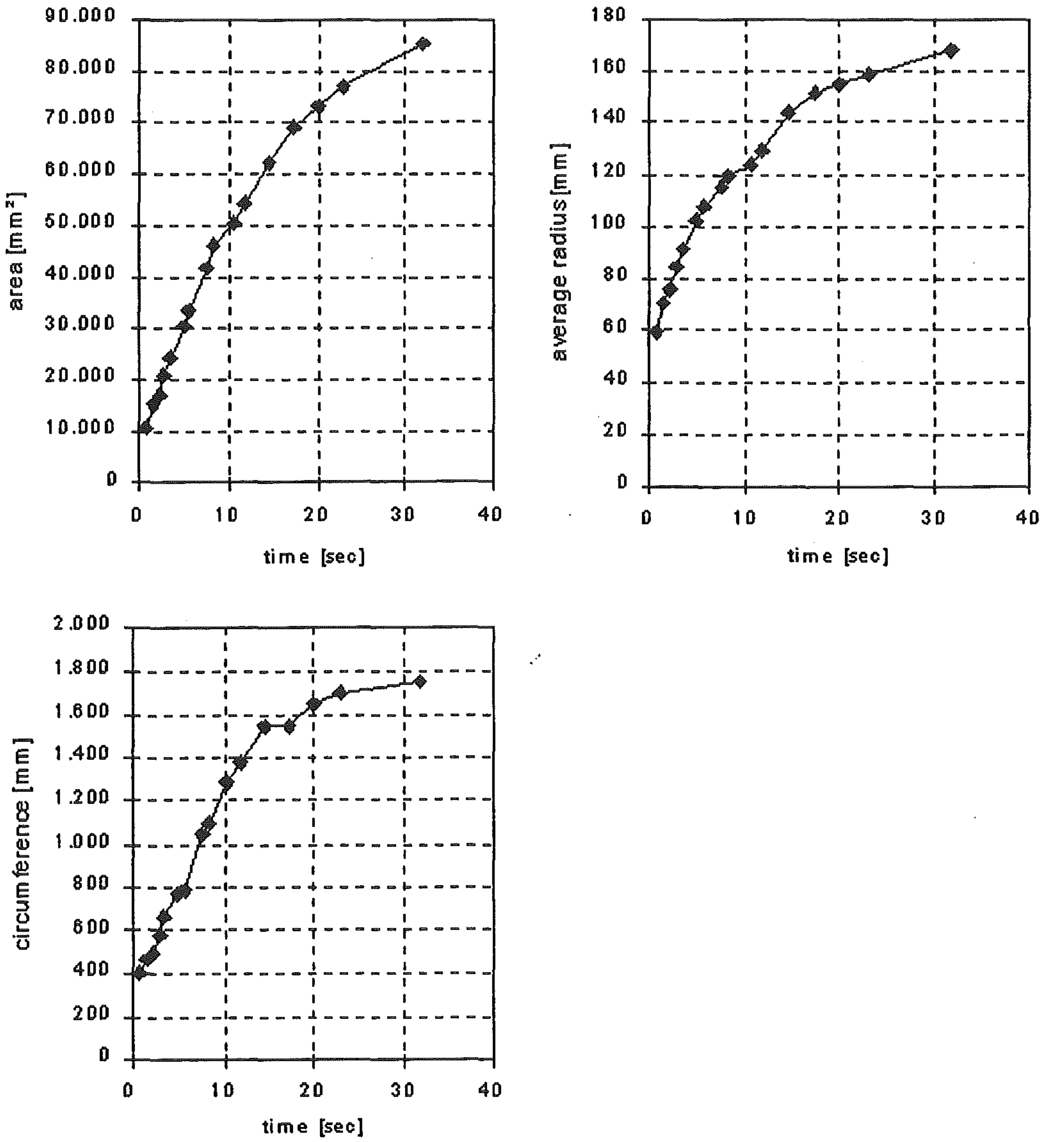

Fig. A19.1: Size of area, circumference and average radius for experiment MCP19.

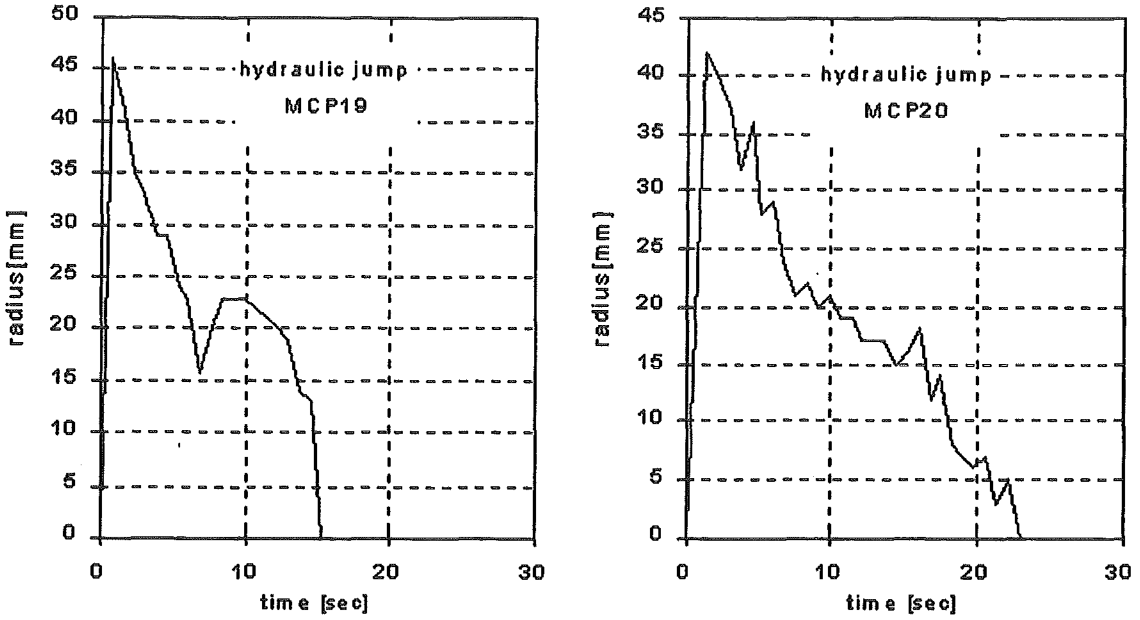

Fig. A19.2: Size of the hydraulic jump for both experiments.

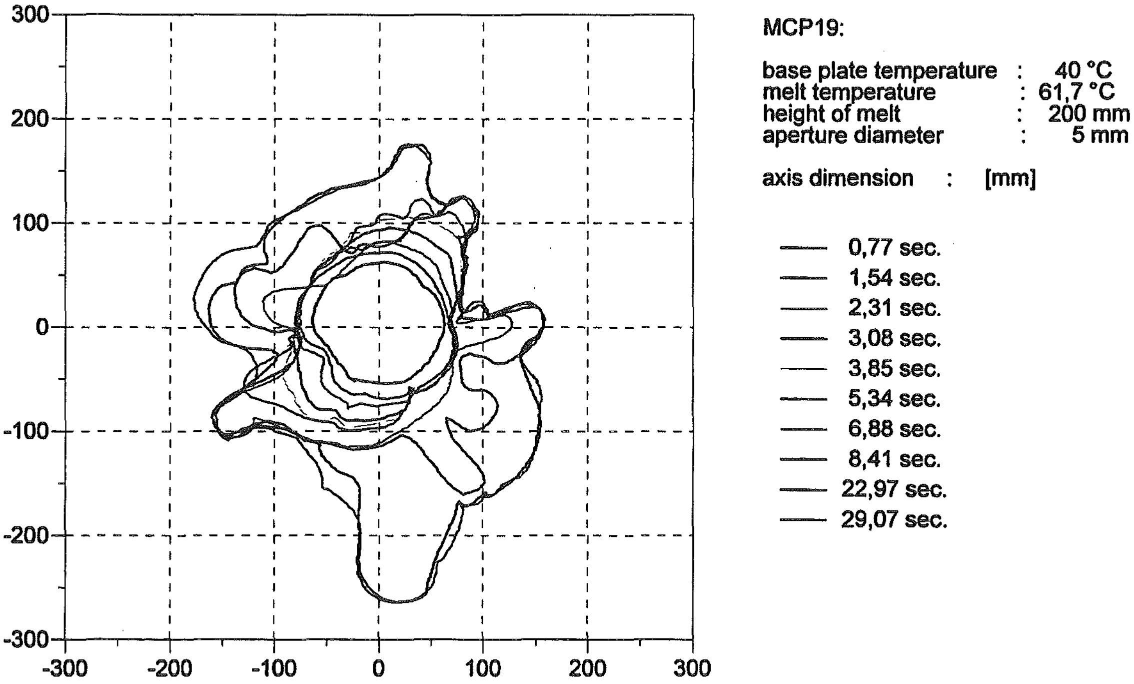
MCP19:

base plate temperature : 40 °C
melt temperature : 61,7 °C
height of melt : 200 mm
aperture diameter : 5 mm

axis dimension : [mm]

Fig. A19.3: The single phases of the spreading.

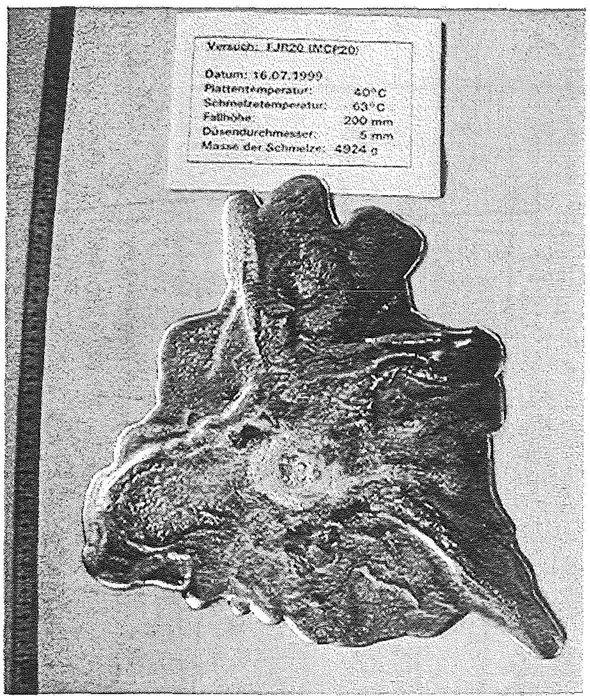

Versuch: EJR20 (MCP20)

Datum: 16.07.1999
Plattentemperatur: 40°C
Schmelzetemperatur: 63°C
Fallhöhe: 200 mm
Düsendurchmesser: 5 mm
Masse der Schmelze: 4924 g

Fig. A19.4: Top view of the solidified melt for experiment mcp19

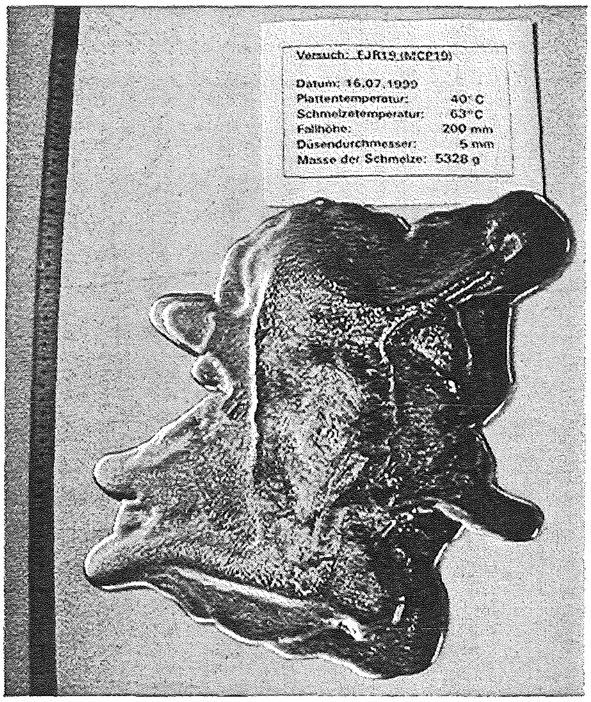

Versuch: EJR19 (MCP19)

Datum: 16.07.1999
Plattentemperatur: 40°C
Schmelzetemperatur: 63°C
Fallhöhe: 200 mm
Düsendurchmesser: 5 mm
Masse der Schmelze: 5328 g

Fig. A19.5: Top view of the solidified melt for experiment mcp20

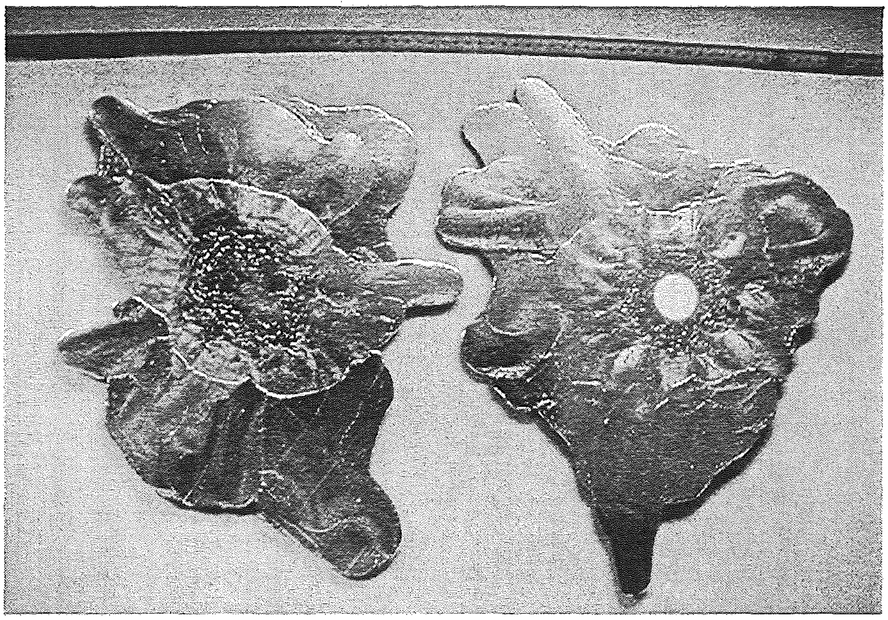

Fig. A19.6: Bottom view of the solidified melt for experiment mcp19 (left) and mcp20 (right).

Experiment mcp19 : Temperatures [°C]

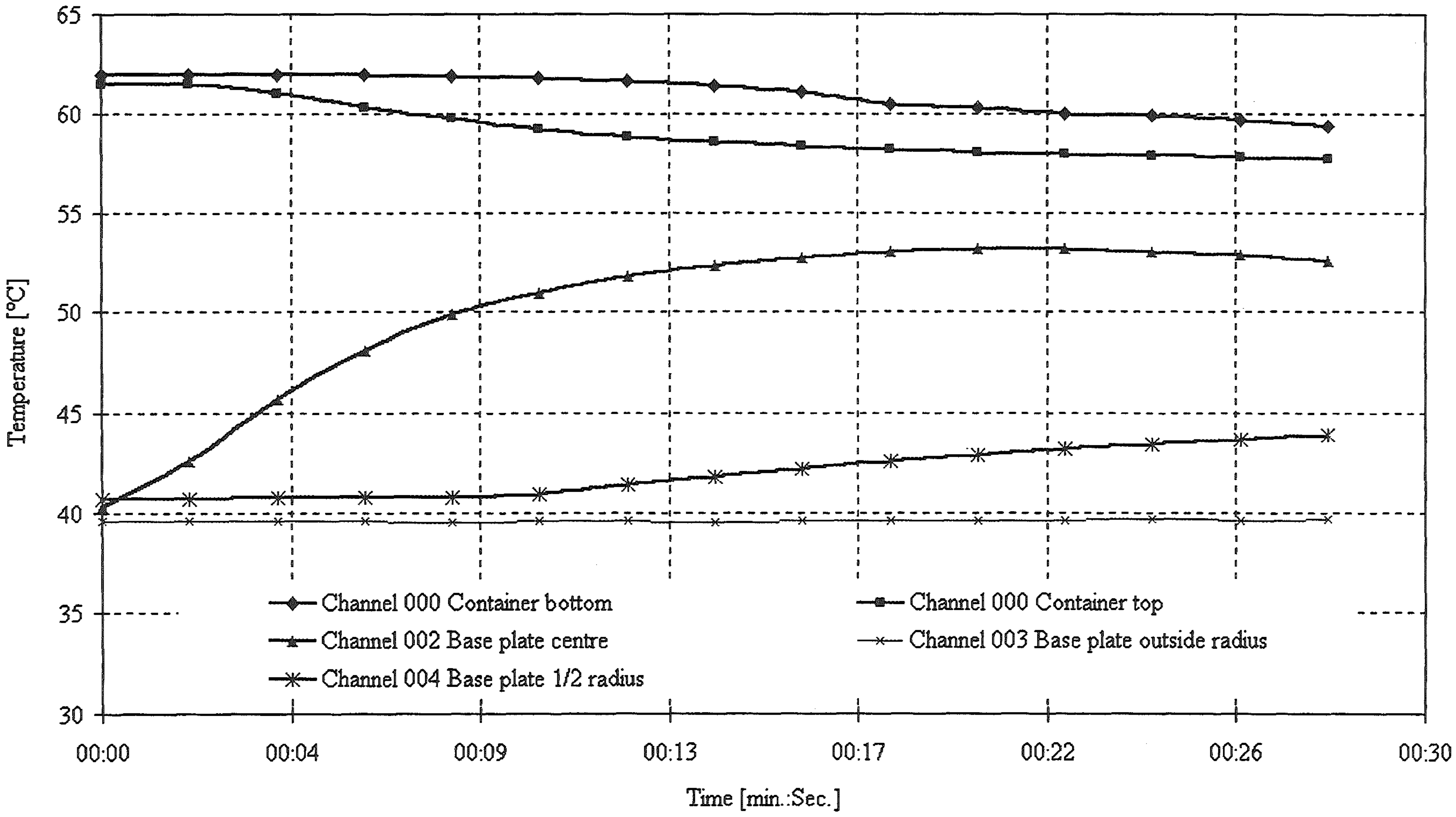

Description of experiment No. 23

Base plate temperature :	60	°C
Melt temperature :	63	°C
Height of the melt :	200	mm
Aperture diameter :	10	mm
Mass of solidified melt :	4929	g

This experiment is done to verify the general influence of the height of melt over the base plate for isothermal experiments. The comparable experiment is mcp15. If one compares the two experiments, one can see similar results for area, circumference and average radius. The volumetric flow rate is less in this case, the smaller radius of the hydraulic jump at the beginning is the result.

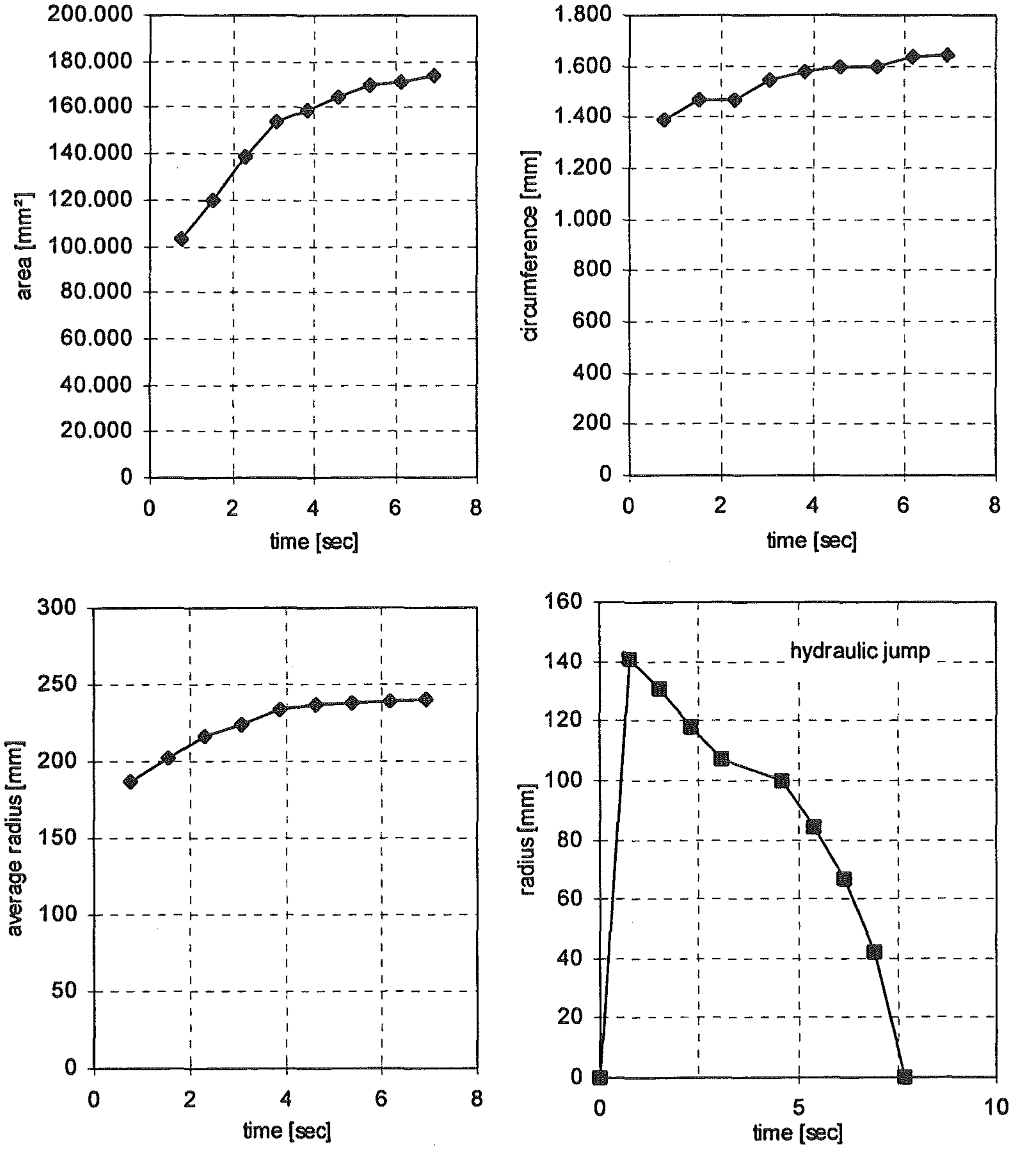

Fig. A23.1: Size of area, radius, circumference and hydraulic jump in time

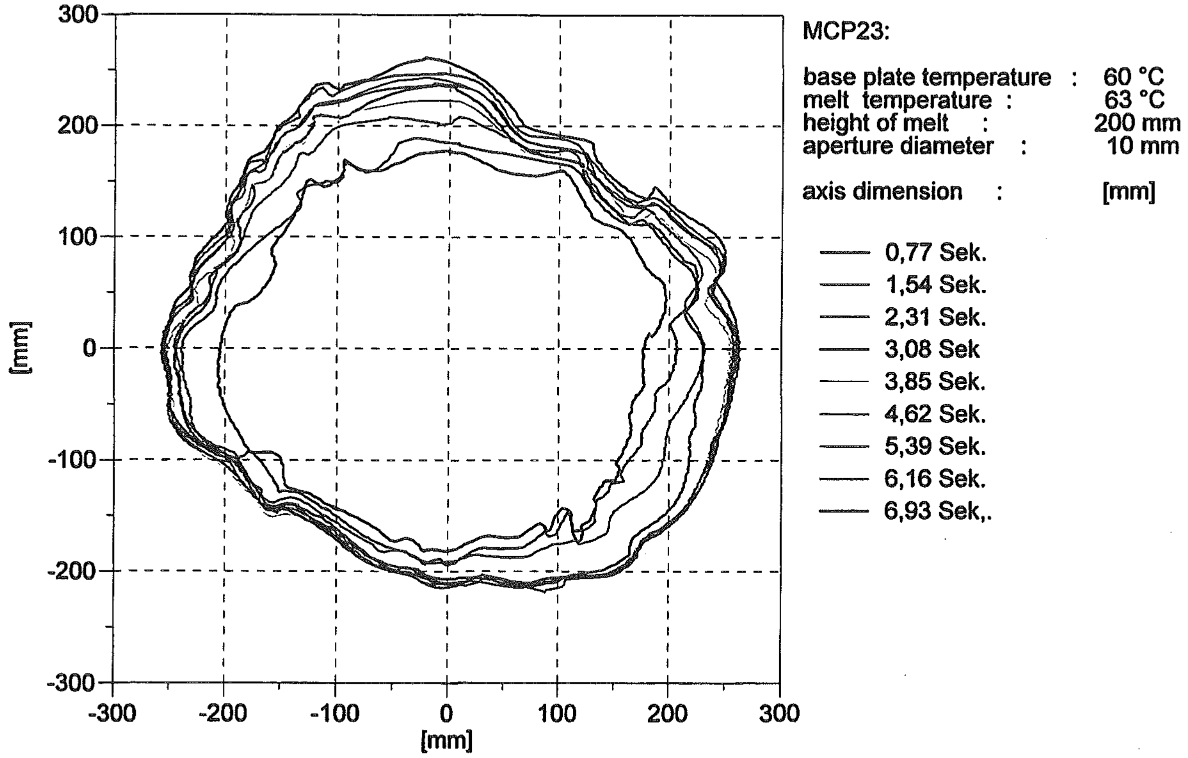

Fig. A23.2: Sequence of the spreading.

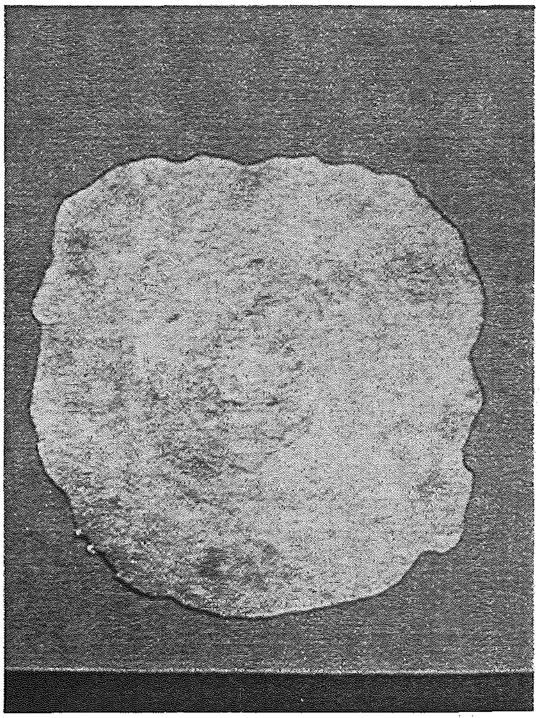

Fig. A23.3 Top view of the solidified melt.

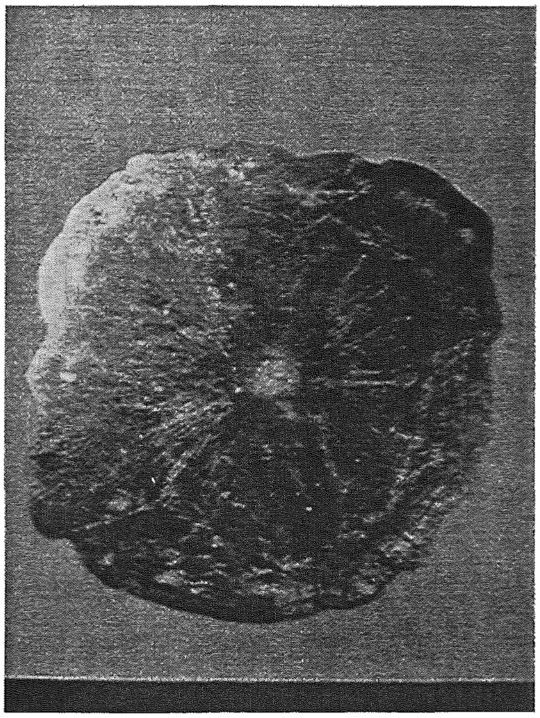

Fig. A23.4 Bottom view of the solidified melt.